論文 / 著書情報
Article / Book Information

題目(和文)	
Title(English)	First-Principles Study on Electronic Structure and Doping for Novel Compound Semiconductors, BaZn2As2, SnS, and Cs2SnI6
著者(和文)	XiaoZewen
Author(English)	Zewen Xiao
出典(和文)	学位:博士（理学）, 学位授与機関:東京工業大学, 報告番号:甲第9957号, 授与年月日:2015年9月25日, 学位の種別:課程博士, 審査員:神谷　利夫,多田　朋史,東　正樹,細野　秀雄,大場　史康,平松　秀典
Citation(English)	Degree:Doctor (Science), Conferring organization: Tokyo Institute of Technology, Report number:甲第9957号, Conferred date:2015/9/25, Degree Type:Course doctor, Examiner:,,,,,
学位種別(和文)	博士論文
Type(English)	Doctoral Thesis

First-Principles Study on Electronic Structure and Doping for Novel Compound Semiconductors, $BaZn_2As_2$, SnS, and Cs_2SnI_6

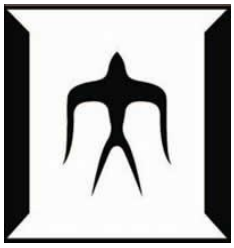

Zewen Xiao

Department of Innovative and Engineered Materials

Tokyo Institute of Technology

2015

Contents

Chapter1

General Introduction

1.1 Background of This Study

1.1.1 Band Aligment of Inorganic Semiconductors

Novel compound semiconductors exhibit a wide variety of electronic functions and are expected to take over the current silicon technology for some applications. Controlling both *n*-type and *p*-type conductivities in a semiconductor is very important for some practical semiconductor devices such as p/n junctions and p/i/n light-emitting diodes/solar cells. However, doping asymmetry is a serious issue in some compound semiconductors with strong ionicity, where only either of *n*-type or *p*-type doping is realized.

The dopability of semiconductors can be empirically understood based on the band alignment of various semiconductors, e.g., as shown in Fig. 1.1. A semiconductor cannot easily be doped *n*-type if its conduction band minimum (CBM) lies too shallow towards the vacuum level (E_{Vac}), i.e., its electron affinity (*EA*) is too small. $CuAlO_2$ would be an example. On the other hand, a semiconductor cannot easily doped *p*-type if its valence band maximum (VBM) lies too deep from the E_{Vac}, i.e., the ionization potential (*IP*) is too large. Most oxides such as ZnO are typical examples. Besides, the band alignment is also often practically used to design a wide variety of semiconductor devices, heterojunctions, etc.

1.1.2 Chemical Design of Inorganic Semiconductors

Inorganic solids with wide band gaps are usually classified as electrical insulator and are used in industry as electrical insulators, dielectrics, and optical materials. Many metal oxides have wide band gaps because of the significant contribution of ionic character to the chemical bonds between metal cations and oxygen anions. The ionic nature simultaneously suppresses the formation of easily ionizable shallow donors or acceptors and tends to cause the localization of electrons and holes. Exceptionally, some wide band gap oxides are conductive [1,2]. The oxides of *p*-block heavy-metal cations with $(n–1)d^{10}ns^0$ electron configurations (where principal quantum number $n > 4$)—such as ZnO, Ca_2O_3, In_2O_3, SnO_2, and their complex compounds/solid solusions (see Fig. 1.1)—can be converted to *n*-type conductors by electron doping with keeping the optical transparency for human eyes. Transparent conducting oxides (TCOs), represented by commercially available Sn-doped In_2O_3 (indium tin oxide, ITO), have widely been used as transparent electrodes for liquid crystal displays (LCDs), organic light-emitting diodes (OLEDs), electrochromic windows, and solar cells [3,4]. In these ionic oxides, their CBM are composed primarily of unoccupied *s* orbitals of the *p*-block heavy metal cations. The spatial spread of the unoccupied *s* orbitals is so large that the direct overlap between the *s* orbitals of adjacent cations is possible and the effective electron mass is small. As a result, TCOs exhibit high electron mobilities, e.g. >150 $cm^2V^{-1}s^{-1}$ for In_2O_3 [5].

In 1996 Prof. Hosono proposed a working hypothesis for exploring transparent conducting amorphous oxides [6]. In the hypothesis, the magnitude of the overlap of neighboring *p*-block metal *ns* orbitals was considered insensitive to disordered metal–oxygen–metal (M–O–M) chemical bonds that intrinsically exist in amorphous materials because of the isotropic shape of *s* orbitals [7], and therefore the amorphous

oxides would have high electron mobility comparable to that in the corresponding crystalline phase. This simple hypothesis have been proved valid and useful by the observation of high electron mobilities ~10 $cm^2V^{-1}s^{-1}$ in amorphous Cd_2GeO_4, $AgSbO_3$ and Cd_2PbO_4 [6]. In 2004, Hosono group [8] reported transparent and flexible thin-film transistors (TFTs) using amorphous In–Ga–Zn–O (a-IGZO), a representative amorphous oxide semiconductors (AOSs), which have advantages such as optical transparency and high electron mobilities > 10 $cm^2V^{-1}s^{-1}$ over conventional amorphous semiconductors such as hydrogenated amorphous silicon (a-Si:H) [9]. Since then, AOSs have widely been investigated and a-IGZO TFTs are now used in current flat-panel displays such as liquid-crystal displays (LCDs) in small-size smartphones, middle-size tablets and notebook computers, and 32'' 4K LCDs as well as 77'' 4K OLED TVs [10–13].

It is known for most TCOs, particularly, AOSs, *n*-type conduction is readily attained; while *p*-type conduction is relatively difficult because the VBM of oxides generally consists of localized oxygen 2*p* orbitals due to the strong iconicity, for which the accepters have deep levels and the hole mobility is rather small. To expand the application of TCOs (including AOSs) for most semiconductor devices, the fabrication of *pn* junctions exclusively from semiconducting TCOs is essential. Therefore, much efforts have been devoted to exploring *p*-type semiconducting TCOs in the past two decades [14–17]. In 1997, Prof. Hosono group [14] proposed a chemical design concept for *p*-type TCOs, where its essence is to extend the VBM wave functions by introducing covalency in the metal–oxygen bonds, namely, the VBM consists of the resulting antibonding level and thus become dispersive. To avoid visible light absorption due to transitions in unfilled orbitals, metal cations are required to have a (pseudo-)closed shell (e.g., $(n–1)d^{10}ns^0$ and $(n–1)d^{10}ns^2$ electron configurations), and to form a dispersive VBM, their energy levels should be close

to those of the O 2*p* levels. There are a few examples of such appropriate cations; Cu^{+}, Ag^{+} and Zn^{2+} for $(n–1)d^{10}ns^{0}$, and Sn^{2+}, Pb^{2+} and Bi^{3+} for $(n–1)d^{10}ns^{2}$. Among them, Cu^{+} has a 3*d* levels close to the O 2*p* levels and is widely chosen for *p*-type TCOs and other *p*-type semiconductors such as $CuIn_xGa_{1–x}Se_2$ (CIGS), an absorber material for solar cells [18]. In fact, Cu_2O is a naturally *p*-type oxide semiconductor with high hole mobilities of >70 $cm^2V^{–1}s^{–1}$, and can produce *p*-channel TFTs exhibiting several $cm^2V^{–1}s^{–1}$ of field-effect mobilities [19]. However, Cu_2O has a rather small band gap (2.17 eV) compared with those of TCOs (> 3.1 eV). Along with the above chemical design concept, Hosono et al [14] reported aluminate of Cu^{+}, $CuAlO_2$ with the delafossite structure as a *p*-type TCO, which show considerable improvement over the first *p*-type TCO, NiO [20]. Since then, two families of Cu^{+}-based TCOs, $CuMO_2$ (*M* = Al, Ga, In, Sc, etc.) [21–24] delafossites and non-delafossites including $SrCu_2O_2$ [25] and LaCuO*Ch* (*Ch* = chalcogen) [26–28], have been developed with the chemical design concept. It is known that Zn^{2+} has deeper 3*d* levels than those of Cu^{+}, but shallower than Ga 3*d*, Cd 4*d* and In 4*d* levels and comparable to O 2*p* levels. As a result, Zn 3*d* as well as O 2*p* orbitals contribute to pushing up the VBM and to forming a dispersive VBM in ZnO [29]. It has been reported that ZnO can be converted to *p*-type by Li^{+} doping to the Zn^{2+} sites [30], $N^{3–}$ doping to $O^{2–}$ sites [31,32], etc., although there are still issues remaining on their stability and reproducibility. Sn^{2+} has occupied 4*s* orbitals slightly lower than O 2*p* orbitals and the VBM of SnO consists of hybridized orbitals of Sn 4*s* and O 2*p* and is spatially dispersive. SnO has a direct band gap of 2.7 eV and an indirect band gap of 0.7 eV, and exhibits naturally *p*-type conduction with drift and field-effect mobilities of several $cm^2V^{–1}s^{–1}$ in thin films and TFTs [33,34].

Although many crystalline *p*-type TCOs have been developed with the above chemical design concept, it is difficult to achieve *p*-type conduction in amorphous ones, i.e.

AOSs. So far, amorphous xZnO·Rh_2O_3 (x = 0.5–2.0) [35,36], Cr_2O_3 [37] SnO_2 [38] have been reported to exhibit *p*-type conduction, but their hole mobilities are very small, < 0.1 $cm^2V^{-1}s^{-1}$. Further, there have been other compounds beyond oxides examined for high-mobility *p*-type amorphous semiconductors. For example, simple Cu-based simple chalcogenides ($Cu_{1.6}S$ and $Cu_{1.7}Se$) and chalcopyrites ($CuM(S,Se)_2$, M = Al, Ga, and In) exhibit tunable *p*-type conductivities from10^{-5} to 10^4 S cm^{-1}; however, their TFTs didn't work because of the high-density subgap states [39]. Therefore, it is still a challenging issue to explore high-mobility *p*-type AOSs and beyond.

1.1.3 Doping Asymmetry in Inorganic Semiconductors

The controllability of carrier type, i.e., *p*-type (hole conducting) and *n*-type (electron conducting), is a fundamental and important requirement for a semiconductor to produce high-performance electronic devices with a homo pn junction structure. Currently, bipolar semiconduction is achieved in some semiconductors mainly by aliovalent substitutional doping. For example, silicon (4 valence electrons in a Si atom), which is the most common semiconductor used in integrated circuits, exhibits *p*-type and *n*-type conductions by doping B (3 valence electrons) and P (5 valence electrons), respectively [40]. However, bipolar semiconduction becomes more difficult for compound semiconductors, particularly, those with wide band gaps. ZnO is naturally *n*-type, but not *p*-type [41–45]. NiO is naturally doped *p*-type, but not *n*-type [20,42]. SnS is naturally a *p*-type semiconductor with a narrow band gap of 1.07 eV, but it is difficult to be doped *n*-type [46,47]. These doping asymmetry problems have hindered the potential applications of many such semiconductors with unique properties. In the last few decades, much efforts have been made to understand the origin of the doping asymmetry particularly in wide-band gap

semiconductors and to overcome the doping asymmetry [43–45]. It is now known that *n*-type diamond and *p*-type ZnO can be achieved by choosing some dopants and designing some specific defect complexes.

Generally, the doping asymmetry is caused by three main reasons; (i) spontaneous formation of compensating defects, (ii) the desirable dopants have limited solubility, and (iii) the desirable dopants have sufficient solubility, but they produce deep levels, which are not ionized at working temperatures. The first reason is an intrinsic problem to the host material, which is the most difficult problem to be overcome. It is known that the formation energy of a charged defect depends linearly on the position of the Fermi level, E_F. When a semiconductor is doped *p*-type, E_F moves closer to the VBM. In the case, the formation energies of the charged accepter defects increase and those of the compensating donor defects decrease. As a result, further *p*-type doping become more difficult. Conversely, a similar but opposite trend is found also for *n*-type doing. The second reason depends highly on the selected dopants and may be improved by fabrication condition (i.e. the chemical potentials of dopants and host elements, respectively). The third reason depends on the selected dopant (i.e. the ionic radius, electronegativity, etc.). Therefore, the latter two reasons can sometimes be solved by finding appropriate dopants and fabrication conditions.

First-principles density functional theory (DFT) has widely been used to calculate the formation energies and transition energies of intrinsic and extrinsic defects. Based on DFT calculations, various approaches have been proposed to overcome the doping asymmetry in semiconductors. Taking *p*-type doping of ZnO as an example, the following approaches has been suggested:

(i) Solubility of acceptor impurities can be increased by adjusting their chemical

potential [48,49]. Raising the chemical potential of an acceptor dopant in the ZnO would increase the solubility of the dopant and suppress precipitate formation. For example, metastable NO and NO_2 can supply reactive nitrogen atoms more easily than N_2 can. Therefore, doping with NO and NO_2 should result in higher solubility of nitrogen compared to N_2 [49].

(ii) Ionization energy of an acceptor can be reduced by designing shallower dopants or dopant complexes [50–52]. For example, the ionization energy of N_O (N at an O site) can be reduced by replacing Zn with isovalent Mg or Be to form shallower N_O+$n$$Mg_{Zn}$ or N_O+$n$$Be_{Zn}$ complexes. Therefore, Mg and Be could be good codopants pairs for nitrogen to achieve *p*-type ZnO [52].

(iii) Both ionization energy of an acceptor level and defect compensation can be reduced by modifying the host band structure near the band edge [43]. The valence band edge of ZnO can be modified by passivating codopants such as Ga and N. N combined with Ga creates a passivated defect band above the VBM. The shallow acceptor levels can be created by doping the passivated ZnO:(Ga+N) system with excessive N [43].

Despite many reports on *p*-type ZnO, there are still issues remaining on their stability and reproducibility, and no credible *p*-type ZnO has been reported to be suitable for practical light-emitting devices. Nevertheless, the above approaches would be also effective to solve the doping asymmetry problem in other materials. Further, more doping routes are desired to achieve stable and reproducible doping and carrier conversion.

1.2 Objectives of This Study

The final purpose of this work is to desigin both *n*-type and *p*-type doping in more variety of compound semiconductors. Specifically, this study have two objectives.

As reviewed in Section 1.1.2, many *n*-type amorphous semiconductors represented by a-IGZO have been developed and have shown high electrons mobilities > 10 cm^2 V^{-1} s^{-1}. However, several *p*-type amorphous semiconductors have been developed; however, they have not shown high hole mobilities comparable to the existing *n*-type amoprhous semicondutors. Therefore, one objective of this study is to explore high-mobility *p*-type ionic amorphous semiconductors, for which the key is to desigin a highly-dispersed VBM. Ionic arsenides are expected to be potential candidates because the largely-spread 5*p* orbials of arsenic anion would shallow and high-diespesed VBM for a hole transport path even in an amorphous structue. In this study, amorphous $BaZn_2As_2$ was examinied.

SnS is expected as an absorber material for solar cells, suffers from the doping asymmetry problem, as reviewed in Section 1.1.3; that is, it is naturally doped *p*-type, but hardly *n*-type. However, *n*-type SnS is desired to construct *p*-SnS/*n*-SnS homojunctions for high performance solar cells. Desipte much efforts for *n*-type doping in SnS, no realialbe *n*-type SnS have been attained. On the other hand, Cs_2SnI_6, a rarely studied perovskite variant, is gaining interest for photovoltaic applications due to its nontoxicity and chemical stability. Cs_2SnI_6 is naturally *n*-type doped and has not shown intrinsic *p*-type conduction. The other objective of this study is to clarify the origins of the doping asymmetry problem in theses novel compound semiconductors including SnS and Cs_2SnI_6 and design effective counter doping routes for these semiconductors.

1.3 Outline of the Thesis

In Chapter 2 “High-Mobility *p*-Type Amorphous Semiconductor $BaZn_2As_2$,” amorphous $BaZn_2As_2$ (a-$BaZn_2As_2$) thin films were fabricated by pulsed laser deposition (PLD). The structural, optical, and electrical properites of a-$BaZn_2As_2$ were investiaged. It was found

that the a-$BaZn_2As_2$ films exhibited band gaps of > 1.04 eV and *p*-type conduction with high hole mobilities ~10 $cm^2\ V^{-1}\ s^{-1}$. Further, growth of crystalline β-$BaZn_2As_2$ films and the fundermental properties ofβ-$BaZn_2As_2$ were also dicussed.

In Chapter 3 "Chemical Origins of the Narrow Band Gap in β-$BaZn_2As_2$," the electronic structure and chemical origins of the narrow band gap in β-$BaZn_2As_2$ were studied in comparison with a similar compound LaZnAsO with a larger band gap (1.5 eV) based on the chemical bonding analyses probed by 6 keV hard X-ray photoemission spectroscopy, hybrid density functional theory (H/DFT) calculations, and the ligand theory.

In Chapter 4 "Origins of Doping Assymmetry in SnS," the defect physics of SnS was investigated by defect calculatons based on DFT. Particularly, the origins of the doping asymmetry in SnS were discussed based on the DFT calculation results and the band alignment diagram. Further, aliovalent Sb^{3+} and Bi^{3+} doping in SnS was also theoretically assessed and found not effective for *n*-type doping.

In Chapter 5 "*n*-Type Conversion of SnS by Geometrical Doping Route," *n*-type conduction was attained in isovalently Pb-substituted SnS films. The Pb substitution reduced the VBM and CBM, and thus reduced the severity of the doping asymmetry. More importantly, DFT calcuations suggest that the substitution invoked a geometrical size effect that enlarges the interlayer distance and subquently induces the formation of Sn and Pb cation interstials, which result in the electron doping.

In Chapter 6 "Electronic Structure of a Perovskite Variant Cs_2SnI_6", the electronic structure of a recently-reported perovskite variant Cs_2SnI_6 was studied by HDFT calculations. The real oxidation state of Sn in Cs_2SnI_6 was revealed closer to +2 similar to that in $CsSnI_3$, rather than +4 expected from a simple ionic model of $Cs^+_2Sn^{4+}I^-_6$. The chemical stability and origin of the band gap were discussed by bonding nature analysis.

In Chapter 7 "Intrinsic Defects in a Perovskite Variant Cs_2SnI_6," HDFT calculations were performed to investigate the properties of intrinsic defects and the doping mechanism in Cs_2SnI_6. Iodine vacancy and tin interstitial were found to be the dominant defects for the intrinsic *n*-type conduction in Cs_2SnI_6. It was found that *p*-type conduction is difficult in Cs_2SnI_6 because of its too shallow VBM (i.e. too large *IP*). The origin of the high shallow VBM was also discussed by chemical bonding analysis in comparison with other related compounds.

In Chapter 8 "General Conclusions", this study is summarized and future perspective is described.

References

[1] K. L. Chopra, S. Major, and D. K. Pandya, Thin Solid Films **102**, 1 (1983).

[2] T. Minami, Thin Solid Films **516**, 5822 (2008).

[3] H. Kim, C. M. Gilmore, A. Piqué, J. S. Horwitz, H. Mattoussi, H. Murata, Z. H. Kafafi, and D. B. Chrisey, J. Appl. Phys. **86**, 6451 (1999).

[4] I. Hamberg and C. G. Granqvist, J. Appl. Phys. **60**, R123 (1986).

[5] H. Nakazawa, Y. Ito, E. Matsumoto, K. Adachi, N. Aoki, and Y. Ochiai, J. Appl. Phys. **100**, 093706 (2006).

[6] H. Hosono, N. Kikuchi, N. Ueda, and H. Kawazoe, J. Non. Cryst. Solids **198–200**, 165 (1996).

[7] S. Narushima, M. Orita, M. Hirano, and H. Hosono, Phys. Rev. B **66**, 035203 (2002).

[8] K. Nomura, A. Takagi, T. Kamiya, H. Ohta, M. Hirano, and H. Hosono, Nature **432**, 488 (2004).

[9] W. E. Spear and P. G. LeComber, Solid State Commun. **17**, 1193 (1975).

[10] T. Kamiya, K. Nomura, and H. Hosono, J. Disp. Technol. **5**, 273 (2009).

[11] T. Kamiya and H. Hosono, NPG Asia Mater. **2**, 15 (2010).

[12] T. Kamiya, K. Nomura, and H. Hosono, Sci. Technol. Adv. Mater. **11**, 044305 (2010).

[13] J. S. Park, W. J. Maeng, H. S. Kim, and J. S. Park, Thin Solid Films **520**, 1679 (2012).

[14] H. Kawazoe, M. Yasukawa, H. Hyodo, M. Kurita, H. Yanagi, and H. Hosono, Nature **389**, 939 (1997).

[15] H. Kawazoe, H. Yanagi, K. Ueda, and H. Hosono, MRS Bull. **25**, 28 (2000).

[16] H. Yanagi, H. Kawazoe, A. Kudo, M. Yasukawa, and H. Hosono, J. Electroceramics **4**, 407 (2000).

[17] A. N. Banerjee and K. K. Chattopadhyay, Prog. Cryst. Growth Charact. Mater. **50**, 52 (2005).

[18] P. Reinhard, A. Chirila, P. Blosch, F. Pianezzi, S. Nishiwaki, S. Buecheler, and A.N. Tiwari, IEEE J. Photovoltaics **3**, 572 (2013).

[19] B. K. Meyer, A. Polity, D. Reppin, M. Becker, P. Hering, P. J. Klar, T. Sander, C. Reindl, J. Benz, M. Eickhoff, C. Heiliger, M. Heinemann, J. Bläsing, A. Krost, S. Shokovets, C. Müller, and C. Ronning, Phys. Status Solidi B **249**, 1487 (2012).

[20] H. Sato, T. Minami, S. Takata, and T. Yamada, Thin Solid Films **236**, 27 (1993).

[21] H. Yanagi, S. Inoue, K. Ueda, H. Kawazoe, H. Hosono, and N. Hamada, J. Appl. Phys. **88**, 4159 (2000).

[22] K. Ueda, T. Hase, H. Yanagi, H. Kawazoe, H. Hosono, H. Ohta, M. Orita, and M. Hirano, J. Appl. Phys. **89**, 1790 (2001).

[23] H. Yanagi, T. Hase, S. Ibuki, K. Ueda, and H. Hosono, Appl. Phys. Lett. **78**, 1583 (2001).

[24] N. Duan, A. W. Sleight, M. K. Jayaraj, and J. Tate, **77**, 1325 (2000).

[25] A. Kudo, H. Yanagi, H. Hosono, and H. Kawazoe, Appl. Phys. Lett. **73**, 220 (1998).

[26] K. Ueda, S. Inoue, S. Hirose, H. Kawazoe, and H. Hosono, Appl. Phys. Lett. **77**, 2701 (2000).

[27] H. Hiramatsu, K. Ueda, H. Ohta, M. Orita, M. Hirano, and H. Hosono, Appl. Phys. Lett. **81**, 598 (2002).

[28] T. Kamiya, K. Ueda, H. Hiramatsu, H. Kamioka, H. Ohta, M. Hirano, and H. Hosono, Thin Solid Films **486**, 98 (2005).

[29] P. Schröer, P. Krüger, and J. Pollmann, Phys. Rev. B **47**, 6971 (1993).

[30] J. Lee, S. Cha, J. Kim, H. Nam, S. Lee, W. Ko, K.L. Wang, J. Park, and J. Hong, Adv. Mater. **23**, 4183 (2011).

[31] M. Joseph, H. Tabata, and T. Kawai, Jpn. J. Appl. Phys. **38**, L1205 (1999).

[32] A. Tsukazaki, A. Ohtomo, T. Onuma, M. Ohtani, T. Makino, M. Sumiya, K. Ohtani, S. F. Chichibu, S. Fuke, Y. Segawa, H. Ohno, H. Koinuma, and M. Kawasaki, Nat. Mater. **4**, 42 (2005).

[33] Y. Ogo, H. Hiramatsu, K. Nomura, H. Yanagi, T. Kamiya, M. Hirano, and H. Hosono, Appl. Phys. Lett. **93**, 032113 (2008).

[34] Y. Ogo, H. Hiramatsu, K. Nomura, H. Yanagi, T. Kamiya, M. Kimura, M. Hirano, and H. Hosono, Phys. Status Solidi A **206**, 2187 (2009).

[35] S. Narushima, H. Mizoguchi, K. Shimizu, K. Ueda, H. Ohta, M. Hirano, T. Kamiya, and H. Hosono, Adv. Mater. **15**, 1409 (2003).

[36] T. Kamiya, S. Narushima, H. Mizoguchi, K. Shimizu, K. Ueda, H. Ohta, M. Hirano, and H. Hosono, Adv. Funct. Mater. **15**, 968 (2005).

[37] P. Qin, G. Fang, N. Sun, X. Fan, Q. Zheng, F. Chen, J. Wan, and X. Zhao, Thin Solid Films **519**, 4334 (2011).

[38] C.-W. Ou, Z. Y. Ho, Y.-C. Chuang, S.-S. Cheng, M.-C. Wu, K.-C. Ho, and C.-W. Chu, Appl. Phys. Lett. **92**, 122113 (2008).

[39] H. Hiramatsu, H. Yanagi, T. Kamiya, M. Hirano, N. Matsunami, K. Shimizu, and H. Hosono, Phys. Status Solidi A **205**, 2007 (2008).

[40] D. A. Neamen, *Semiconductor Physics and Devices: Basic Principles*, 3rd Ed. (McGraw-Hill, New York, 2003), pp. 115–117.

[41] S. B. Zhang, S.-H. Wei, and A. Zunger, Phys. Rev. B **63**, 075205 (2001).

[42] S. Lany, J. Osorio-Guillén, and A. Zunger, Phys. Rev. B **75**, 241203 (2007).

[43] Y. Yan, J. Li, S.-H. Wei, and M. M. Al-Jaassim, Phys. Rev. Lett. **98**, 135506 (2007).

[44] Y. Yan and S.-H. Wei, Phys. Status Solidi B **245**, 641 (2008).

[45] V. Avrutin, D. J. Silversmith, and H. Morkoç, Proc. IEEE **98**, 1269 (2010).

[46] F.-Y. Ran, Z. Xiao, H. Hiramatsu, H. Hosono, and T. Kamiya, Appl. Phys. Lett. **104**, 072106 (2014).

[47] P. Sinsermsuksakul, R. Chakraborty, S. B. Kim, S. M. Heald, T. Buonassisi, and R. G. Gordon, Chem. Mater. **24**, 4556 (2012).

[48] Y. Yan, S. B. Zhang, S. J. Pennycook, and S. T. Pantelides, Mater. Res. Soc. Symp. Proc. **666**, F2.6 (2001).

[49] Y. Yan, S. B. Zhang, and S. T. Pantelides, Phys. Rev. Lett. **86**, 5723 (2001).

[50] Y. R. Ryu, T. S. Lee, and H. M. White, Appl. Phys. Lett. **83**, 87 (2003).

[51] S. Limpijumnong, S. B. Zhang, S.-H. Wei, and C. H. Park, Phys. Rev. Lett. **92**, 155504 (2004).

[52] J. Li, S.-H. Wei, S.-S. Li, and J.-B. Xia, Phys. Rev. B **74**, 081201R (2006).

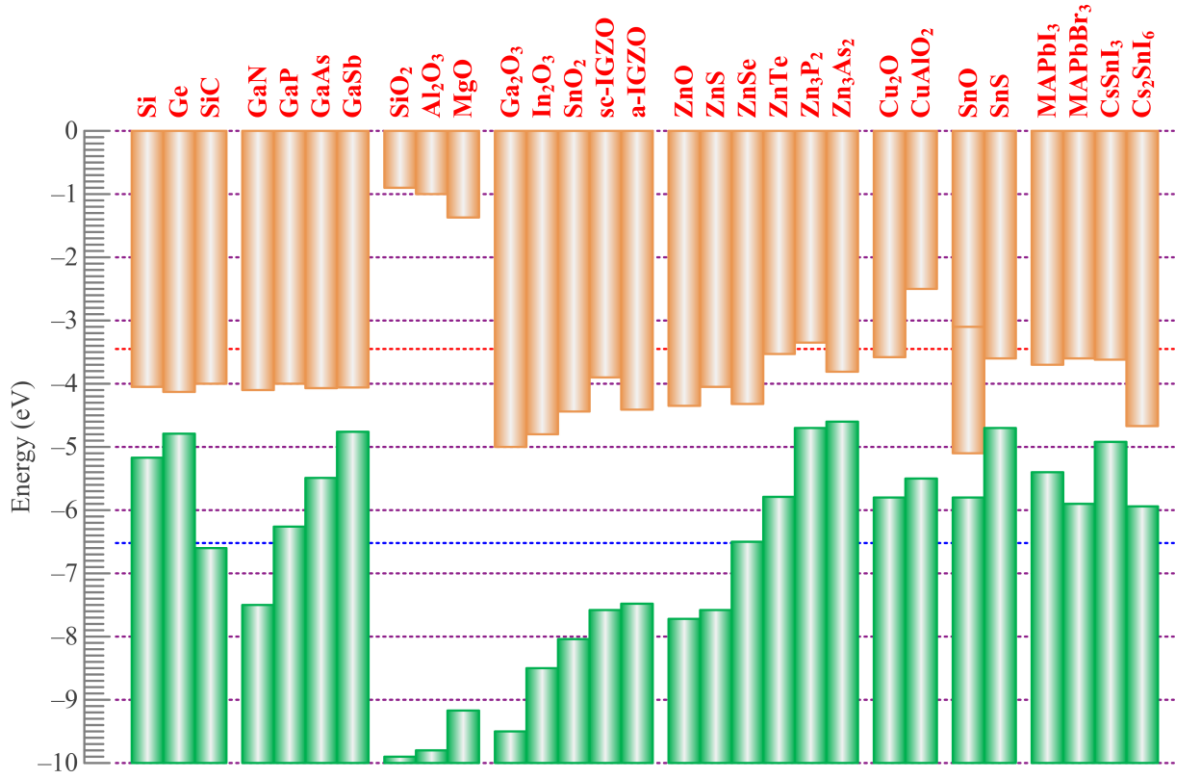

Figure 1.1. Band alignment based on the ionization potential (*IP*) and electron affinity (*EA*) from literatures.

Chapter 2

High-Mobility *p*-Type Amorphous Semiconductor $BaZn_2As_2$

2.1 Introduction

Amorphous semiconductors such as hydrogenated amorphous silicon (a-Si:H) have advantages over crystalline ones from the viewpoint of processing, e.g., low-temperature deposition and large-area uniformity, which enables developing large-area electronic devices such as solar cells and thin-films transistors (TFTs) for flat-panel displays [1]. In the last decade, *n*-type amorphous oxide semiconductors (AOSs) represented by amorphous In–Ga–Zn–O (a-IGZO) have widely been investigated and are now commercialized owing to their advantages such as high electron mobilities > 10 $cm^2\ V^{-1}\ s^{-1}$ [2–5] over the conventional amorphous semiconductors such as a-Si:H. On the other hand, *p*-type AOSs with high hole mobilities are important are desired to make high-performance all-AOS electronic devices based on CMOS circuits. Although some *p*-type AOSs such as amorphous xZnO·Rh_2O_3 (x = 0.5–2.0) [6,7], Cr_2O_3 [8], and SnO_2 [9] have been reported, their hole mobilities are very small, < 0.1 $cm^2\ V^{-1}\ s^{-1}$.

It is known that the valence band maximum (VBM) of most oxide semiconductors consists mainly of fully occupied 2*p* orbitals of oxygen anions with a large electronegativity. Hence the dispersion of VBM is small (i.e. the hole effective mass is large and the hole mobility is small) and the ionization potential (*IP*) is large (i.e. the hole

is energetically unstable), causing the *p*-type doping difficulty for oxide semiconductor, particularly, in an amorphous phase.

On the other hand, effective *p*-type doping and relatively high hole mobility have been attained in crystalline Cu_2O and SnO, because the occupied 3*d* orbitals of Cu^+ cation and the occupied Sn 5*s* orbitals of Sn^{2+} cation hybridize with 2*p* orbitals of oxygen anion, leading to the shallower and more dispersive VBMs in Cu_2O and SnO than other typical oxide semiconductors. Currently, crystalline Cu_2O and SnO can produce *p*-type channel TFTs exhibiting several $cm^2\ V^{-1}\ s^{-1}$ of field-effect mobilities [10−12]. Amorphous SnO *p*-channel TFTs have been also reported, but their TFT mobilies were only ~0.01 $cm^2\ V^{-1}\ s^{-1}$ [13]. Therefore, the exploration of high-mobility *p*-type amorphous semiconductors is still of extreme significance for developing large-area electronic devices.

To explore high-mobility *p*-type amorphous semiconductors, the following properties would be essential to select potential candidate compounds; (i) the VBM is shallow enough so that *p*-type doping can readily attained, (ii) the VBM is dispersive so that the hole moblitity can be high, and (iii) the compound is mainly ionic so that the hole transport passes can be retained in the amorphous structure [14,15]. It is considered that ionic metal pnictides such as Zn_3P_2 and Zn_3As_2, the VBMs of which consist mainly of largely-spread *p* orbitals of pnictogen anions, should satisfy the above requirements (see Fig. 1.1) and would have the potential for high-mobility *p*-type amorphous semiconductors. Here, ternary pnictide $BaZn_2As_2$ rather than binary Zn_3As_2 is finally selected as a candidate compound, because it would be easier for the former one to form a stable amorphous structure due to its higher melting/crystallization temperatures [16,17]. Further, $BaZn_2As_2$ crystallizes into two phases, i.e., orthorhombic α-$BaZn_2As_2$ (space group *Pnma*) [16] and tetragonal β-$BaZn_2As_2$ (space group *I*4/*mmm*) [17] as shown in the right of Fig. 2.1. The

β-$BaZn_2As_2$ phase is isostructural to the "122" iron-based superconductors such as (Ba,K)Fe_2As_2 [18,19] and would be interested for developing new electronic funtions; e.g., Zhao *et al.* [20] have synthesized polycrystalline (Ba,K)$(Zn,Mn)_2As_2$ for diluted magnetic semiconductors.

In this chapter, amorphous $BaZn_2As_2$ (a-$BaZn_2As_2$) thin films were fabricated by pulsed laser deposition (PLD). The structural, optical, and electrical properites of a-$BaZn_2As_2$ were investiaged. The a-$BaZn_2As_2$ films exhibited band gaps of > 1.04 eV and *p*-type conduction with high hole mobilities from 1 to ~10 $cm^2\ V^{-1}\ s^{-1}$. Further, the crystallization of a-$BaZn_2As_2$ and the fundermental properties of crystallized β-$BaZn_2As_2$ were also dicussed.

2.2 Experimental and Computational Details

2.2.1 Target Fabrication

Thin films were grown by PLD. The $BaZn_2As_2$ PLD targets were synthesized through a solid-state reaction from elementary Ba, Zn and As. Ba pieces, fresh Zn powders, and As powders, which were mixed at the stoicheometric ratio, sealed in an evacurated quartz tube, and heated at 700 °C for 20 hours. The obtained reaction product was ground, pressed into pellets (8 mm in diameter), and further pressed with a cold isostatic press (CIP) apparatus at 250 MPa. Then, the pellets were sealed in evacurated quartz tubes and anneled at 700 °C for 20 hours, and then furnace-cooled to room temperatue (RT) to obtain α-$BaZn_2As_2$. To obtain β-$BaZn_2As_2$ phase, the pellets were annealed at a higher temperatue of 1000 °C and rapidly quenched by being droped into water to stablize the metastable β-$BaZn_2As_2$ phase. All the target fabrication processes except for the CIP, the sealing and the heating were conducted in an argon-filled glove box. Besides, to abtain stoichometric amorphous

$BaZn_2As_2$ thin films, a composition-optimized Zn-rich target (nominal atomic ratio is Ba: Zn: As = 1: 4.0: 2.5) was needed and fabricated by almost the same way except for a lower anneling temperature for the pellet (500 ^oC) to avoid Zn precipitation.

2.2.2 Thin Film Growth

~100 nm-thick amorphous $BaZn_2As_2$ (a-$BaZn_2As_2$) thin films were deposited on silica glass substrates at room temperature (RT) by PLD using a KrF excimer laser (λ = 248 nm; pulse duration = 20 ns; repletion frequency = 10 Hz). A composition-optimized Zn-rich target (the nominal atomic ratio of Ba: Zn: As = 1.0: 4.0: 2.5) was used to obtain nearly stoichiometric amorphous $BaZn_2As_2$ thin films. The as-deposited a-$BaZn_2As_2$ films were confirmed to be insulating and post-annealing was conducted to abtain electrical conductivity. For this, the a-$BaZn_2As_2$ films were annealed at T_{ann} = 300–500 °C for 1 h in evacuated silica-glass ampules, where a small amount of Zn_3As_2 powder was contained to suppress the evaporation of Zn and As elements during the annealing process.

Additionally, expitaxial β-$BaZn_2As_2$ thin films were also grown by the reactive solid-phase epitaxy (R-SPE) method [21,22]. Firstly, a metallic Zn layer (~ 5 nm in thickness) was deposited on a single-crystal MgO (001) at RT by PLD, followed by deposition of an a-$BaZn_2As_2$ layer at RT in the same PLD chamber. Next, the a-$BaZn_2As_2$ / Zn / MgO sample was covered by an MgO (001) plate and annealed at 900 ^oC for 30 minutes in an argon-filled stainless steel tube, where a small amount of Zn_3As_2 powders was contained to suppress the evaporation of the Zn and As elements during annealing.

2.2.3 Characterization

X-ray diffraction (XRD) patterns of the bulk samples were measured with a conventional powder XRD instrument (RINT2500, Rigaku). The temperature (T)

dependence of dc electrical conductivity (σ) of the β-$BaZn_2As_2$ sample was measured by the conventional four-probe method with a physical property measure measurement system (PPMS, Quantum Design) up to 400 K.

Crystalline quality and orientation of the grown films were examined with a high-resolution XRD (HR-XRD) instrument (Smart Lab, Rigaku). Out-of-plane ($2\theta/\omega$ synchronous scan) and in-plane ($2\theta\chi/\phi$ synchronous scan) XRD patterns were measured to determine epitaxial relationships between the films and the MgO substrates and to calculate lattice parameters. Chemical compositions were determined by X-ray fluorescence (ZSX-100e, Rigaku) with a polycrystalline sample as a reference. Optical absorption spectra from ultraviolet to near-infrared region were recorded in air using a conventional spectrophotometer (U4100, Hitachi), and those in the mid-infrared region were performed in vacuum with a Fourier transform infrared (FTIR) spectrometer (Vertex 70v, Bruker).

2.3 Results and Discussion

2.3.1 Structural Properties of Amorphous $BaZn_2As_2$ Films

The XRD patterns of $BaZn_2As_2$ bulk samples are shown in the bottom of Fig. 2.1. The one synthesized at 700 °C crystallized into the orthorhombic α-$BaZn_2As_2$ phase; while the one synthesized at 1000 °C crystallized into the β-$BaZn_2As_2$ phase, which had been stabilized by the water quenching process. These results are consistent with the literatures [16,17]. The XRD patterns of the $BaZn_2As_2$ films are shown in the top of Fig. 2.1. The pattern of the as-deposited film showed no sharp diffraction peak attributable to the crystalline α- and β-$BaZn_2As_2$ phases. The halo peak around ~21° is assigned to the silica glass substrate. These features indicate that the as-deposited film was amorphous. The films annealed at

300 and 400 °C kept the amorphous phase since their XRD patterns are unchanged as that of the as-deposited one. For the film annealed at 500 °C, the XRD pattern has an extra wide halo peak around ~35° and three weak diffraction peaks at 16.2°, 26.1° and 26.2°. Although the former cannot be attributed to the crystalline structure, the later three are the α-$BaZn_2As_2$ 002, α-$BaZn_2As_2$ 103 and β-$BaZn_2As_2$ 004 diffraction peaks, respectively, indicating that crystallization into polymorphic α- and β-$BaZn_2As_2$ initiated in the a-$BaZn_2As_2$ film by the 500 °C annealing. Table 1 shows the chemical composition of two typical film samples. Both the films had nearly stoichiometric compositions, which were not changed significantly during the annealing process.

2.3.2 Optical Properties of Amorphous $BaZn_2As_2$ Films

Figure 2.2a shows optical absorption spectra. The absorption coefficients level off in the high energy region at > 3.0 eV independent of T_{ann}. Figure 2.2b shows the $(\alpha h\nu)^{1/2}$–$h\nu$ plots (Tauc's plots) to evaluate optical bandgaps of the a-$BaZn_2As_2$ films. The as-deposited a-$BaZn_2As_2$ exhibits a distinct linear region in the Tauc's plot. Extrapolating this linear region to the abscissa yields the Tauc's bandgap of 1.04 eV, which is close to those of simple zinc arsenides (e.g., 0.99 eV for Zn_3As_2 [23] and 0.98 eV for $ZnAs_2$ [24]). For the annealed films, the absorption spectra slightly shifted toward higher energies. The bandgaps of the films annealed at 300, 400 and 500 °C were 1.24, 1.32 and 1.35 eV, respectively (i.e., the post-annealing increased the bandgap by 0.20–0.31 eV). These results indicate that the band gap are tunable with T_{ann}, the reason for which has not been revealed, but would be attributed to structural relaxation in the annealing process.

2.3.3 Electrical Properties of Amorphous $BaZn_2As_2$ Films

The as-deposited a-$BaZn_2As_2$ films were highly resistive. To achieve electrical conduction

in a-$BaZn_2As_2$ films, post-annealing was performed. Figure 2.3 shows the electrical properties of the annealed a-$BaZn_2As_2$ films. All the annealed films exhibited *p*-type conduction. Figure 2.3a plots the hole mobilities (μ_h) as a function of T_{ann}, which exhibits an increasing trend with T_{ann}. At T_{ann} = 300 ºC, μ_h of 0.6–1.6 $cm^2\ V^{-1}\ s^{-1}$ were obtained. For higher T_{ann} = 400 ºC, μ_h was increased to 1.8–9.8 $cm^2\ V^{-1}\ s^{-1}$, which were comparable with those of *n*-type AOSs [5]. At T_{ann} = 500 ºC, μ_h further increased to 20.2 $cm^2\ V^{-1}\ s^{-1}$, which would be attributed partly to the existence of the crystallized β-$BaZn_2As_2$ phase. The hole densities (*p*) and conductivities (σ) were at the orders of 10^{18}–10^{19} cm^{-3} and 1–20 S cm^{-1}, as shown in Fig. 2.3b and 2.3c, respectively. No clear T_{ann} dependences were observed for *p* and σ. Figure 2.3d plots μ_h as a function of *p*, exhibiting a decreasing trend. There would be two major mechanisms that affect the hole mobility. That is, Fig. 2.3a suggests that film quality would be improved by higher T_{ann} annealing, and Fig. 2.3d implies that carrier scattering due to ionized acceptors deteriorates μ_h at higher *p* [25], and provides an expectation that further reduction of *p* will achieve higher μ_h.

2.3.4 Epitaxial Growth and Narrow Band Gap of Crystalline β-$BaZn_2As_2$

The HR-XRD patterns of the $BaZn_2As_2$ thin film annealed at 900 ºC are shown in Fig. 2.4a. In the out-of-plane XRD pattern (the top panel of Fig. 2.4a), only intensive β-$BaZn_2As_2$ 00*l* along with MgO 001 diffraction peaks were observed. In the in-plane HR-XRD pattern (the bottom panel of Fig. 2.4a), only $BaZn_2As_2$ 200 and 400 diffraction peaks together with MgO 200 and 400 diffraction peaks were observed. These results indicate epitaxial β-$BaZn_2As_2$ thin films were obtained by the R-SPE process with the epitaxial relationship of out-of-plane $BaZn_2As_2$ (00*l*) // MgO (001) and in-plane $BaZn_2As_2$ (200) // MgO (200). Note that no diffraction peak of metallic Zn was observed, indicating the ultrathin Zn layer should have been sacrificed in the R-SPE process and played as an epitaxy initializer,

similar to the roles of epitaxial Cu and ZnO layers for epitaxial growth of LaCuOS [21] and $InGaO_3(ZnO)_m$ [22], respectively.

The optical absorption spectrum of the epitaxial β-$BaZn_2As_2$ film measured by a conventional spectrophotometer is shown in Fig. 2.3b. An absorption edge was observed at <1.0 eV; but the absorption coefficient (α) didn't vanish to zero or reach a minimum until 0.5 eV, suggesting the band gap should be less than 0.5 eV. To evaluate such small band gap for β-$BaZn_2As_2$, FTIR spectra were further measured in the lower energy region from 0.04 eV to 0.93 eV as shown in Fig. 2.4c. A strong absorption peak is observed in 0.05–0.20 eV for the film / substrate sample. This peak is caused by MgO substrate (the blue dashed lines in Fig. 2.4c), which hinders the band gap determination more or less. By subtracting the absorption spectrum of the MgO substrate ($\alpha_{substrate}$), the net absorption of the film ($\alpha_{film} - \alpha_{substrate}$) is plotted by the red dashed line, showing that an absorption edge would be at 0.23 eV. The band gap was further examined from the intrinsic region of electrical conductivity (σ) of a polycrystalline β-$BaZn_2As_2$ sample. The σ (in logarithmic coordinate) vs. $1/T$ Arrhenius plot shown in Fig. 2.4d exhibits two linear regions between 10 and 50 K and between 190 and 310 K, respectively. The high-T linear region should be attributed to the intrinsic region of σ and can be expressed by $\sigma = \sigma_0 \exp(-E_a/k_B T)$, where σ_0 is the pre-exponential constant, k_B is the Boltzmann constant, and E_a is the activation energy. The low-T linear region could be attributed, for example, to the variable range hopping (VRH) model, the saturation regime of the ionization of donors, and very shallow donors. For example, the σ–T data were fitted by a combined expression $\sigma(T) = \sigma_0 \exp(-E_a/k_B T) + \sigma_{vrh} \exp[-(T_0/T)^{1/4}]$, where the latter express the VRH model with constants σ_{vrh} and T_0 [26], as drawn by the red curve. The fit gave intrinsic E_a value of 0.114 eV and thus the band gap is $E_g = 2E_a = 0.23$ eV.

2.4 Conclusions

The a-$BaZn_2As_2$ thin films were grown by PLD. The optical band gap of a-$BaZn_2As_2$ was determined to be 1.04 eV in the as-deposited state, and increased up to 1.37 eV with increasing the annealing temperature to 500 ºC. The annealed films exhibited *p*-type conductivities with hole mobilities up to ~10 $cm^2V^{-1}s^{-1}$ by keeping amorphous structures, and partially-crystallized films exhibited higher hole mobilities ~20 $cm^2V^{-1}s^{-1}$. This achievement indicates that high hole mobilities would be attained even in amorphous semiconductors if heavy anions are employed. Crystallization was observed in the a-$BaZn_2As_2$ films annealed at $T_{ann} \geq 500$ ºC and epitaxial growth of β-$BaZn_2As_2$ films was achieved by the R-SPE method. The band gap of β-$BaZn_2As_2$ was estimated to be 0.23 eV, unexpectedly much smaller even than a-$BaZn_2As_2$.

References

[1] R. A. Street, *Hydrogenated amorphous silicon*, Cambridge University Press, Cambridge (1991).

[2] E. Fortunato, P. Barquinha, A. Pimentel, A. Gonçalves, A. Marques, R. Martins, and L. Pereira, *Appl. Phys. Lett.* **85**, 2541 (2004).

[3] K. Nomura, H. Ohta, K. Ueda, T. Kamiya, M. Hirano, and H. Hosono, *Science* **300**, 1269 (2003).

[4] K. Nomura, H. Ohta, A. Takagi, T. Kamiya, M. Hirano, and H. Hosono, *Nature* **432**, 488 (2004).

[5] T. Kamiya, K. Nomura, and H. Hosono, Sci. Technol. Adv. Mater. **11**, 044305 (2010).

[6] S. Narushima, H. Mizoguchi, K. Shimizu, K. Ueda, H. Ohta, M. Hirano, T. Kamiya, and H. Hosono, *Adv. Mater.* **15**, 1409 (2003).

[7] T. Kamiya, S. Narushima, H. Mizoguchi, K. Shimizu, K. Ueda, H. Ohta, M. Hirano, and H. Hosono, Adv. Funct. Mater. **15**, 968 (2005).

[8] P. Qin, G. Fang, N. Sun, X. Fan, Q. Zheng, F. Chen, J. Wan, and X. Zhao, *Thin Solid Films* **519**, 4334 (2011).

[9] C.-W. Ou, Z. Y. Ho, Y.-C. Chuang, S.-S. Cheng, M.-C. Wu, K.-C. Ho, and C.-W. Chu, *Appl. Phys. Lett.* **92**, 122113 (2008).

[10] Y. Ogo, H. Hiramatsu, K. Nomura, H. Yanagi, T. Kamiya, M. Hirano, and H. Hosono, *Appl. Phys. Lett.* **93**, 032113 (2008).

[11] M. Liao, Z. Xiao, F.-Y. Ran, H. Kumomi, T. Kamiya, and H. Hosono, ECS J. Solid State Sci. Technol. **4**, Q26 (2015).

[12] K. Matsuzaki, K. Nomura, H. Yanagi, T. Kamiya, M. Hirano, and H. Hosono, *Appl. Phys. Lett.* **93**, 202107 (2008).

[13] C.-W. Ou, Dhananjay, Z. Y. Ho, Y.-C. Chuang, S.-S. Cheng, M.-C. Wu, K.-C. Ho, and C.-W. Chu, *Appl. Phys. Lett.* **92**, 122113 (2008).

[14] H. Hosono, N. Kikuchi, N. Ueda, and H. Kawazoe, J. Non. Cryst. Solids **198-200**, 165 (1996).

[15] H. Hosono, J. Non. Cryst. Solids **352**, 851 (2006).

[16] P. Klüfers, A. Mewis, Z. Naturforsch. **33b**, 151 (1978).

[17] A. Hellmann, A. Löhken, A. Wurth, A. Mewis, Z. Naturforsch. **62b**, 155 (2007).

[18] M. Rotter, M. Tegel, and D. Johrendt, Phys. Rev. Lett. **101**, 107006 (2008).

[19] T. Katase, H. Hiramatsu, H. Yanagi, T. Kamiya, M. Hirano, and H. Hosono, Solid State Commun. **149**, 2121 (2009).

[20] K. Zhao, Z. Deng, X.C. Wang, W. Han, J.L. Zhu, X. Li, Q.Q. Liu, R.C. Yu, T. Goko, B. Frandsen, L. Liu, F.L. Ning, Y.J. Uemura, H. Dabkowska, G.M. Luke, H. Luetkens,

E. Morenzoni, S.R. Dunsiger, A. Senyshyn, P. Böni, C.Q. Jin, Nat. Commun. **4**, 1442 (2013).

[21] H. Hiramatsu, K. Ueda, H. Ohta, M. Orita, M. Hirano, and H. Hosono, Appl. Phys. Lett. **81**, 598 (2002).

[22] H. Ohta, K. Nomura, M. Orita, M Hirano, K. Ueda, T. Suzuki, Y. Ikuhara, and H. Hosono, Adv. Funct. Mater. **13**, 139 (2003).

[23] J. Misiewicz and J. M. Pawlikowski, Solid State Commun. **32**, 687 (1979).

[24] A. V. Mudryi, A. I. Patuk, I. A. Shakin, A. E. Kalmykov, S. F. Marenkin, and A. M. Raukhman, Mater. Chem. Phys. **44**, 151 (1996).

[25] D. A. Neamen, *Semiconductor Physics and Devices: Basic Principles*, 3rd Ed. (McGraw-Hill, New York, 2003), pp. 115–117.

[26] N. F. Mott, Philos. Mag. **19**, 835 (1969).

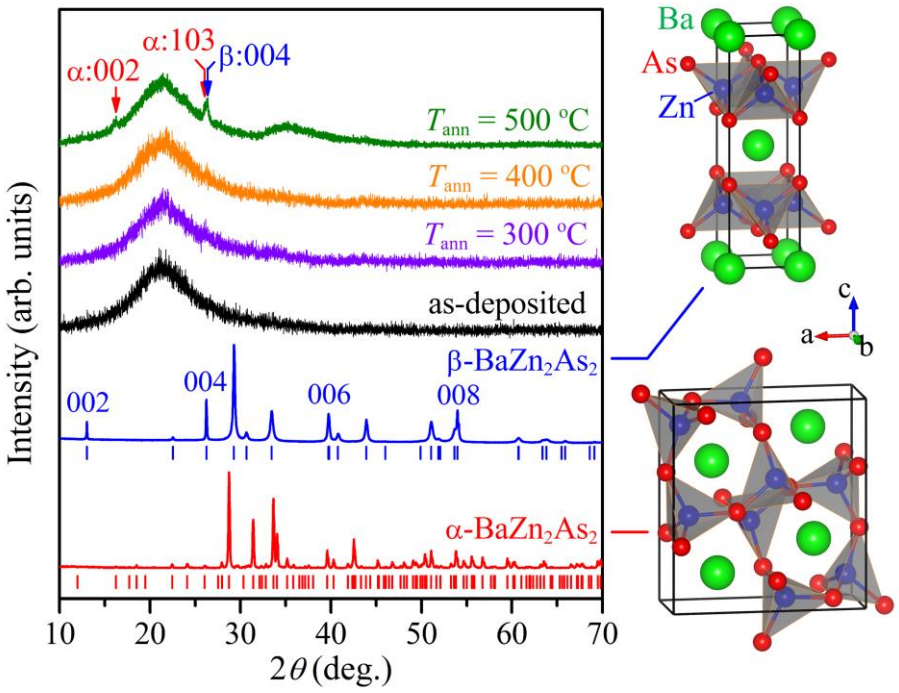

Figure 2.1. XRD patterns of $BaZn_2As_2$ films deposited at room temperature and annealed at various temperature (T_{ann}) along with those of polycrystalline α- and β-$BaZn_2As_2$ bulks for comparison. The crystal structures of α-$BaZn_2As_2$ (α-$BaCu_2S_2$-type, space group *Pnma*) and β-$BaZn_2As_2$ ($ThCr_2Si_2$-type, space group *I4/mmm*) are also shown on the right.

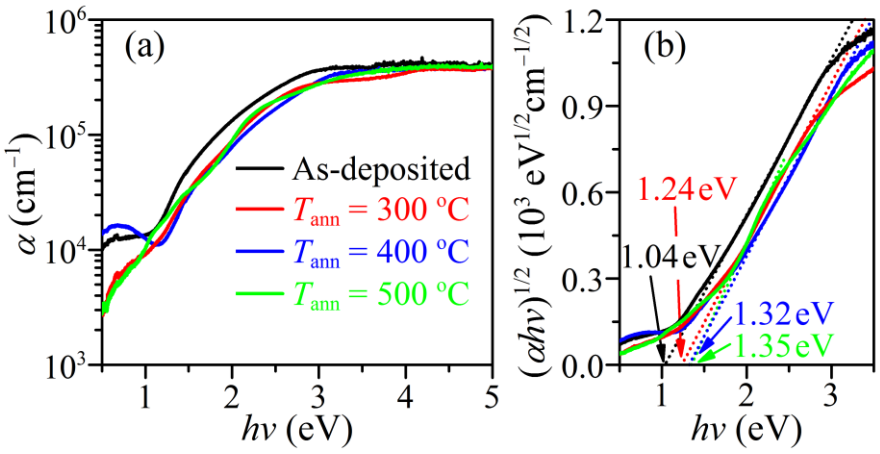

Figure 2.2. Optical properties of amorphous $BaZn_2As_2$. (a) Optical absorption spectra and (b) $(\alpha h\nu)^{1/2} - h\nu$ plots of as-deposited and annealed films. The obtained optical bandgaps are given in (b).

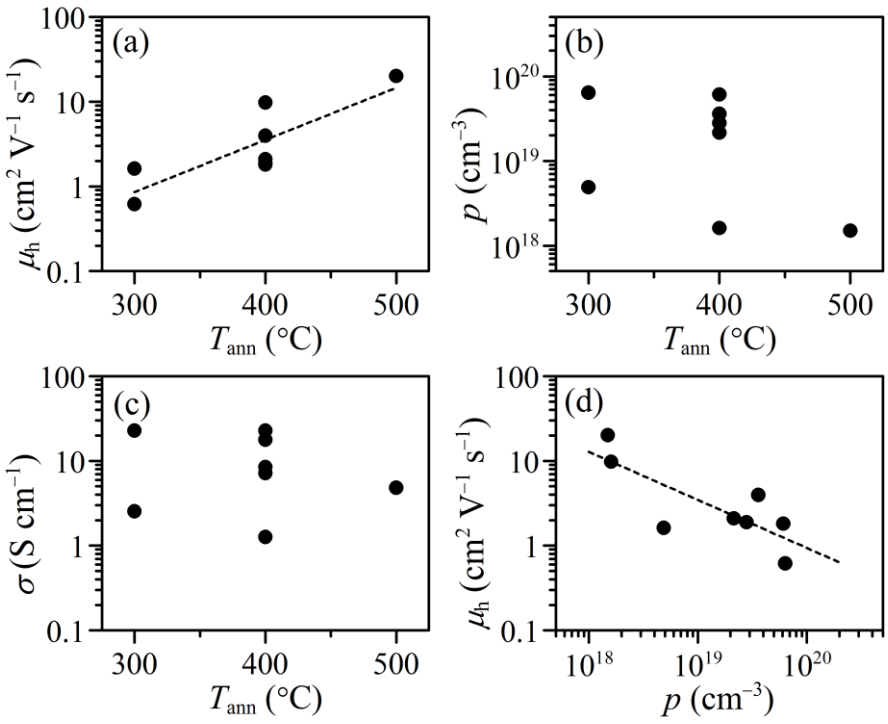

Figure 2.3. Electrical properties of amorphous $BaZn_2As_2$. (a) Hole mobility (μ_h), (b) hole density (p), and (c) conductivity (σ) of amorphous $BaZn_2As_2$ films annealed at various temperatures (T_{ann}). (d) μ_h plotted as a function of p.

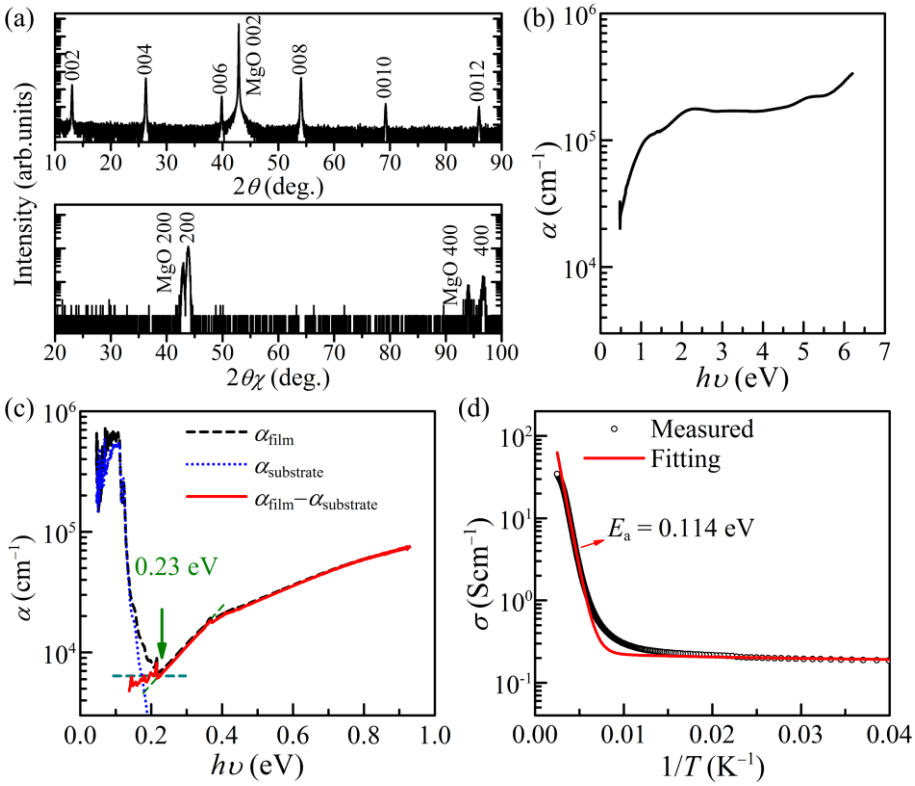

Figure 2.4. (a) Out-of-plane and in-plane HR-XRD pattern of $BaZn_2As_2$ thin film after annealing at 900 °C. (b and c) Optical spectra of epitaxial β-$BaZn_2As_2$ film (b) in near-infrared–ultraviolet region and (c) in mid infrared region. (d) T dependence of σ for polycrystalline β-$BaZn_2As_2$ sample. The red curve is a fit to $\sigma(T) = \sigma_0\exp(-E_a/k_BT) + \sigma_{vrh}\exp[-(T_0/T)^{1/4}]$.

Chapter 3

Chemical Origins of the Narrow Band Gap in β-$BaZn_2As_2$

3.1 Introduction

Layered mixed-anion compounds including LaCu*Ch*O (*Ch* = S, Se, Te) [1–2], La$T_M P_n$O (T_M = Mn, Zn; *Pn* = P, As) [3–5] and LaT_M'P_nO (T_M' = Fe, Ni; *Pn* = P, As) [6–8] exhibit a wide variety of electronic phenomena such as wide gap *p*-type semiconduction and superconductivity, making them attractive for a new platform to explore functional materials. These compounds have the general chemical formula *LnMAX* (*Ln* =lanthanide, *M* = transition metal, *A* = chalcogen or pnictogen, *X* = O, F or H), which are called "1111-type" compounds and have the tetragonal ZrCuSiAs-type structure (space group *P*4/*nmm*). In particular, an interesting feature of these compounds is that they have a two-dimensional crystal structure composed of alternating [*MA*] and [*LnX*] layers; the former forms a carrier conduction path and the latter forms a wider band gap than the conduction layer and behaves like a carrier transport barrier.

Alternatively, similar layered-structure compounds (i.e., composed of a narrow band gap [*MA*] layer) have also been found; a representative one is called "122-type" compounds expressed by the chemical formula AeM_2Pn_2 (*Ae* = alkaline earth). Similar to the 1111-type compounds, the properties of AeM_2Pn_2 change drastically if the type of the transition metal *M* is varied. For example, AeM_2Pn_2 behave as superconductors (for Fe [9,10] and Ni [11]), ferromagnetic metals (for Co [12]), antiferromagnetic metals (for Cr

[13]), diamagnetic metals (for Cu [14]), antiferromagnetic semiconductors (for Mn [15–18]), and nonmagnetic semiconductors (for Zn [19]). Most of them crystallize into the tetragonal $ThCr_2Si_2$ structure with the space group *I*4/*mmm* [20]. On the other hand, $BaZn_2As_2$ has two crystalline phases; the low-temperature orthorhombic phase α-$BaZn_2As_2$ [21] (α-$BaCu_2S_2$-type structure, the space group *Pnma*) and the high-temperature tetragonal phase β-$BaZn_2As_2$ [22] (the 122-type one, the space group *I*4/*mmm*) (Fig. 3.1a). Recently, $(Ba_{1-x}K_x)(Zn_{1-y}Mn_y)_2As_2$ was reported to be a good diluted magnetic semiconductor, in which the tetragonal phase is stabilized by the doping of 10% K or Mn [19].

It is known that the anion–anion chemical bonding influences the ground states of 122-type compounds significantly and is intertwined with the formation of the ferromagnetic quantum critical point and superconductivity [23,24]. In Chapter 2, the band gap of β-$BaZn_2As_2$ was determined to be 0.23 eV [25], which is extremely narrow compared with that of the similar 1111-type compound, LaZnAsO (1.5 eV), [4] although they have similar layered structures where the common [ZnAs] layers are expected to form the band gap for both the conduction band minimum (CBM) and valence band maximum (VBM). The similar difference in the band gap is observed also in the Mn-based compounds (i.e. 0.14 eV for $BaMn_2P_2$ [15], 1.7 eV for LaMnPO [5], 0.06 eV for $BaMn_2As_2$ [16], 1.5 eV for LaMnAsO [5], 0.06–0.20 eV for $BaMn_2Sb_2$ [17,18], 1.0 eV for LaMnSbO [5]). Further it has been reported that simple zinc arsenides have much larger band gaps as well (e.g., 0.99 eV for Zn_3As_2 [26] and 0.98 eV for $ZnAs_2$ [27]). Recently, first-principles calculations for the α- and β-$BaZn_2As_2$ phases reported that they have complicated and highly anisotropic electronic structures because of the unusual cation–anion and anion–anion hybridizations [28]; however, it does not provide an

explanation for the extreme narrow band gap of β-$BaZn_2As_2$.

In this chapter, the chemical origins of the narrow band gap of β-$BaZn_2As_2$ in comparison with LaZnAsO are discussed based on the chemical bonding nature probed by 6 keV hard X-ray photoemission spectroscopy, hybrid density functional calculations, and the ligand theory. It is found that the anion-anion hybridization between adjacent [ZnAs] layers induces a secondary splitting of the outer orbitals of As atoms and widens the VB. In addition, the *d* orbitals of the heavy alkaline earth Ba ion form a deep conduction band (CB) minimum (CBM) due to the non-bonding nature of the Ba $5d_{x2-y2}$ orbitals. These two factors provide a quantitative explanation for the narrow band gap of β-$BaZn_2As_2$.

3.2 Computational Details

Density functional theory (DFT) and hybrid DFT (HDFT) calculations were performed using the projector augmented plane-wave method implemented in the Vienna *Ab initio* Simulation Program (VASP 5.3) [29]. The plane wave cutoff energy was set to 345.9 eV. A 5×5×2 *k*-mesh was used for tetragonal β-$BaZn_2As_2$ and LaZnAsO and a 5×5×3 *k*-mesh was used for trigonal *Ae*Zn_2As_2 crystals (*Ae* =Ba, Sr and Ca). For the exchange-correlation functional, first the local density approximation (LDA) and the Perdew–Burke–Ernzerhof (PBE96) [30] generalized gradient approximation (GGA) functional were examined; however, they underestimated the band gaps of β-$BaZn_2As_2$ and LaZnAsO (see Table 3.1). Then hybrid functionals were examined and it is found that the HSE06 [31,32] hybrid functional with the standard mixing parameter of 25% for the exact-exchange term provided reasonable results. Before the electronic structure calculations, variable-cell structure relaxations were performed using the respective functionals.

3.3 Results and Discussion

3.3.1 Crystal Structure Difference between β-$BaZn_2As_2$ and LaZnAsO

Figs. 3.1a and 3.1b show the crystal structures of β-$BaZn_2As_2$ and LaZnAsO, respectively. The literature structural parameters for β-$BaZn_2As_2$ [22] and LaZnAsO [33] are summarized in Table 3.1. The structures of the [ZnAs] layers are almost the same between β-$BaZn_2As_2$ and LaZnAsO, where each ($ZnAs_4$) tetrahedron is connected with four neighboring ($ZnAs_4$) tetrahedra by sharing their edges. On the other hand, a distinct difference can be found between these structures in Fig. 3.1c, where the coordination numbers of As atoms around an As atom is plotted as a function of As−As distances, d_{As-As}. The intralayer As−As distances (i.e., d_{in} and d_{out}, as denoted in Fig. 3.1a) are similar between β-$BaZn_2As_2$ and LaZnAsO (0.410–0.425 nm); whereas, the interlayer As−As distance (d_{inter}) for β-$BaZn_2As_2$ (0.370 nm) is much shorter than that for LaZnAsO (0.660 nm) owing to the different heights between the Ba ion and the LaO layer.

3.3.2 Electronic Structure Differences between β-$BaZn_2As_2$ and LaZnAsO

Table 3.1 summarizes the literature and calculated band gaps and lattice parameters for β-$BaZn_2As_2$ and LaZnAsO. While the LDA and PBE96 GGA functionals underestimated the band gaps, the HSE06 hybrid functional provided reasonable band gap values of 0.23 eV for β-$BaZn_2As_2$ and 1.38 eV for LaZnAsO, which are fairly close to the experimental values. Besides, the HSE06 also gave better structural parameters than the LDA and the PBE96. Therefore, I use the HSE06 calculation results for the following discussion.

The calculated total and projected densities of states (DOSs) for β-$BaZn_2As_2$ and LaZnAsO are shown in Figs. 3.2a and 3.2b. The CB of β-$BaZn_2As_2$ between CBM and CBM + 1.0 eV consists mainly of Ba 5*d* and As 4*d* hybridized with small portion of Zn 4*s* orbitals, which is highly dispersed as seen in the band structure in Fig. 3.2c. The CB of

LaZnAsO between CBM and CBM + 1.0 eV consists mainly of Zn 4*s* and As 4*d* orbitals with narrower dispersion as seen in Fig. 3.2d. Both compounds exhibit long CB tails in the total DOSs near CBM. The VB of β-$BaZn_2As_2$ consists mainly of As 4*p* orbital slightly hybridized with Zn 4*p* and Ba 5*d* orbitals; while that of LaZnAsO consists of As 4*p* orbitals slightly hybridized with Zn 4*p* orbitals in the shallow region (VBM to −3.6 eV), and the O 2*p* orbitals slightly hybridized with As 4*p* and La 5*d* orbitals in the deeper region (−3.6 to −6.0 eV). In particular, β-$BaZn_2As_2$ exhibits a long tail structure in the total DOS from −0.6 eV to the VBM.

From the band structures (Figs. 3.2c and 3.2d), it can be seen that the VB levels are split to four similar energy levels in β-$BaZn_2As_2$ and LaZnAsO at the Z point, which is mainly explained by the intralayer hybridizations between the As atoms. The two bands marked by the red symbols are bonding (σ) and antibonding (σ^*) σ states of As 4p_z orbitals, respectively; while the other two by the blue symbols are bonding (π) and antibonding (π^*) π states of As (4p_x, 4p_y) orbitals, respectively, as confirmed from the *lm*-decomposed DOSs of As 4*p* orbitals (the fifth panels of Figs. 3.2a and 3.2b). For β-$BaZn_2As_2$, each doubly degenerated orbital at the Z point splits into two bands along the *k* vector moving to the Γ point because the adjacent [ZnAs] layers interact with each other and form a bonding state and an antibonding state as indicated by σ^*_1 and σ^*_2 for example in Fig. 3.2c. For LaZnAsO, each band does not exhibit a significant energy split along the Z−Γ direction (Figure 3.3d), which is strikingly different from β-$BaZn_2As_2$. A comparison the different VB structures shows that the most significant difference near the VBM is found in the σ^*_2 band of β-$BaZn_2As_2$ formed because of the direct interlayer As 4p_z–As 4p_z anti-bond (see Fig. 3.3a), which is highly dispersed and the maximum energy level exceeds the π^*_2 band by 0.36 eV at the Γ point; i.e., As 4p_z mainly forms the *lm*-decomposed DOS of the

shallow VB region as seen in the fifth panel of Fig. 3.2b.

3.3.3 Origins of the Narrow Band Gap: I. Interlayer As−As Hybridization

As discussed above, the Γ point splitting of the VB in β-$BaZn_2As_2$ (denoted as secondary splitting hereafter) is caused by the direct hybridization between interlayer As atoms (schematically shown in Fig. 3.3a) because of the relatively short d_{inter} (0.370 nm). To further confirm this model, HSE06 calculations were performed for several hypothetical structures of β-$BaZn_2As_2$ with fixed [ZnAs] layers and varied d_{inter} values, as illustrated in Fig. 3.3a. The obtained band gap versus d_{inter} relation is summarized in Fig. 3.5b, and those band structures and DOSs are shown in Figs. 3.3c and 3.3d, respectively. First, the d_{inter} was decreased silightly from 0.370 to 0.360 nm. The secondary splitting of As 4*p* became wider because of the larger hybridization of the interlayer As atoms, which raised the VBM energy level as shown in the left panel in Fig. 3.3c. As a result, the band gap value is decreased to 0.04 eV. When the d_{inter} was increased to 0.380 nm, the secondary splitting of As 4*p* became smaller due to the reduced interlayer hybridizations, which led to a lowered VBM and an increased band gap of 0.40 eV. By further increasing the d_{inter} to 0.400 nm, the secondary splitting became further smaller and the σ^*_2 band did not pass across the π^*_2 band anymore (the right panel of Fig. 3.3c), which made the VBM structure more similar to that of LaZnAsO. Correspondingly, the "tail" structure near VBM faded away completely as seen in Fig. 3.3d. The resulted band gap was further increased to 0.66 eV. It is also confirmed that further increasing d_{inter} did not increase the band gap significantly. From the d_{inter} dependence of band gap summarized in Fig. 3.3b, it is concluded that the interlayer hybridization between the As $4p_z$ orbitals of adjacent layers is an origin of the narrow band gap in β-$BaZn_2As_2$, which decreases the band gap by ~0.43 eV (the band gap difference between the actual structure (d_{inter} = 0.370 nm) and that with d_{inter} being 0.400

nm). Here, it should be noted that the d_{inter} value in β-$BaZn_2As_2$ is shorter than that in LaZnAsO, but much longer than As–As bonds in single-bonded As_2-dimers (0.240–0.260 nm) [34] in such as $CaNi_2As_2$ [35]. This means that the interlayer hybridization of the As 4p_z orbitals in β-$BaZn_2As_2$ is much weaker than the As_2-dimers and is an intermediate case.

3.3.4 Origins of the Narrow Band Gap: II. Nonbonding Ba 5d_{x2-y2} Orbital

As discussed above for the PDOS in Fig. 3.2a, the Ba 5*d* orbitals contribute largely to the CB, in particular to the CBM structure. To examine the role of the Ba 5*d* orbitals on the narrow band gap, *lm*-decomposed DOSs for the five Ba 5*d* orbital (i.e. d_{xy}, d_{xz}, d_{yz}, d_{x2-y2} and d_{z2}) were further calculated and are shown in the rightmost panel of Fig. 3.2a. It is known well that the energy levels of outer *d* orbitals are split by the coordinating ligands, whose energy splits are understood qualitatively from the ligand symmetry (D_{4h} around Ba, as shown in Fig. 3.4a) by the group theory. The energy level of the edges of Ba 5*d* orbitals derived from the ligand theory and the *lm*-decomposed DOSs is schematically shown in Fig. 3.4c. As known from the *lm*-decomposed DOSs, the d_{x2-y2} has the lowest energy among the five *d* orbitals, and is even lower than that of Zn 4*s* orbital (the dashed line in Fig. 3.4c), and forms the CBM. As drawn in Fig. 3.4a, the d_{x2-y2} wave function extends to the interstitial spaces between the neighboring As 4*p* orbitals, minimizes the charge overlap with the As electrons, lowers its energy level due to the small Coulomb repulsion, and forms the deep CBM. Further, as the Ba 5d_{x2-y2}–As 4*p* states are non-bonding states due to the point-group symmetry and the restriction of the translational symmetry at the Ba site, which diminishes the energy upshift due to the antibonding interaction between the Ba 5d_{x2-y2} and As 4*p* orbitals and also contributes to the formation of the deep CBM. This is similar to the case of superdegeneration observed *e.g.* in cubic perovskites; for example, the band gaps of GeO_2 are >6 eV, but that in cubic $SrGeO_3$ is reduced to 2.7 eV due to the

non-bonding nature of Ge 4*s* [36].

In contrast, LaZnAsO has a lower ligand symmetry of C_{4v} around La (see Figure 3.6b), and each La 5*d* orbital cannot avoid hybridization with O 2*p* and As 4*p* orbitals, where antibonding interaction raises the CBM. The energy spilt of La 5*d* orbitals is much narrower, as seen from the *lm*-decomposed DOSs in the rightmost panel of Figure 3.3b and the derived schematic energy diagram in Figure 3.6d. Besides, the energy levels of La 5*d* orbitals are also up-shifted significantly and are higher than the Zn 4*s* level due to the antibonding interaction between the La 5*d* and the O2*p* and As 4*p* orbitals. As a result, La 5*d* orbitals do not contribute to the CBM structure, and the band gap is mainly formed in the [ZnAs] layer. From the above discussion, it is concluded that the non-bonding Ba $5d_{x2-y2}$ orbital forms the deep CBM and contributes to the narrow band gap of β-$BaZn_2As_2$.

3.4 Conclusions

The HSE06 calculations, which reproduce the experimental band gap values and the VB structures of β-$BaZn_2As_2$ and LaZnAsO, revealed that the extremely narrow band gap in β-$BaZn_2As_2$ originates from two reasons; one is the pushed-up VBM which is primarily composed of antibonding states of As $4p_z$ orbitals in the adjacent layers, and the other is the extremely low-lying energy level of the non-bonding Ba $5d_{x2-y2}$ orbitals, which is lower even than Zn 4*s* states. It is believed that the present results provide a clue to better understanding of the evolution of band structure and flexible control of band gap and carrier transport in versatile pnictide compounds.

References

[1] K. Ueda, S. Inoue, S. Hirose, H. Kawazoe, and H. Hosono, Appl. Phys. Lett. **77**, 2701 (2000).

[2] H. Hiramatsu, K. Ueda, H. Ohta, M. Hirano, T. Kamiya, and H. Hosono, Appl. Phys. Lett. **82**, 1048 (2003).

[3] K. Kayamura, H. Hiramatsu, M. Hirano, R. Kawamura, H. Yanagi, T. Kamiya, and H. Hosono, Phys. Rev. B **76**, 195325 (2007).

[4] K. Kayamura, R. Kawamura, H. Hiramatsu, H. Yanagi, M. Hirano, T. Kamiya, and H. Hosono, Thin Solid Films **516**, 5800 (2008).

[5] K. Kayanuma, H. Hiramatsu, T. Kamiya, M. Hirano, and H. Hosono, J. Appl. Phys. **105**, 073903 (2009).

[6] Y. Kamihara, H. Hiramatsu, M. Hirano, R. Kawamura, H. Yanagi, T. Kamiya, and H. Hosono, J. Am. Chem. Soc. **128**, 10012 (2006).

[7] Y. Kamihara, T. Watanabe, M. Hirano, and H. Hosono, J. Am. Chem. Soc. **130**, 3296 (2008).

[8] T. Watanabe, H. Yanagi, Y. Kamihara, T. Kamiya, M. Hirano, and H. Hosono, J. Solid State Chem. **181**, 2117 (2008).

[9] M. Rotter, M. Tegel, and D. Johrendt, Phys. Rev. Lett. **101**, 107006 (2008).

[10] T. Katase, H. Hiramatsu, H. Yanagi, T. Kamiya, M. Hirano, and H. Hosono, Solid State Commun. **149**, 2121 (2009).

[11] E. D. Bauer, F. Ronning, B. L. Scott, and J. D. Thompson, Phys. Rev. B **78**, 172504 (2008).

[12] D. J. Singh, A. S. Sefat, M. A. McGuire, B. C. Sales, and D. Mandrus, Phys. Rev. B **79**, 094429 (2009).

[13] A. S. Sefat, D. J. Singh, R. Jin, M. A. McGuire, B. C. Sales, and D. Mandrus, Phys. Rev. B **79**, 024512(2009).

[14] V. K. Anand, P. K. Perera, A. Pandey, R. J. Goetsch, A. Kreyssig, and D. C. Johnston,

Phys. Rev. B **85**, 214523 (2012).

[15] S. L. Brock, J. E. Greedan, and S. M. Kauzlarich, J. Solid State Chem. **113**, 303 (1994).

[16] Y. Singh, A. Ellern, and D. C. Johnston, Phys. Rev. B **79**, 094519 (2009).

[17] H. F. Wang, K. F. Cai, H. Li, L. Wang, and C. W. Zhou, J. Alloys Compd. **477**, 519 (2009).

[18] J. An, A. S. Sefat, D. J. Singh, and M. -H. Du, Phys. Rev. B **79**, 075120 (2009).

[19] K. Zhao, Z. Deng, X. C. Wang, W. Han, J. L. Zhu, X. Li, Q. Q. Liu, R. C. Yu, T. Goko, B. Frandsen, L. Liu, F. Ning, Y. J. Uemura, H. Dabkowska, G. M. Luke, H. Luetkens, E. Morenzoni, S. R. Dunsiger, A. Senyshyn, P. Böni, and C. Q. Jin, Nat. Commun. **4**, 1442 (2013).

[20] G. Just and P. J. Paufler, Alloys Compd. **232**, 1 (1996).

[21] P. Klüfers and A. Mewis, Z. Naturforsch. **33b**, 151 (1978).

[22] A. Hellmann, A. Löhken, A. Wurth, and A. Mewis, Z. Naturforsch. **62b**, 155 (2007).

[23] S. Kawasaki, T. Tabuchi, X. F. Wang, X. H. Chen, and G. -Q. Zheng, Supercond. Sci. Technol. **23**, 054004 (2010).

[24] S. Jia, P. Jiramongkolchai, M. R. Suchomel, B. H. Toby, J. G. Checkelsky, N. P. Ong, and R. J. Cava, Nat. Phys. **7**, 207 (2011).

[25] Z. Xiao, F.-Y. Ran, H. Hiramatsu, S. Matsuishi, H. Hosono, and T. Kamiya, Thin Solid Films **559**, 100 (2014).

[26] J. Misiewicz and J. M. Pawlikowski, Solid State Commun. **32**, 687 (1979).

[27] A.V. Mudryi, A. I. Patuk, I. A. Shakin, A. E. Kalmykov, S. F. Marenkin, and A. M. Raukhman, Mater. Chem. Phys. **44**, 151 (1996).

[28] I. R. Shein and A. L. Ivanovskii, J. Alloys Compd. **583**, 100 (2014).

[29] G. Kresse and J. Furthmüller, Phys. Rev. B **54**, 11169 (1996).

[30] J. P. Perdew, K. Burke, and M. Ernzerhof, M. Phys. Rev. Lett. **77**, 3865 (1996).

[31] J. Heyd, G. E. Scuseria, and M. Ernzerhof, J. Chem. Phys. **118**, 8207 (2003).

[32] J. Heyd, G. E. Scuseria, and M. Ernzerhof, J. Chem. Phys. **124**, 219906 (2006).

[33] H. Lincke, R. Glaum, V. Dittrich, M. H. Möller, and R. Z. Pöttgen, Anor. Allg. Chem. **635**, 936 (2009).

[34] R. Hoffmann and C. Zheng, J. Phys. Chem. **89**, 4175 (1985).

[35] R. Poble, R. Frankovsky, and D. Z. Johrendt, Naturforsch. **68b**, 581 (2013).

[36] H. Mizoguchi, T. Kamiya, S. Matsuishi, and H. Hosono, Nat. Commun. **2**, 470 (2011).

Table 3.1. Experimental and calculated band gaps (E_g) and structural parameters of β-$BaZn_2As_2$ and LaZnAsO. "Exp." indicates literature values, and "LDA", "PBE96" and "HSE06" are those obtained by DFT/HDFT calculations using these functionals. Δ show the deviations from the experimental values.

Compound	Method	E_g (eV)	a (Å) / Δ (%)	c (Å) / Δ (%)	V (Å3) / Δ (%)
β-$BaZn_2As_2$	Exp.	0.23 [25]	4.12 [22]	13.578 [22]	230.49 [22]
	LDA	< 0	4.043 / −1.9	13.205 / −2.7	215.89 / −6.3
	PBE96	< 0	4.168 / +1.2	13.630 / +0.4	236.75 / +2.7
	HSE06	0.23	4.151 / +0.7	13.616 / +0.3	234.64 / +1.8
LaZnAsO	Exp.	1.50 [4]	4.0956 [33]	9.07 [33]	152.13 [33]
	LDA	0.36	4.018 / −1.9	8.828 / −2.7	142.53 / −6.3
	PBE96	0.56	4.113 / +0.4	9.126 / +0.7	154.38 / +1.4
	HSE06	1.38	4.098 / +0.0	9.099 / +0.4	152.78 / +0.4

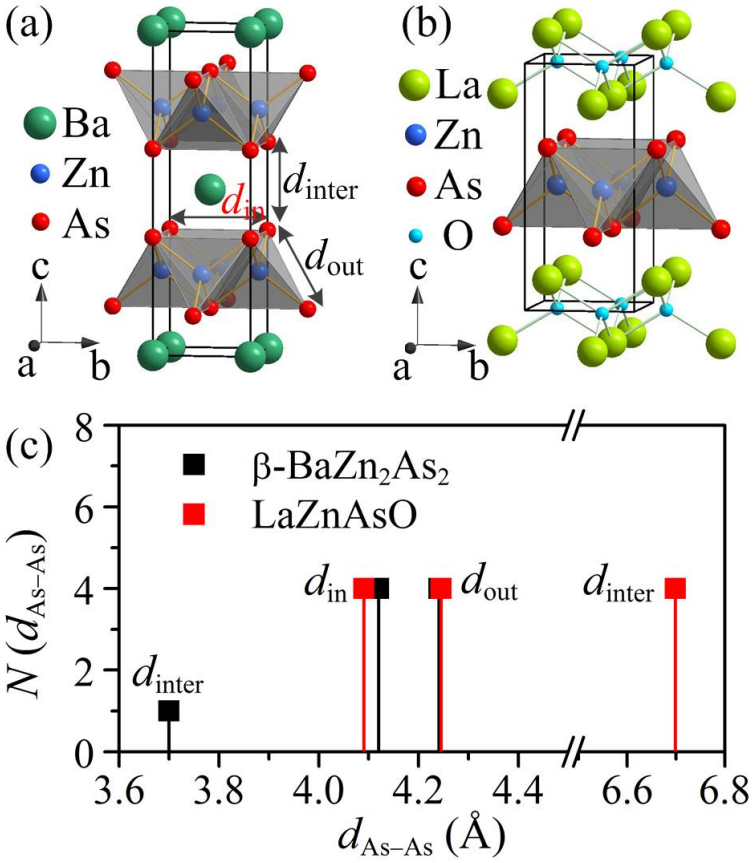

Figure 3.1. Crystal structures. Schematic illustrations for (a) β-$BaZn_2As_2$ (*I*4/*mmm*) and (b) LaZnAsO (*P*4/*nmm*). The d_{in} (equal to the lattice parameter *a*), d_{out} and d_{inter} parameters are defined as the distances between the nearest As neighbors along the in-plane, the out-of-plane and the interlayer directions, respectively, as denoted in (a). (c) Comparison of coordination structures among β-$BaZn_2As_2$, LaZnAsO, and tri-$BaZn_2As_2$, which plots the coordination number distribution of As atoms around an As atom as a function of As–As distance (d_{As-As}). Reprinted with permission from *J. Am. Chem. Soc.* 2014, 136, 14959−14965. Copyright 2014 American Chemical Society.

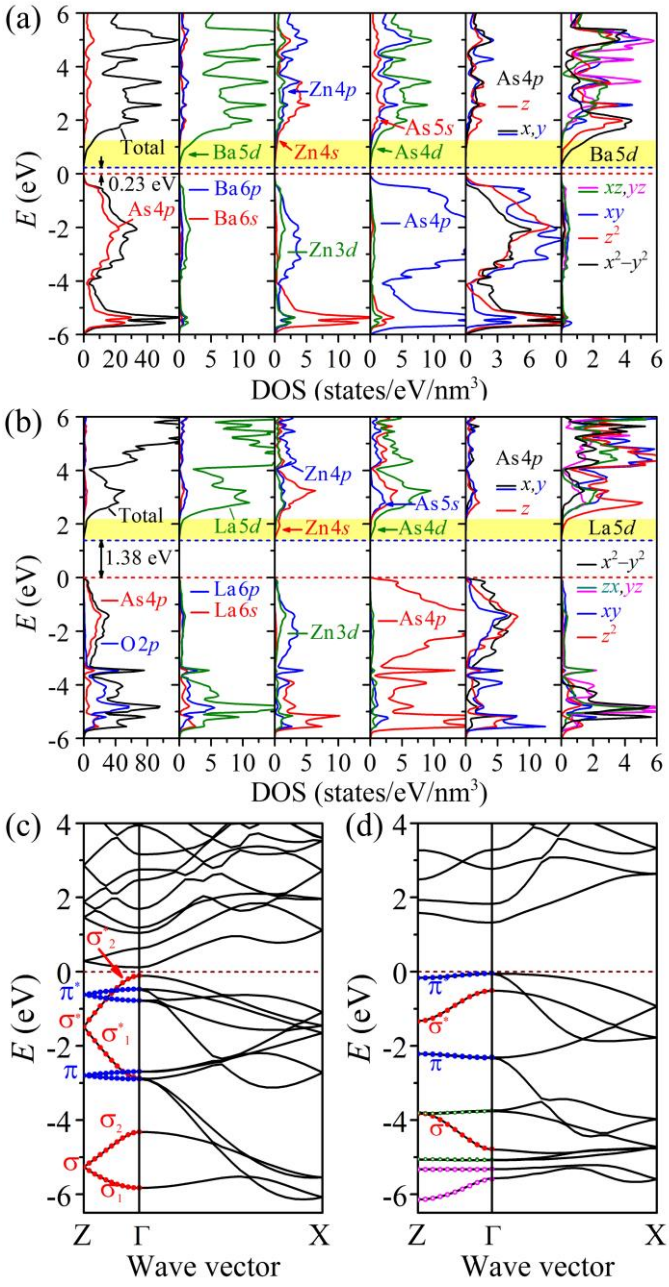

Figure 3.2. (a and b) Total, projected, and *lm*-decomposed densities of states (DOS) of (a) β-$BaZn_2As_2$ and (b) LaZnAsO. The red and blue lines mark the valence band maximum (VBM) and the conduction band minimum (CBM), respectively. (c and d) Band structures of (c) β-$BaZn_2As_2$ and (d) LaZnAsO. The dashed lines mark the VBMs. Reprinted with permission from *J. Am. Chem. Soc.* 2014, 136, 14959−14965. Copyright 2014 American Chemical Society.

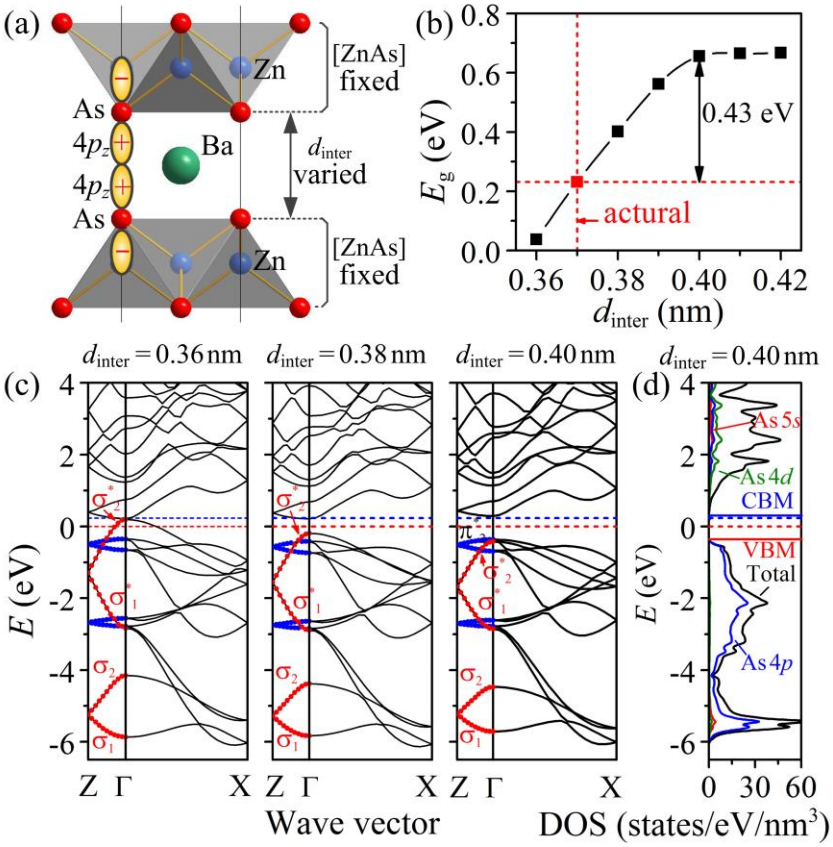

Figure 3.3. (a) Schematic illustration of hypothetical structures of β-$BaZn_2As_2$ with fixed [ZnAs] layer structures and varied d_{inter} values. (b) Calculated band gap of β-$BaZn_2As_2$ as a function of d_{inter}. (c) Band structures of hypothetical β-$BaZn_2As_2$ structures with d_{inter} being 0.36, 0.38 and 0.40 nm. (d) Total and projected DOSs of hypothetical β-$BaZn_2As_2$ with d_{inter} = 0.40 nm. In (c) and (d), the energies are aligned to the energy levels of the Zn 3*d* orbitals, and the dashed red and blue lines mark the VBM and the CBM of the experimental β-$BaZn_2As_2$ structure (d_{inter} = 0.37 nm) for comparison. Reprinted with permission from *J. Am. Chem. Soc.* 2014, 136, 14959−14965. Copyright 2014 American Chemical Society.

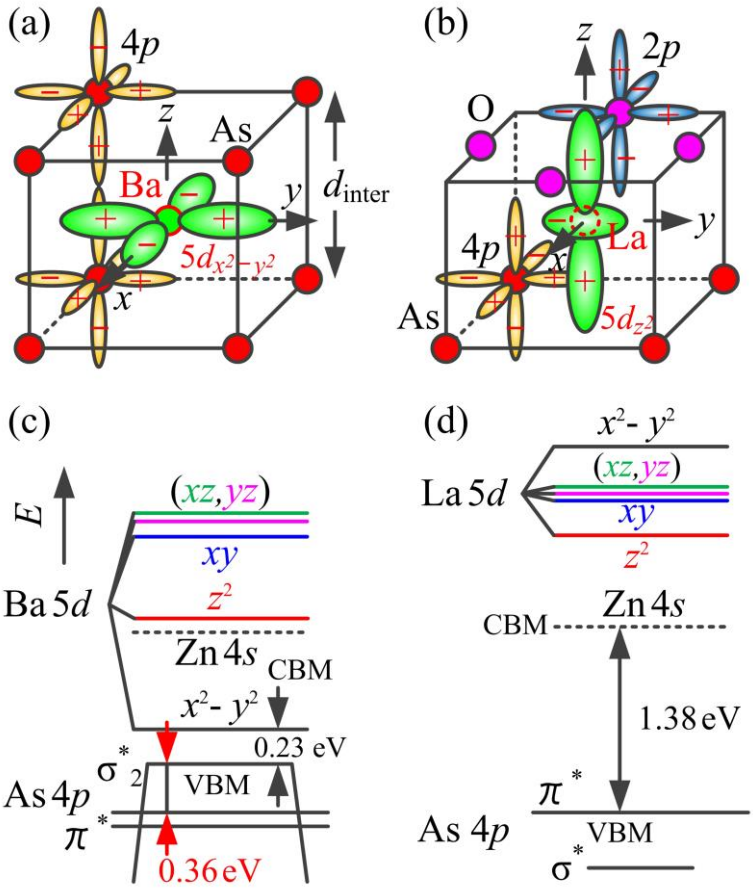

Figure 3.4. (a,b) Ligand geometries of (a) D_{4h} around Ba in β-$BaZn_2As_2$ and (b) C_{4v} around La in LaZnAsO. The wave functions of the As 4*p* orbitals, the O 2*p* orbitals and the lowest 5*d* orbitals of Ba and La are also shown schematically. (c,d) Schematic energy diagrams near the VBM and the CBM for (c) β-$BaZn_2As_2$ and (d) LaZnAsO. The energy levels are derived from the *lm*-decomposed DOSs in Figs. 3(a,b) and aligned by Zn 3*d* levels. Reprinted with permission from *J. Am. Chem. Soc.* 2014, 136, 14959−14965. Copyright 2014 American Chemical Society.

Chapter 4

Origins of Doping Asymmetry in SnS

4.1 Introduction

Control of carrier polarity conversion in semiconductor is important to produce high-performance semiconductor devices such as solar cells and light emitters, and is actually utilized in conventional semiconductors such as Si and compound semiconductors. On the other hand, it is known that such bipolar doping is not attained easily in other semiconductors; e.g., most of oxide semiconductors are of naturally *n*-type, and it is difficult to obtain *p*-type conduction in the same materials as known e.g. for SnO_2, and vice versa e.g. for Cu_2O and NiO. To date, several, but a limited number of doping routes have been recognized and employed. For ionic semiconductors, aliovalent ion substitution and off-chemical stoichiometry are known well; e.g., substitution of Zn^{2+} with Ga^{3+} increased the electron density in ZnO [1], and Cu vacancy increased the hole density in Cu_2O [2]. Further, H doping is now recognized as an important and effective route for *n*-type doping in oxide semiconductors [3]. For organic semiconductors and devices, chemical doping, which is caused by partial charge transfer originating from different electron affinities of constituent atoms / functional groups, is important [4]. The most popular route for carrier polarity conversion is aliovalent ion substitution; actually, *n*-type conversion of SnO was realized by substituting Sb^{3+} ions for the Sn^{2+} ions [5]. However, up to now, this route has not been succeeded in many semiconductors, such as SnS.

SnS is a naturally *p*-type semiconductor with hole densities of 10^{15}–10^{18} cm^{-3} and the high mobilities ~90 $cm^2/(Vs)$ [6,7]. It has a layered crystal structure along the *a*-axis direction as shown in Fig. 1a, which belongs to the orthorhombic lattice (the space group *Pnma*, No. 62). Due to its reasonable small bandgap of ~1.07 eV [8] and strong optical absorption coefficients above the bandgap (> 10^5 cm^{-1}), SnS is expected to be a promising absorber material for low-cost thin-film solar cells. Thus, numerous *n*-type materials, including CdS [9,10], SnS_2 [11], FeS_2 [12], TiO_2 [13], ZnO [14], and amorphous Si [15], have been employed for fabricating heterojunction SnS-based solar cells. However, the highest energy conversion efficiency reported up to now is limited to ~3.88% [16,17], which is much lower than the theoretically-predicted value of 24% [18]. The low efficiency might suffer from unfavorable band alignments and the large lattice mismatches in the heterojunction structures [19,20]. Fabricating a homojunction solar cell with *p*-SnS/*n*-SnS structure would solve this problem.

With this line, much effort has been devoted to obtaining *n*-type SnS materials by substituting the Sn^{2+} ions with aliovalent ions with the charge state of 3+. Dussan *et al*. report that Bi^{3+}-doped SnS exhibits *n*-type conduction when the Bi concentration is larger than 50% [21]. Whereas, a Bi_2S_3 impurity phase, which is also *n*-type, was observed in their heavily Bi-doped SnS films [22]. Sajeesheesh *et al*. claim that *n*-type SnS thin films are obtained by chemical spray pyrolysis, but their result might be due to a significant *n*-type Sn_2S_3 impurity phase in the films [23]. Very recently, Sinsermsuksakul *et al*. tried to obtain *n*-type SnS by Sb^{3+} doping; however, except for great increase in the electrical resistance of the SnS film, no *n*-type conduction was observed [24]. To date, no reliable *n*-type SnS material has yet been reported. That is, SnS suffers the doping asymmetry problem; i.e., it can be naturaly doped *p*-type, but hardly *n*-type, which hinders the

fabrication of *p*-SnS/*n*-SnS homojunction for high-performance solar cells.

In this chapter, the defect physics of SnS was investigated by defect calculatons based on density functional theory (DFT). Particularly, the origins of the doping asymmetry in SnS were discussed based on the DFT calculation results and the band alignment diagram. Further, aliovalent Sb^{3+} and Bi^{3+} doping in SnS was also theoretically assessed.

4.2 Computational Details

The electronic structure and defect calculations were performed for SnS in the framework of DFT using the projector augmented plane-wave method as implemented in the VASP code [25]. The local density approximation (LDA) was used for the exchange-correlation functional, as employed in Ref. [26]. The plane-wave cut-off energy was set to 323.3 eV. A 72-atom supercell and a 3×3×3 Monkhorst-Pack *k*-mesh were used. Prior to the electronic and the total energy calculations, internal ion coordinate parameters were optimized so as to take the minimum total energy but the supercell parameters were fixed (the fixed-cell structural relaxations) so as to meet the dilute limit condition [27]; that is, the lattice parameters were constrained to the experimental values (i.e., a = 11.18 Å, b = 3.982 Å, c = 4.329 Å [28]). It is known that the total energies for defect-containing models, in particular for charged defects, are affected by considerable finite-size effects [29]. Therefore, the common posteriori corrections to the calculated total energies were applied by the methodology in the literatures [29,30].

The formation enthalpy ($\Delta H_{D,q}$) of a defect (D) in a charge state q is calculated through the equation [27]

$$\Delta H_{D,q}(E_F,\mu) = E_{D,q} - E_H - \Sigma n_\alpha \mu_\alpha + q(E_F+E_V+\Delta V), \quad (4.1)$$

where $E_{D,q}$ and E_H are the total energies of a supercell with a defect in the charge state q

and a perfect host supercell, respectively. n_α indicates the number of α atoms added to ($n_\alpha > 0$) or removed from ($n_\alpha < 0$) the defect supercell model, and μ_α is the chemical potential of an α atom with respect to that of an elemental phase (μ_α^{el}) given by $\mu_\alpha = \mu_\alpha^{el} + \Delta\mu_\alpha$. E_F is the Fermi level relative to the valence band maximum (VBM, E_V) which is corrected by the ΔV method [27]. μ_α varies depending on the experimental condition during growth or annealing where the defect states are frozen and ranges from the S-rich (Sn-poor) to the S-poor (Sn-rich) conditions. $\Delta\mu_\alpha$ should satisfy the thermal equilibrium stability conditions; i.e., $\Delta\mu_{Sn} + \Delta\mu_S = \Delta H(SnS)$. The S-rich conditions are given by the equilibrium conditions between SnS and Sn_2S_3; while the S-poor limit is taken with respect to elementary β-Sn (i.e. $\Delta\mu_{Sn} = 0$).

The defect concentrations $c_{D,q}$ are calculated by the statistic equation [27]

$$c_{D,q}(E_F,\mu,T_D) = N_{D,q}\exp[\Delta S_{D,q}/k_B - \Delta H_{D,q}(E_F,\mu)/k_B T_D], \quad (4.2)$$

where $N_{D,q}$ is the concentration of the possible sites where the defects can be formed, $\Delta S_{D,q}$ the formation entropy, k_B the Boltzmann constant, and T_D the growth or annealing temperature (i.e., the defects formed at T_D were assumed to be frozen to room temperature). It is difficult to determine $\Delta S_{D,q}$ by DFT; therefore a typical value of $5k_B$ [31] was used for defects in SnS. The equilibrium Fermi level ($E_{F,e}$), $c_{D,q}$ and the net carrier concentration for given μ and T_D were determined so as to satisfy the charge neutrality condition [31].

4.3 Results and Discussion

4.3.1 Properties of Intrinsic Defects in SnS

The calculated ΔH of the intrinsic defects in SnS (vacancies V_{Sn} and V_S, interstitials Sn_i and S_i, and antisites Sn_S and S_{Sn}) are shown in Figs. 5.2a and 5.2b for the S-rich and S-poor conditions, respectively. Under both conditions, V_{Sn} has the lowest ΔH with a shallow

$\varepsilon(0/2-)$ transition at 0.03 eV above the VBM, which is close to the experimental observation (0.22 eV) [32] and mainly responsible for the *p*-type conduction in SnS. This result substantiates the established experimental observations theoretically [33,34]. Under the S-poor condition, Sn_S has a low ΔH comparable to that of V_{Sn}, and but acts as a deep acceptor because it is ionized to negative only in the high E_F region $\geq$ 0.36 eV. V_S and Sn_i have $\varepsilon(n+/0)$ transition levels closer to the VBM than to the conduction band minimum (CBM, $E_C = E_V + E_g$, where E_g is the band gap 1.08 eV); i.e, they work as donors but the $\varepsilon(n+/0)$ levels are far below the CBM and cannot be *n*-type sources. S_{Sn} and S_i have too large ΔH to affect the electrical properties. These results are consistent with those reported in Ref. 26.

Figures 4.2c and 4.2d show the calculated c_D of the dominant defects at T = 673.15 K (the deposition temperature in Ref. 8) under the S-rich and S-poor conditions, respectively. In the S-rich condition, $E_{F,e}$ was calculated to be 0.07 eV from the VBM by the charge neutrality condition. At $E_{F,e}$, the acceptor V_{Sn}^{2-} are generated at the high c_D of 1.4×10^{18} cm^{-3}, but compensated slighty by the generation of the donor V_S^{2+} (2.0×10^{15} cm^{-3}) and S_{Sn}^{+} (2.4×10^{11} cm^{-3}), thus yielding the net hole concentration (p) of 2.7×10^{18} cm^{-3}. Under the S-poor condition, $E_{F,e}$ is increased to 0.41 eV from the VBM. The holes produced by V_{Sn}^{2-} ($2\times3.9\times10^{15}$ cm^{-3}) and Sn_S^{-} (5.2×10^{15} cm^{-3}) are partially compensated by the electrons produced by V_S^{2+} ($2\times2.0\times10^{15}$ cm^{-3}), resulting in the lowered p of 7.6×10^{15} cm^{-3}. These results are in good agreement with our previous experimental results in epitaxial SnS films [8]; i.e., p ranged from 4.0×10^{15} to 2.2×10^{17} cm^{-3}, as well as the theoretical results by Vidal *et al* [26].

4.3.2 Origins of Doping Asymmetry in SnS

Since no intrinsic defect can be an effective *n*-type source as shown above, it is unlikely to

abtain intrinsic *n*-type doping in pure SnS undeer all growth conditions (i.e. from the S-rich to the S-poor). Further, the extrinsic dopability also can be perceived from the results shown in Fig. 4.1. Under S-rich condition, V_{Sn}^{2-} has negative ΔH at *n*-type conditions (i.e., $E_F > E_g/2$) and will form spontaneously and accept the electrons released by *n*-type dopants. Therefore, *n*-type doping is impossilbe under S-rich condition. On the other hand, under S-poor condition, V_{Sn}^{2-} has positive but very small ΔH at some *n*-type conditions. Therefore, *n*-type doping is possible but would be difficult because the compensating V_{Sn}^{2-} also form heavily. These results sustantiate the doping asymmetry in SnS, i.e., it is readily doped *p*-type, but not *n*-type.

The origins of doping asymmetry in SnS can also be understood qualitatively based on the band alignment diagram shown in Fig. 4.2a. It is known that Si has moderate ionization potential (*IP*) of 5.17 eV and moderate electron affinity (*EA*) of 4.05 eV [35]; therefore, can be readily doped iether *p*-type by B dopant or *n*-type by P dopant. PbS, which is of the rocksalt structure, has a smaller *IP* (4.95 eV) and a larger *EA* (4.54 eV) than Si [36], and exhibit iether *p*-type conduction or *n*-type conduction without extrinsic doping. For SnS, the *IP* and *EA* were determined to be 4.68 and 3.60 eV, respectively, from the UPS spectra of an SnS film shown in Fig. 4.2b (i.e. a work function of 4.20 eV and an E_F of 0.48 eV) and the band gap of 1.08 eV [8]. The *IP* of SnS is much smaller than Si and PbS, indicating the holes generated are more energitically stable. As a result, SnS intrinsically exhibit *p*-type conduction. On the other hand, SnS has too small *EA*, the electrons doped are energitically unstable, causing the *n*-type doping difficulty.

The origins of small *IP* and *EA* values in SnS can be explained by the formation of the VBM and CBM structure. For most metal sulfide semiconductors such as SnS_2, the VBM is mainly composed of S 3*p* orbitals while the CBM is mainly composed of *s* orbtials of

metal cation. For SnS (see the bottom of Fig. 4.2c), the Sn 5*s* orbitals are fully occupied and have shallow energy levels close to the S 3*p* orbitals; therefore, they couple with each other and form bonding states at 5−8 eV and antibonding states at 10.5−12.5 eV (note that the energy is referred to the S 3*s* levels). The VBM of SnS is composed of the S 3*p*−Sn 5*s* antibonding states. It should be noted that the VBM of SnS is pushed up by the strong coupling between S 3*p* and Sn 5*s*, and higher than the typical sulfide semiconductors. On the other hand, the CBM of SnS is mainly composed of Sn 5*p*−S 3*p* antibonding states. Similarly, the Sn 5*p*−S 3*p* coupling pushes up the CBM to a shallow energy level. Therefore, it is concluded that the shallowness of the VBM and the CBM are caused by the strong *s*−*p* and *p*−*p* couplings between Sn^{2+} cation and S^{2-} anion.

In contrast, PbS has much deeper VBM and CBM than SnS (see Fig. 4.2a), though they are family compounds. The difference would originate from the different crytal structues and/or different metal cations, where the latter is of more interst for materials design. Therefore, herein, a hypothetical orth-PbS (*Pnma*, the same as SnS), rather than the real cubic one (rocksalt structure), is comparaed. The calculated electronic structure of orth-PbS is shown in the top of Fig. 4.2c. As it can be clearly seen, Pb 6*s* orbitals are much deeper than Sn 5*s* orbitals, which may be attributed to the relativistic effect in the heavy metal [37]. As a result, the *sp* coupling in orth-PbS is much weaker than that in SnS. As a result, the VBM of orth-PbS is 0.53 eV deeper than that of SnS. Similarly, the CBM of orth-PbS is 0.45 eV deeper than that of SnS, which is explained by the deeper energy levels of Pb 6*p* orbitals than Sn 5*p* orbitals also due to the relativistic effect [37]. One may expect that *n*-type doping would be easier in orth-PbS if it really exists and that the serious doping asymmetry problme in SnS would be improved if Pb is incorporated in the SnS lattice. The effects of Pb substitution in SnS will be discussed in the following Chapter 5.

4.3.3 Assessment of Sb^{3+} and Bi^{3+} Doping in SnS

Aliovalent ion doping by Sb^{3+} and Bi^{3+} into the Sn^{2+} sites, which are expected to release electrons for *n*-type conductivity [21,24], but has not been effective. Here, the Sb and Bi doping effects are theoretically assessed by defect calculations. Three possible doping sites, i.e. the Sn substitutional sites (Sb_{Sn} and Bi_{Sn}), the antisites on S (Sb_S and Bi_S), and the interstitial sites (Sb_i and Bi_i) were examined. The calculated ΔH are shown in Figs. 5.3a and 5.3b. The Sb and Bi dopants can hardly be incorporated to the interstitial sites because of the prohibitively high ΔH values (> 2 eV) of Sb_i and Bi_i. Under the S-rich condition, the Sb_{Sn} and Bi_{Sn} have lower ΔH than the Sb_S and Bi_S and are energetically favored. The Sb_{Sn} and Bi_{Sn} have the $\varepsilon(+/0)$ transition levels at 0.74 and 0.71 eV, respectively, and would work as deep donors. However, V_{Sn}^{2-} has lower ΔH in the E_F region closer to the CBM, indicating that the holes produced by V_{Sn}^{2-} are not compensated completely by the electrons generated from Sb_{Sn} and Bi_{Sn}. As a result, the resulting p is decreased by 1–2 orders of magnitude with increasing the dopant content (the blue lines in Figs. 5.3c and 5.3d, which explains the observed result that the resistivity increased by 2 orders of magnitude in the Sb-doped SnS thin films by Sinsermsuksakul *et al.* [24].

On the other hand, the S-poor condition is favored to suppress the formation of V_{Sn} acceptors. However, under the S-poor condition, Sb and Bi prefer to take the Sn sites at low E_F (acting as donors) as expected but unexpectedly the S sites at high E_F (acting as acceptors). The resulting $E_{F,e}$ are pinned at 0.43 and 0.48 eV from the VBM for the cases of Sb and Sb dopants, respectively. The resulting p is almost independent of the dopant content as seen in the red lines in Figs. 5.3c and 5.3d.

From these results, it would be unlikely to achieve *n*-type conductivity in SnS by aliovalent doping using the Sb and Bi dopants. On the other hand, Dussan *et al.* [21]

claimed that *n*-type conduction was obtained in SnS by Bi substitution. However, *n*-type SnS_2 and Bi_2S_3 impurity phases were detected in their films, which would be a possible origin of the observed *n*-type conductivity.

4.4 Conclusions

Defect formation and doping mechanism were studied for SnS by DFT. The native *p*-type conduction in SnS is originated mainly from Sn vacancies. It is difficult to dope SnS *n*-type because the shallow acceptor Sn vacancy forms readily and largely at *n*-type conditions, which compensente *n*-type doping sources. The origins of the doping asymmetry in SnS is explained by its too shallow VBM and CBM levels, i.e., too small ionization potential and electron affinity, which are caused by the strong *s*–*p* and *p*–*p* couplings between Sn^{2+} cation and S^{2-} anion, respectively. Further, Sb and Bi doping in SnS was assessed and found not effective to attain *n*-type conduction in SnS.

References

[1] H. J. Ko, Y. F. Chen, S. K. Hong, H. Wenisch, T. Yao and D. C. Look, Appl. Phys. Lett. **77**, 3761 (2000).

[2] H. Raebiger, S. Lany, and A. Zunger, Phys. Rev. B **76**, 045209 (2007).

[3] L.-Y. Chen, W.-H. Chen, J.-J. Wang, F. C.-N. Hong and Y.-K. Su, Appl. Phys. Lett. **85**, 5628 (2004).

[4] H. Méndez, G. Heimel, A. Opitz, K. Sauer, P. Barkowski, M. Oehzelt, J. Soeda, T. Okamoto, J. Takeya, J.-B. Arlin, J.-Y. Balandier, Y. Geerts, N. Koch, and I. Salzmann, Angew. Chem. Int. Edit. **52**, 7751 (2013).

[5] H. Hosono, Y. Ogo, H. Yanagi, and T. Kamiya, Solid-State Lett. **14**, H13 (2011).

[6] W. Albers, C. Haas, and F. van der Maesen, Phys, Chem. Solids **15**, 306 (1960).

[7] N. R. Mathews, H. B. M. Anaya, M. A. Cortes-Jacome, C. Angeles-Chavez, and J. A. Toledo-Antonio, J. Electrochem. Soc. **157**, H337 (2010).

[8] F.-Y. Ran, Z. Xiao, H. Hiramatsu, H. Hosono, and T. Kamiya, Appl. Phys. Lett. **104**, 072106 (2014).

[9] K. T. Ramakrishna Reddy, N. Koteswara Reddy, and R. W. Miles, Sol. Energy Mater. Sol. Cells **90**, 3041 (2006).

[10] S. A. Bashkirov, V. F. Gremenok, V. A. Ivanov, V. V. Lazenka, and K. Bente, Thin Solid Films **520**, 5807 (2012).

[11] A. Sánchez-Juárez, A. Tiburcio-Silver, and A. Ortiz, Thin Solid Films **480**, 452 (2005).

[12] N. Berry, M. Cheng, C. L. Perkins, M. Limpinsel, J. C. Hemminger, and M. Law, Adv. Energy Mater. **2**, 1124 (2012).

[13] Y. Wang, H. Gong, B. H. Fan, and G. X. Hu, J. Phys. Chem. C **114**, 3256 (2010).

[14] M. Ichimura and H. Takagi, Jpn. J. Appl. Phys. **47**, 7845 (2008).

[15] F. Jiang, H. L. Shen, W. Wang, and L. Zhang, J. Electrochem. Soc. **159**, H235 (2012).

[16] P. Sinsermsuksakul, K. Hartman, S. B. Kim, J. Heo, L. Sun, H. H. Park, R. Chakraborty, T. Buonassisi, and R. G. Gordon, Appl. Phys. Lett. **102**, 053901 (2013).

[17] V. Steinmann, R. Jaramillo, K. Hartman, R. Chakraborty, R. E. Brandt, J. R. Poindexter, Y. S. Lee, L. Sun, A. Polizzotti, H. H. Park, R. G. Gordon, and T. Buonassisi, Adv. Mater. **26**, 7488 (2014).

[18] A. Schneikart, H.-J. Schimper, A. Klein, and W. Jaegermann, J. Phys. D. Appl. Phys. **46**, 305109 (2013).

[19] L. Sun, R. Haight, P. Sinsermsuksakul, S. Bok Kim, H. H. Park, and R. G. Gordon, Appl. Phys. Lett. **103**, 181904 (2013).

[20] X. Cai, S. Zeng, and B. Zhang, Appl. Phys. Lett. **95**, 173504 (2009).

[21] A. Dussan, F. Mesa, and G. Gordillo, J. Mater. Sci. **45**, 2403 (2010).

[22] G. Gordillo, M. Botero, and J. S. Oyola, Microelectron. J. **39**, 1351 (2008).

[23] T. H. Sajeesh, A. R. Warrier, C. S. Kartha, and K. P. Vijayakumar, Thin Solid Films **518**, 4370 (2010).

[24] P. Sinsermsuksakul, R. Chakraborty, S. B. Kim, S. M. Heald, T. Buonassisi, and R. G. Gordon, Chem. Mater. **24**, 4556 (2012).

[25] G. Kresse and J. Furthmüller, Phys. Rev. B **54**, 11169 (1996).

[26] J. Vidal, S. Lany, M. d'Avezac, A. Zunger, A. Zakutayev, J. Francis, and J. Tate, Appl. Phys. Lett. **100**, 032104 (2012).

[27] C. G. Van De Walle and J. Neugebauer, J. Appl. Phys. **95**, 3851 (2004).

[28] S. Del Bucchia, J.-C. Jumas, and M. Maurin, Acta Crystallogr. **B37**, 1903 (1981).

[29] S. Lany and A. Zunger, Phys. Rev. B **78**, 235104 (2008).

[30] S. Lany and A. Zunger, Model. Simul. Mater. Sci. Eng. **17**, 084002 (2009).

[31] D. B. Laks, C. G. Van de Walle, G. F. Neumark, P. E. Blöchl, and S. T. Pantelides, Phys. Rev. B **45**, 10965 (1992).

[32] T. H. Sajeesh, K. B. Jinesh, M. Rao, C. S. Kartha, and K. P. Vijayakumar, Phys. Status Solidi A **209**, 1274 (2012).

[33] A. Lichanot and S. Gromb, J. Phys. Chem. Solids **32**, 1947 (1971).

[34] M. Devika, K. T. R. Reddy, N. K. Reddy, K. Ramesh, R. Ganesan, E. S. R. Gopal, and K. R. Gunasekhar, J. Appl. Phys. **100**, 023518 (2006).

[35] S. M. Sze and K. K. Ng, *Physics of Semiconductor Devices* (John Wiley & Sons, Inc., Hoboken, New Jersey, 2007).

[36] S. A. McDonald, G. Konstantatos, S. Zhang, P. W. Cyr, E. J. D. Klem, L. Levina, and E. H. Sargent, Nat. Mater. **4**, 138 (2005).

[37] P. W. Atkins, T. L. Overton, J. P. Rourke, M. T. Weller, and F. A. Armstrong, *Inorganic Chemistry*, 5th ed. (Oxford University Press, New York, 2010).

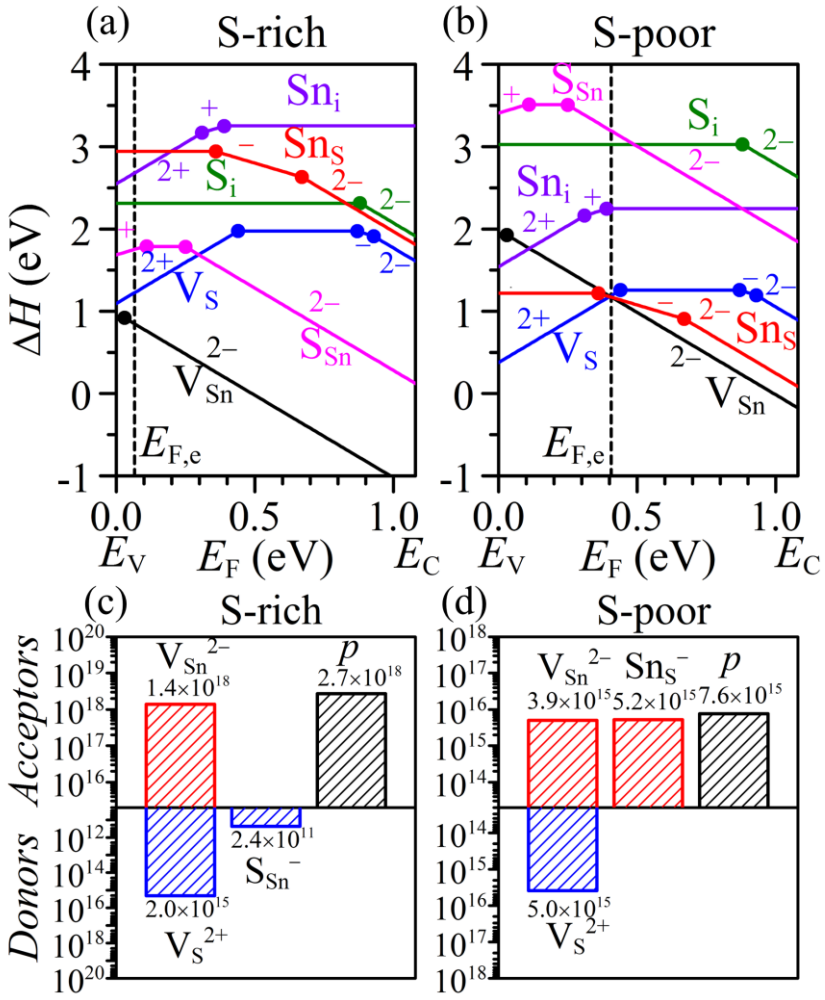

Figure 4.1. (a,b) Calculated formation enthalpies ΔH for intrinsic point defects in SnS as a function of E_F under (a) S-rich and (b) S-poor conditions. The vertical dashed lines mark the equilibrium Fermi level $E_{F,e}$ at T = 673.15 K. (c,d) Calculated defect concentrations in cm^{-3} at T = 673.15 K under (c) S-rich and (d) S-poor conditions. The black hatched bars show the equilibrium net carrier concentrations in cm^{-3}.

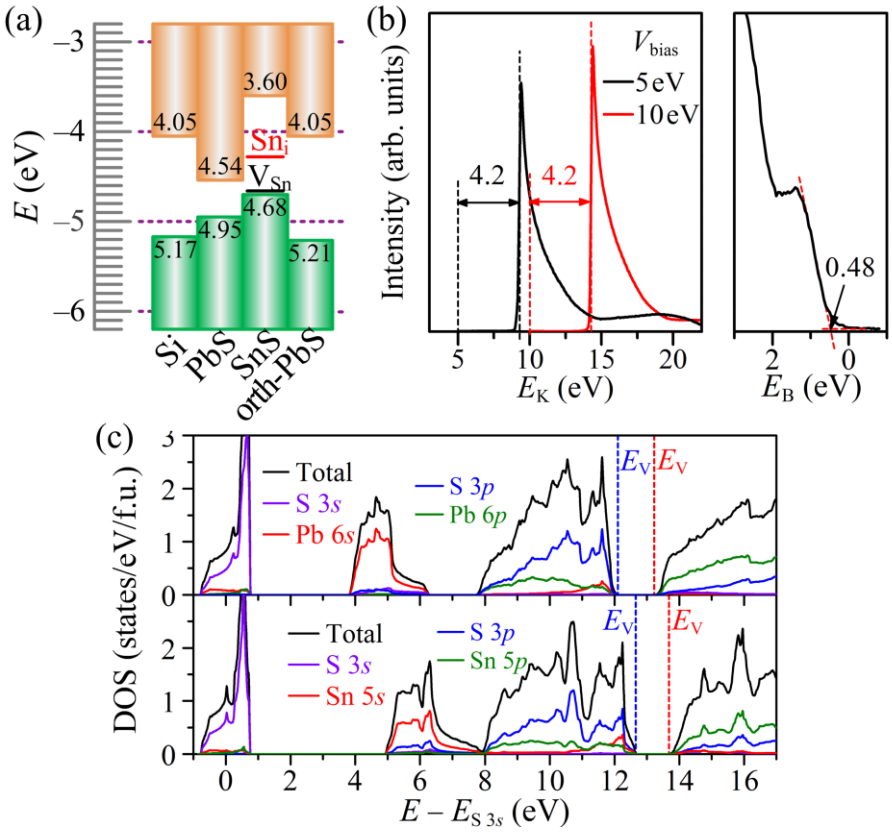

Figure 4.2. (a) Band alignment between Si [35], PbS [36], SnS and hopothetical orth-PbS (space group *Pnma*, isostructural to SnS). The data of SnS and orth-PbS were obtained from USP spectra shown in (b) and DFT calculation shown in (c), respectively. (b) UPS spectra of an epitaxial SnS film [8]. (c) Total and projected densities of states (DOSs) of SnS (bottom panel) and orth-PbS. The energies are aligned with referring to the Sn 3*s* orbitals.

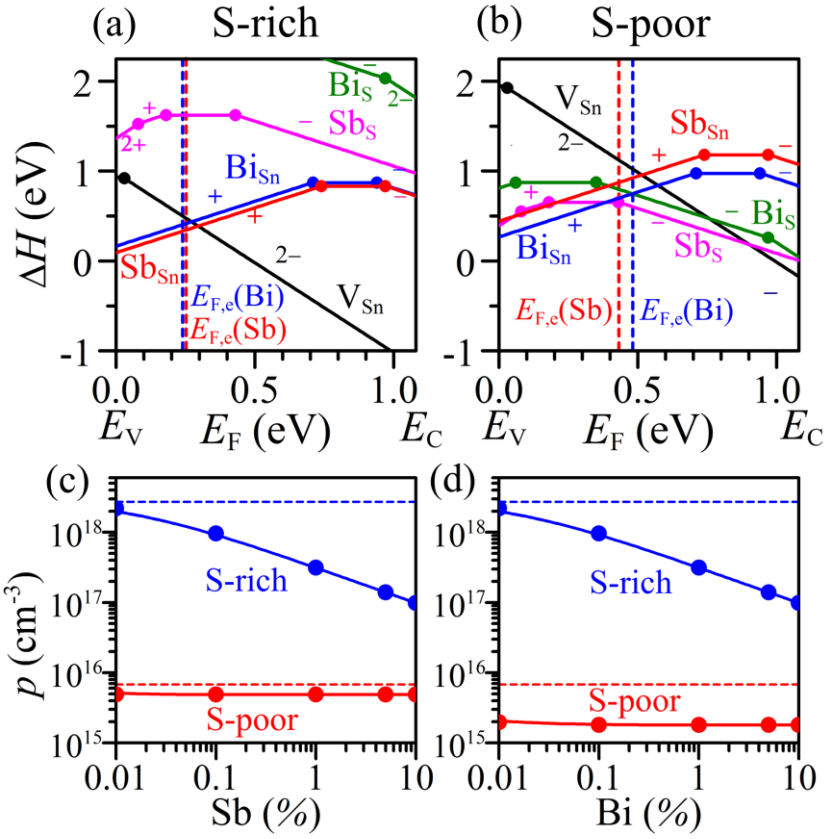

Figure 4.3. (a,b) Calculated formation enthalpies ΔH for Sb and Bi impurities in SnS as a function of E_F under (a) S-rich and (b) S-poor conditions. Also included is the dominant intrinsic defect V_{Sn} for comparison. The vertical dashed lines mark the $E_{F,e}$ at T = 673.15 K for 5% dopants. (c,d) Calculated carrier concentrations as functions of the dopant concentrations of (c) Sb and (d) Bi under S-rich (blue solid lines) and S-poor (red solid lines) conditions. The dashed lines mark the equilibrium carrier concentrations for the intrinsic defects in the undoped SnS for comparison.

Chapter 5

n-Type Conversion of SnS by Geometrical Doping Route

5.1 Introduction

In Chapter 4, the doping asymmetry in SnS are explained by the too small ionization potential (*IP*) and electron affinity (*EA*) (i.e., the shallow VBM and CBM levels) based on defect calculation and band alignment. The small *IP* makes that the holes are energetically favored and readily generated by the intrinsic defect V_{Sn} in SnS. On the other hand, the small *EA* makes the doped electrons in SnS unstable, causing the *n*-type doping difficulty in SnS. The density functional theory (DFT) calculations suggest that the shallow VBM and CBM are originated from the shallow occupied Sn 5*s* and unoccupied Sn 5*p* orbitals (see Chapter 4 for details). On the other hand, hypothetical orth-PbS has deeper VBM and CBM levels than SnS, because the Pb 6*s* and 6*p* orbitals are deeper than the Sn 5*s* and 5*p* orbitals due to the relativistic effect [1]. Based on these understandings, it is reasonable to expect that incorporating Pb into SnS lattice would deepen the VBM and CBM levels, and thus improve or even solve the doping difficulty in SnS.

In this chapter, reliable *n*-type condution was achieved in SnS films fabricated isovalent Pb^{2+} doping. It is found that the doping mechanism is strikingly different from the conventional doping routes such as ion substitution, off-stoichiometry, and chemical doping. Density functional theory calculations reveal that the Pb substitution invokes a geometrical size effect that enlarges the interlayer distance and subsequently reduces the

formation energies of Sn and Pb interstitials, which results in the electron doping.

5.2 Experimental and Computational Details

5.2.1 Fabrication and Characterization

($Sn_{1-xf}Pb_{xf}$)S films (x_f is film chemical composition) were grown on SiO_2 glass substrates by pulsed laser deposition (PLD) using a KrF excimer laser (248 nm in wavelength, 3−6 J/cm^2 of laser energy density, and 10 Hz of repetition rate) in an Ar / H_2S mixing gas flow (80 / 20 %) to control the chemical stoichiometry ([Sn]+[Pb]) : [S] (the parentheses denote the concentrations). ($Sn_{1-xt}Pb_{xt}$)S (x_f is target chemical composition) polycrystalline disks with x_t = 0.18, 0.37, and 0.66 were used as ablation targets. The base pressure of the growth chamber was 1×10^{-5} Pa, the substrate termperature (T_s) was varied from 200 to 400 ^oC, and the mixing gas pressure (P) from 5 to 20 Pa.

The crystalline phase and crystal structure of the obtained films were characterized by X-ray diffraction (XRD, radiation source = Cu Kα). Optical properties were obtained by measuring transmittance (T_r) and reflectance (R) spectra. The absorption coefficient (α) was estimated by $\alpha = \ln[(1-R)/T_r] / t$, where t is the film thickness. Electrical properties of the SnS films were analyzed by Hall effect measurements using the van der Pauw configuration with an AC modulation of magnetic field. x_f values were determined by X-ray fluorescence (XRF) spectroscopy calibrated by the chemical compositions obtained by inductively-coupled plasma-atomic emission spectroscopy (ICP-AES). The valence band structures were observed by UPS (excitation source = He I, 21.2 eV), where the films were protected in an Ar atmosphere during the transfer from the PLD chamber to the UPS chamber.

5.2.2 Theoritical Calculations

Stable crystal / defect structures, their electronic structures, and formation energies of intrinsic defects were calculated by density functional theory (DFT) calculations with local density approximation (LDA) and generalized gradient approximation (GGA) functionals using the VASP code [2]. The plane wave cutoff energy was set to 323.3 eV. A 32-atoms substitutional $(Sn_{16-n}Pb_n)S_{16}$ model (1×2×2 unit cells) model and a 4×6×5 *k*-mesh were used for the calculations of structural properties and electronic structures. The defect calculations were performed using a 64-atoms $(Sn_{16}Pb_{16})S_{32}$ model and a 3×3×3 *k*-mesh. The detailed procedures for calculating the defect formatation enthalpy (ΔH) and equilibrium Fermi level ($E_{F,e}$) are the same as described in Chapter 4.

5.3 Results and Discussion

5.3.1 Structural properties of $(Sn_{1-xf}Pb_{xf})S$ films

Figure 5.1a shows a typical out-of-plane $2\theta/\omega$ synchronous scan (top panel) and an in-plane synchronous $2\theta_\chi/\phi$ scan (bottom panel) XRD patterns of the $(Sn_{1-xf}Pb_{xf})S$ film with x_f = 0.5 grown at substrate temperature (T_s) = 300 °C and P = 5 Pa. The out-of-plane XRD pattern exhibited strong 200, 400 and 800 diffractions of the orthorhombic structure along with a weak 011 diffraction. The in-plane synchronous $2\theta_\chi/\phi$ scan (bottom panel) shows powder-like patterns with all possible *hkl* diffractions, suggesting that the film did not have in-plane orientation. These results indicate that the $(Sn_{1-xf}Pb_{xf})S$ films were polycrystalline films with a strong 100 preferential orientation normal to the substrate. No impurity phase was detected both in the out-of-plane and the in-plane XRD patterns. As seen in Figs. 5.1b and 5.1c, orthorhombic $(Sn_{1-xf}Pb_{xf})S$ films were obtained at P < 20 Pa (corresponding to the closed symbols in Fig. 5.2a); while, amorphous films were obtained

when *P* was increased to 20 Pa (the open symbols in Fig. 5.2a).

The lattice parameters of $(Sn_{1-xf}Pb_{xf})S$ films obtained from the out-of-plane 400 and the in-plane 020 and 011 diffraction angles are summarized as a function of x_f in Fig. 5.1d. As x_f increased from 0 to 0.5, the *a* and *b* values increased linearly from 1.12 to 1.14 nm and from 0.403 to 0.414 nm, respectively, whereas the *c* value decreased from 0.426 to 0.419 nm; i.e., the interlayer distance (corresponding to the *a* value) increased. The solid lines in Fig. 5.1d represent the lattice parameters of the$(Sn_{1-x}Pb_x)S$ bulk sample reported by Leute *et al.* [3]. The *a* values of the films are almost the same as those of the bulk samples. However, the *b* and *c* values exhibited non-negligible deviations from the bulk values; *i.e.*, the *b*-axis was expanded while the *c*-axis shrunken compared from the bulk values. The reason is not clear, but defects in the polycrystalline films would cause the structural difference. Figure 5.1d also compares the variation of the lattice parameters with those obtained by DFT calculations (the open symbols) performed with the $(Sn_{16-n}Pb_n)S_{16}$ supercell model (Pb substitution model). Here, both LDA and GGA functionals are compared. It can be seen that the calculated results for the Pb substitution model were within the variation of the functionals (typically, the ground-state lattice parameters by DFT include errors within 2–3%). That is, this model, where the Sn sites are substituted by Pb, explains the experimental structure well, and strongly supports that the Pb dopants are successfully incorporated to the Sn sites in the SnS lattice.

5.3.2 Electrical Properties of $(Sn_{1-xf}Pb_{xf})S$ films

Figure 5.2a shows the variation of x_f as functions of *P*, T_s and x_t. It is seen that all the x_f values were smaller than the x_t values of the corresponding targets, and the x_f values decreased with increasing *P*. As seen for the target with x_t = 0.37, the maximum x_f of Pb was incorporated when the films were grown at T_s = 300 ^{o}C, which, therefore, was

employed hereafter for discussion. The crystallized region in Fig. 5.2a is classified further to three regions based on the electrical properties. Region I is "*p*-type region" (high $P \geq 15$ Pa at low $x_f < 0.1$), where the films still exhibited *p*-type conduction with low hole densities (N_h) and low hole mobilities (μ_h) (measured by Hall effect). *n*-type $(Sn_{1-xf}Pb_{xf})S$ films were obtained in Region II ("*n*-type region", $x_f \geq 0.15$ at low $P \leq 10$ Pa). The electron density (N_e) and mobility (μ_e) changed largely with x_f and P, which will be discussed later on. Region III is the intermediate region ("highly-resistive region", low x_f & low P, and high x_f & high P), where the films exhibited very high resistivity $>10^5$ Ω·cm, and the Hall effect measurements did not give definite Hall voltage signs.

The detailed Hall effect measurement results as a function of x_f are shown in Fig. 5.2b. The pure SnS film showed *p*-type conduction with $N_h \sim 4.1\times10^{15}$ cm^{-3} and $\mu_h \sim 12$ cm^2 V^{-1} s^{-1}. The $(Sn_{1-xf}Pb_{xf})S$ film with $x_f = 0.08$ fabricated at $P = 15$ Pa still showed *p*-type conduction but with the low $N_h \sim 1.0\times10^{14}$ cm^{-3} and the very small μ_{Hall} in the order of 10^{-2} cm^2 V^{-1} s^{-1}. When $x_f \geq 0.2$, *n*-type conductions were observed for the films fabricated at P = 5 and 10 Pa. For the *n*-type $(Sn_{1-xf}Pb_{xf})S$ film with $x_f = 0.2$, N_e and μ_e were 1.4×10^{12} cm^{-3} and 1.3 cm^2 V^{-1} s^{-1}, respectively. N_e increased with increasing x_f and reached 2.0×10^{15} cm^{-3} for $x_f = 0.5$. μ_e was not changed largely when $x_f < 0.3$ ($N_e < 3.2\times10^{13}$ cm^{-3}). At x_f values > 0.4, μ_e increased almost linearly, and the maximum value of 7.0 cm^2 V^{-1} s^{-1} was obtained for $x_f = 0.5$.

Figure 5.2c shows temperature dependences of N_e and μ_e for the $(Sn_{1-xf}Pb_{xf})S$ film with the room-temperature N_e of 4.3×10^{13} cm^{-3} ($x_f = 0.48$ grown at 10 Pa). The N_e shows a thermally-activated behavior with an active energy of $E_a \sim 0.4$ eV. From a simple approximation in the impurity region $N_e = (N_D N_C)^{1/2}\exp[-(E_C - E_D)/(2k_BT)]$ (N_D is the donor density, N_C the conduction band effective density of states (DOS), $E_C - E_D$ the donor

level measured from the conduction band minimum E_C, k_B the Boltzmann constant), $E_C - E_D$ and N_D are estimated to be ~0.8 eV and 2.5×10^{21} cm^{-3} ($N_C = 2.8\times10^{21}$ cm^{-3} is taken from Si), respectively. On the other hand, although E_F was closer to E_C as in usual *n*-type semiconductors, the donor level E_D was closer to the valence band maximum energy (E_V) rather than E_C, showing that the *n*-type doping in the $(Sn_{1-xf}Pb_{xf})S$ films is a bit different from the usual *n*-type semiconductors.

As shown by the red line in Fig. 5.2c, μ_e decreased with decreasing the temperature, and the $\ln(\mu_{Hall}T^{1/2})-T^{-1}$ plot exhibited a good straight line in the whole T range, suggesting that the electron transport in the film was dominated by grain boundary (GB) potential barriers as proposed by Seto *et al.* [4], where electron transport is disturbed by potential barriers formed due to the electrons trapped at acceptor-type defects at the GBs. The GB potential barrier height E_B is estimated to be approximately 0.09 eV (the equation [4] is given in Fig. 5.2c). From this result, the potential electron mobility μ_0 (i.e., the ideal value when no GB affects the carrier transport) was estimated to be ~ 1.6×10^2 cm^2 V^{-1} s^{-1} by extrapolating E_B to zero (*i.e.*, $\mu_0 = \mu_{Hall}\exp(E_B/kT)$).

Further, *n*-type $(Sn_{0.5}Pb_{0.5})S$ / *p*-type Si pn heterojunction (see the inset of Fig. 5.2d) was prepared to confirm the *n*-type condution in $(Sn_{1-xf}Pb_{xf})S$ films. The *n*-$(Sn_{0.5}Pb_{0.5})S$ film and the *p*-Si wafer used had $N_e = 2\times10^{15}$ and $N_h = 5\times10^{15}$ cm^{-3}, respectively. The current–voltage (*I*–*V*) characteristic of the pn junction (Fig. 5.2d) shown a clear rectifying characteristic, further supporting the *n*-type conduction of the $(Sn_{1-xf}Pb_{xf})S$ films.

5.3.3 Electronic Structure and Band Alignment of $(Sn_{0.5}Pb_{0.5})S$

Figures 5.3a and 5.3b show typical optical absorption spectra and $(\alpha hv)^{1/2}$–hv plots (the indirect-transition model) of the $(Sn_{1-xf}Pb_{xf})S$ films fabricated at the various conditions, respectively. The pure SnS film (the black line in Fig. 5.3a) exhibited very weak subgap

absorption, and the bandgap estimated from $(\alpha h\nu)^{1/2}$–$h\nu$ plot is 1.08 eV. The band gaps (E_g) estimated from Fig. 5.3b are shown in Fig. 5.3c as a function of x_f, showing that the E_g increased with increasing x_f, and reached to 1.15 eV for x_f = 0.5. The calculated E_g values with LDA and GGA are also shown in Fig. 5.3c. As it can be seen, the GGA reproduces the experimental E_g values better than the LDA.

Figure 5.3d shows the valence band spectrum of the $(Sn_{0.5}Pb_{0.5})S$ film measured by UPS. The observed E_F of the $(Sn_{0.5}Pb_{0.5})S$ film was located at 0.82 eV above VBM. From the E_g of 1.15 eV, the $E_C - E_F$ value is estimated to be 0.33 eV, closer to conduction band maximum (CBM), agreeing with *n*-type conduction. Figure 5.3e shows the UPS spectra with bias voltages (V_{bias}) of 5 and 10 V. From the relative cutoff energy of the secondary electrons, the work function (W) of the $(Sn_{0.5}Pb_{0.5})S$ film was determined to be 4.20 eV. From the above results (i.e., W = 4.2 eV, E_F = 0.82 eV, and E_g = 1.15 eV), the ionization potential ($IP = W + E_F$) and electron affinity ($EA = IP - E_g$) of the $(Sn_{0.5}Pb_{0.5})S$ films were estimated to be 5.02 and 3.87 eV, respectively.

Figure 5.3f shows band alignment between Si [5], PbS [6], SnS, $(Sn_{0.5}Pb_{0.5})S$ and hypothetical orth-PbS (see details in Chapter 4). As clearly seen, $(Sn_{0.5}Pb_{0.5})S$ has moderate *IP* and *EA* values (5.02 and 3.87 eV, respectively) between those of SnS (4.68 and 3.60 eV, repectively) and those of orth-PbS (5.21 and 4.05 eV, respectively). These results indicate that incorporating Pb in SnS increased both the *IP* and the *EA*, as expected. This change can be explained by comparing the electronic structures of SnS and $(Sn_{0.5}Pb_{0.5})S$, as shown in the top and the bottom of Fig. 5.3g, respectively. As has been dicussed in Chapter 4, the shallow VBM (i.e. the small *IP*) and CBM (i.e. the small *EA*) are attributed to the strong Sn 5*s*–S 3*p* coupling and the shallow energy levels of Sn 5*p* orbitals, respectively (the top of Fig. 5.3g). As seen from the projuected DOSs of $(Sn_{0.5}Pb_{0.5})S$ (the bottom of Fig. 5.3g),

the Pb 6*s* orbitals are deeper than the Sn 5*s* orbitals, making the *sp* coupling in $(Sn_{0.5}Pb_{0.5})S$ weaker than pure SnS and thus the VBM deeper (i.e. the *IP* larger). Similarly, the Pb 6*p* orbitals are deeper than the Sn 5*p* orbitals, making the CBM of $(Sn_{0.5}Pb_{0.5})S$ deeper than pure SnS (i.e. the *EA* larger).

5.3.4 Microscopic Mechanism of *n*-Type Doping by Pb Substitution

It should be emphased that the *n*-type condution in the $(Sn_{1-xf}Pb_{xf})S$ films was achieved by isovalent substitution of Sn^{2+} by Pb^{2+}, and the doping mechanism cannot be explained by the conventional concept of aliovalent ion doping. To reveal the *n*-type doping mechanism in $(Sn_{1-xf}Pb_{xf})S$, defect calculations were performed for $(Sn_{0.5}Pb_{0.5})S$, as a reprentative of $(Sn_{1-xf}Pb_{xf})S$. Note that S-poor condition is favored for *n*-type doping in SnS to suppress the formation of tin vacancies (V_{Sn}), as discussed in Chapter 4, and the *n*-type $(Sn_{1-xf}Pb_{xf})S$ films were indeed obtained only when grown under S-poor conditions (*i.e.*, at low H_2S pressures). Therefore, the S-poor condition was employed for the following discussion.

Figure 5.4a shows the calculated ΔH of intrinsic defects along with those of Pb impurities in SnS. The detailed discussion for intrinsic defects in SnS has been given in Chapter 4. Here, it should be noted that V_{Sn} is a shallow acceptor responsible for the native *p*-type conduction with an $\varepsilon(2-/0)$ transition at 0.03 eV above the VBM, and that Sn interstitial (Sn_i) is a deeper donor with an $\varepsilon(+/0)$ transition at 0.68 eV below the CBM. For Pb impurities in SnS, three possible sites (i.e. Pb_{Sn} substitutional site, Pb_S antisite, and Pb_i interstitial site) were examined. Among them, Pb_{Sn} has the lowest ΔH which is slightly below zero and is stabilized in the neutral state, indicating Pb substitution of Sn may occur spontaneously to form $(Sn_{1-x}Pb_x)S$ solid solutions and does not accept or release electrons.

Figure 5.4b shows the calculated ΔH for intrinsic defects in $(Sn_{0.5}Pb_{0.5})S$. It can be seen that ΔH of V_{Sn}^{2-} increased significantly compared with that in pure SnS, which is

mainly caused by the lower chemical potential of Sn in $(Sn_{0.5}Pb_{0.5})S$. Besides, V_{Sn} in $(Sn_{0.5}Pb_{0.5})S$ has deep $\varepsilon(n-/0)$ transitions at around 0.31 eV above the VBM, which is 0.28 eV deeper than that in pure SnS. As illustrated in Fig. 5.3f, V_{Sn} has similar absolute energy levels in SnS and $(Sn_{0.5}Pb_{0.5})S$. Because the VBM $(Sn_{0.5}Pb_{0.5})S$ was lowered by the Pb substitution, V_{Sn} relativiely became deeper. In $(Sn_{0.5}Pb_{0.5})S$, V_{Pb} has comparable ΔH with V_{Sn}, but shallower transition levels.

On the other hand, the ΔH of Sn_i^{2+} in $(Sn_{0.5}Pb_{0.5})S$ was largely reduced compared with that in pure SnS, and the $\varepsilon(2+/+)$ and $\varepsilon(+/0)$ transitionsof Sn_i became much shallower, at 0.11 and 0.02 eV below the CBM, respectively. As illustrated in Fig. 5.3f, the shallowing of Sn_i transition levels by 0.66 eV is only partly caused by the reduction of CBM by 0.27 eV and there should be other more important causes. It should be noted he interlayer distance (corresponding to the *a*-axis length) and the *b*-axis lattice parameters were increased by the Pb substitution, as shown in Fig. 5.1d. These geometrical alternations reduce ΔH of Sn_i^{2+} by about 0.78 eV (i.e. $2 \times (0.66 - 0.27)$ eV, where 2 is the charge number) and make the formation of Sn^{2+} much easier. Similarly, Pb_i^{2+} acts as shallow donor, but has slightly larger ΔH (by 0.15 eV) than Sn_i^{2+} due to the larger ionic radius of Pb^{2+} than that of Sn^{2+}.

For quantitative analysis, the equilibrium E_F ($E_{F,e}$) of $(Sn_{0.5}Pb_{0.5})S$ at 300 ºC (i.e., the defect structures at the growth temperature were assumed to be frozen to room temperature) was calculated by considering all the ΔH values and the semiconductor statistics, giving $E_{F,e} - E_V = 0.71$ eV with $[V_{Sn}^{2-}] = 5.5\times10^{13}$, $[V_{Pb}^{2-}] = 4.6\times10^{14}$, $[Sn_i^{2+}] = 6.1\times10^{14}$, and $[Pb_i^{2+}] = 3.2\times10^{13}$ cm^{-3}. Note that the V_S has the charge neutral state at this $E_{F,e}$, and does not contribute to charge doping. Consequently, the free holes were generated at 1.0×10^{15} cm^{-3}, while the larger amounts of free electrons were generated at 1.3×10^{15}

cm^{-3}, resulting in *n*-type doping. Finally, it is concluded that Sn_i and Pb_i are the most plausible origins of the *n*-type conduction in the $(Sn_{xf}Pb_{1-xf})S$ films.

5.4 Conclusions

In summary, *n*-type conduction in SnS was achieved by isovalent Pb substitution with the maximum electron mobility of 7 $cm^2/(Vs)$. The Pb substitution reduced the VBM and CBM, and thus reduced the severity of the doping asymmetry. More importantly, the substitution invoked a geometrical size effect that enlarges the interlayer distance and subquently induces the formation of Sn and Pb cation interstials, which result in the electron doping. The present finding provides a novel idea for carrier doping. Even keeping the same crystal structure and the ion charges, easiness of impurity doping, in particular for atoms / ions with largely-different sizes, depends significantly on the lattice parameters and the internal atomic coordinates, which can be altered also by impurity doping. Further, although substitution doping usually requires aliovalent ion doping to alter the carrier polarity or concentration, geometrical doping has more flexibility because isovalent ion doping would also work for carrier doping.

References

[1] P. W. Atkins, T. L. Overton, J. P. Rourke, M. T. Weller, and F. A. Armstrong, *Inorganic Chemistry*, 5th ed. (Oxford University Press, New York, 2010).

[2] G. Kresse and J. Furthmüller, Phys. Rev. B **54**, 11169 (1996).

[3] V. Leute, A. Behr, C. Hünting, and H. M. Schmidtke, Solid State Ionics **68**, 287 (1994).

[4] J. Y. W. Seto, J. Appl. Phy. **46**, 5247 (1975).

[5] S. M. Sze and K. K. Ng, *Physics of Semiconductor Devices* (John Wiley & Sons, Inc.,

Hoboken, New Jersey, 2007).

[6] S. A. McDonald, G. Konstantatos, S. Zhang, P. W. Cyr, E. J. D. Klem, L. Levina, and E. H. Sargent, Nat. Mater. **4**, 138 (2005).

[7] J. Vidal, S. Lany, M. d'Avezac, A. Zunger, A. Zakutayev, J. Francis, and J. Tate, Appl. Phys. Lett. **100**, 032104 (2012).

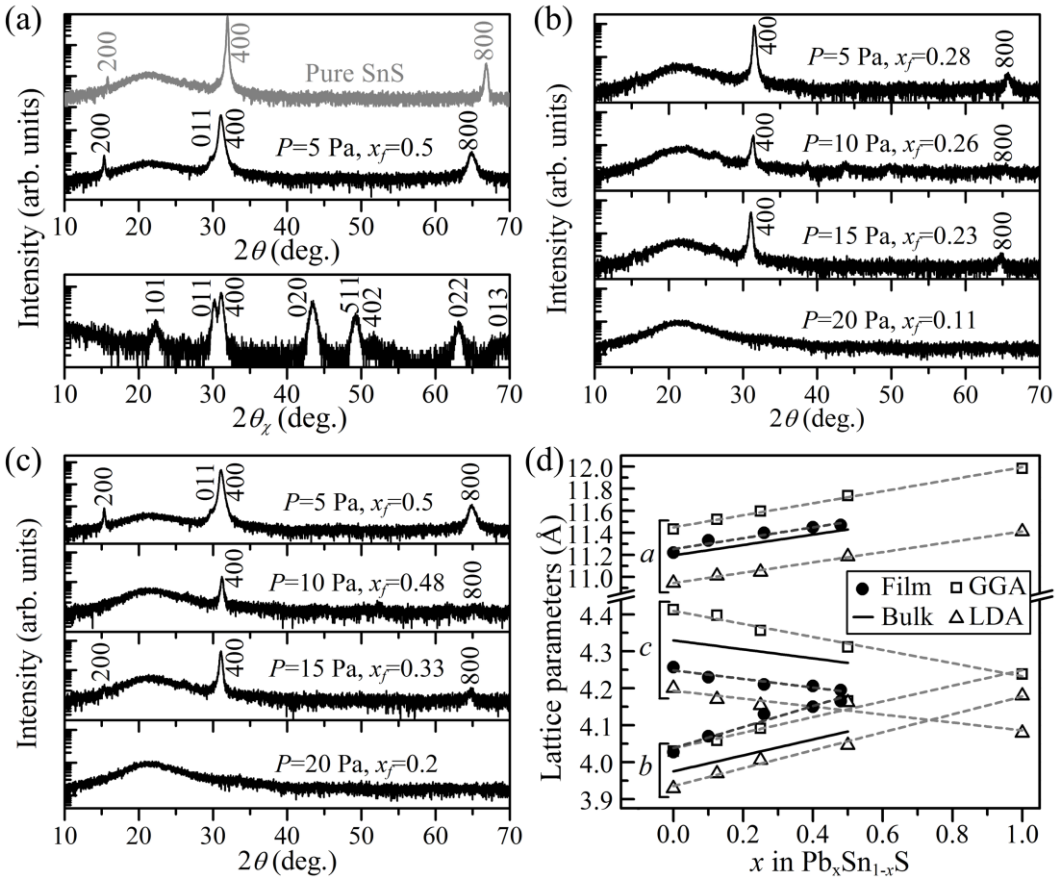

Figure 5.1. Structural properties of $(Sn_{1-xf}Pb_{xf})S$ films. (a) Typical out-of-plane (top panel) and in-plane (bottom panel) XRD patterns of $(Sn_{1-xf}Pb_{xf})S$ film with x_f=0.5 grown at 300 °C and 5 Pa. (b and c) XRD patterns of the $(Sn_{1-xf}Pb_{xf})S$ films grown at 300 °C with various conditions. (d) Lattice parameters (*a*, *b*, *c*) of $(Sn_{1-x}Pb_x)S$ as a function of *x*. The closed circles indicate those obtained with the thin films, the solid lines are those of bulk $(Sn_{1-x}Pb_x)S$ taken from Ref. 3, and the open symbols are the calculation results obtained by DFT in this work. The dashed straight lines are guides for eyes.

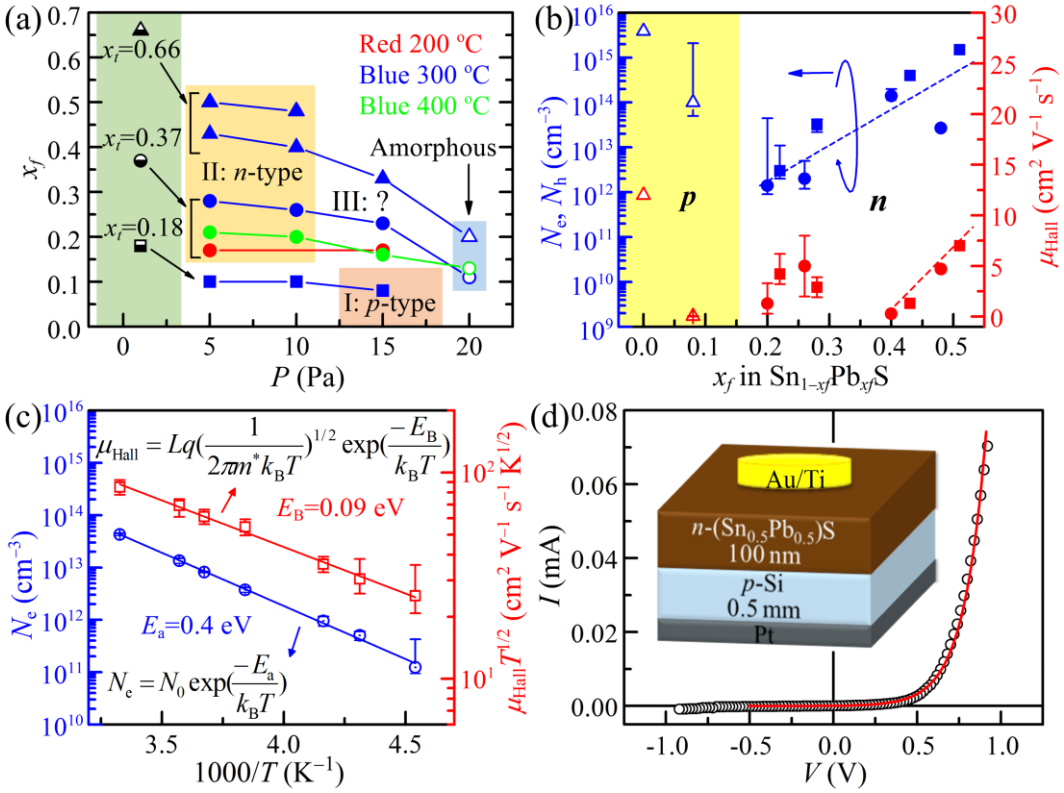

Figure 5.2. (a) Pb content in film (x_f) as a function of pressure (P), substrate temperature (T_S), and Pb content in target (x_t). The half-filled symbols indicate the targets, the closed circles the orthorhombic phase crystalline film, and the open symbols amorphous films. (b) Carrier density and mobility of (Sn$_{1-x_f}$Pb$_{x_f}$)S films as a function of x_f measured by Hall effect. (c) Temperature dependences of electron density (N_e, blue line) and mobility (μ_e, red line) of *n*-type (Sn$_{1-x_f}$Pb$_{x_f}$)S film with x_f = 0.48. (d) I–V characteristics of a *n*-(Sn$_{0.5}$Pb$_{0.5}$)S/*p*-Si pn heterojunction. Inset shows the device structure.

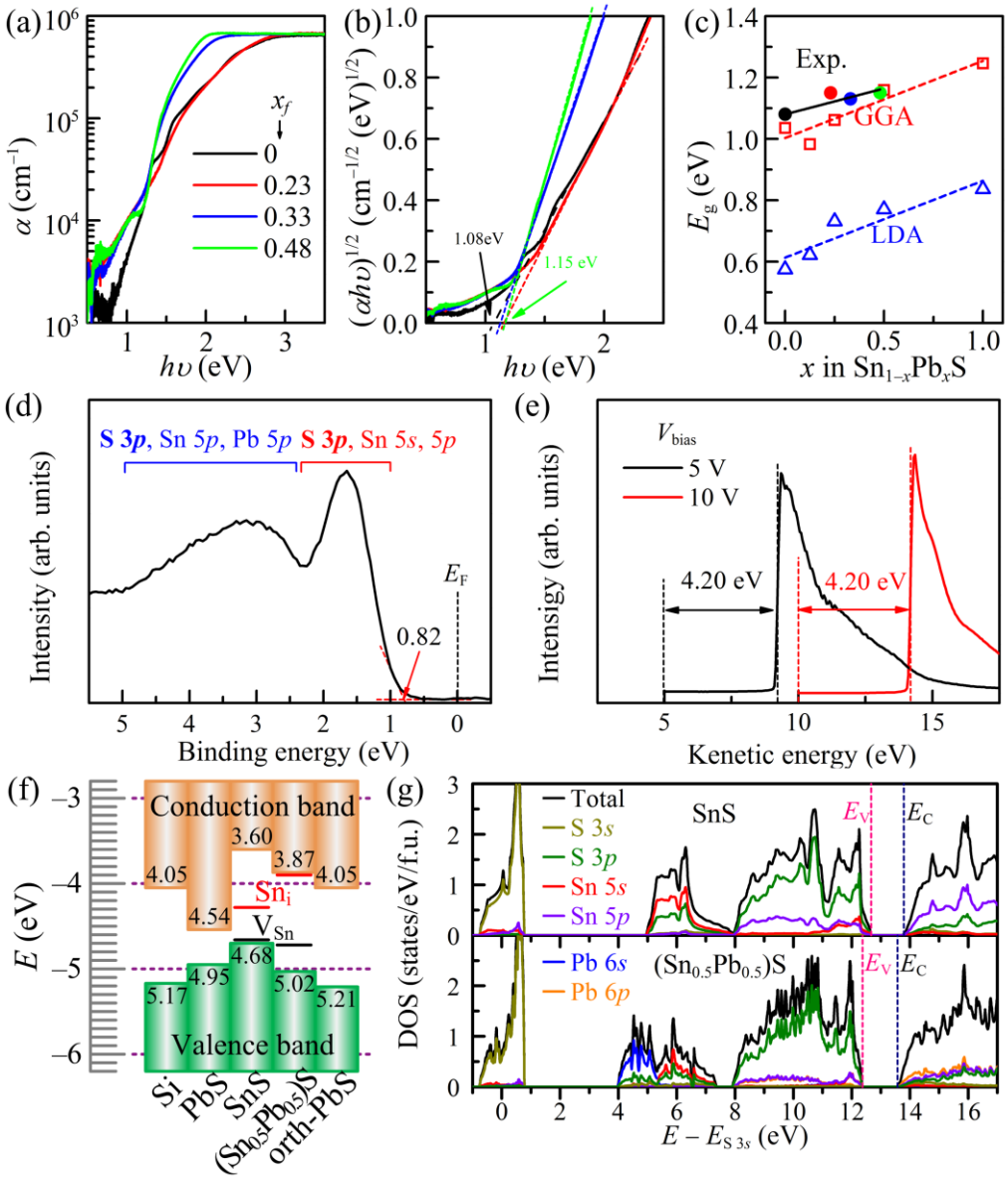

Figure 5.3. (a) Optical absorption spectra and (b) $(\alpha h\upsilon)^{1/2}$–$h\upsilon$ plots of $(Sn_{1-x_f}Pb_{x_f})S$ films with various x_f. (c) Experimental and calculated bandgaps as a function of x_f. (d and e) UPS spectra of the $(Sn_{0.5}Pb_{0.5})S$ film. (f) Band alignment between Si [5], PbS [6], SnS, $(Sn_{0.5}Pb_{0.5})S$ and hypothetical orth-PbS (space group *Pnma*) (see Chapter 4). The ionization potential (*IP*) and electron affinity (*EA*) valuces are given in the figure. The horizontal bars indicate defect levels of Sn vacancy (V_{Sn}) and interstitial (Sn_i) in SnS and $(Sn_{0.5}Pb_{0.5})S$. (g) Total and projected densities of states (DOSs) of SnS and $(Sn_{0.5}Pb_{0.5})S$ calculated with the GGA functionals.

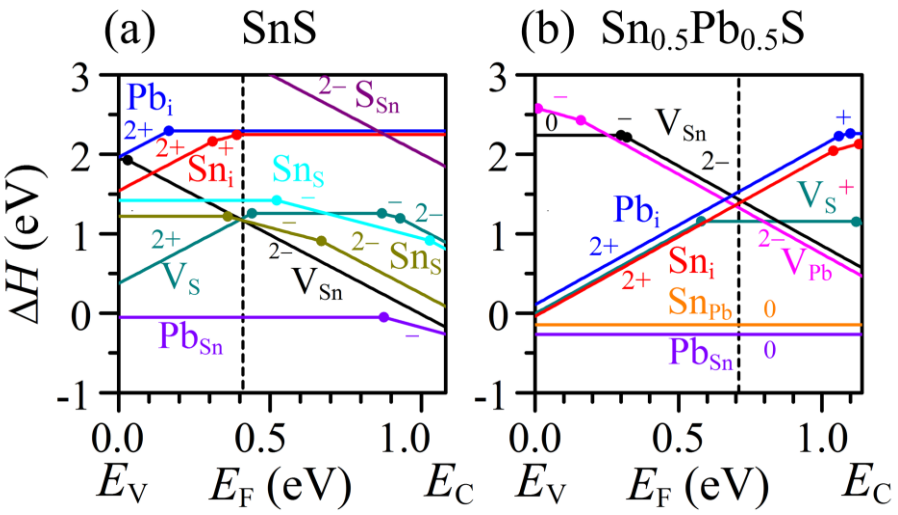

Figure 5.4. (a) Calculated formation enthalpies ΔH of intrinsic defects for (a) pure SnS and (b) $(Sn_{0.5}Pb_{0.5})S$ as a function of E_F at S-poor limit. Those of Pb impurities in SnS are also shown in (a). The values in the figures represent the charge states of the defects in the DFT calculations. The black dashed lines represent the equilibrium E_F ($E_{F,e}$) calculated self-consistently.

Chapter 6

Electronic Structure of a Perovskite Variant Cs_2SnI_6

6.1 Introduction

Lead halide perovskites invoked new development research in the third-generation photovoltaics because of the high power conversion efficiencies (PCE) of those photovoltaic cells as high as 20.1% [1–6]. These compounds are represented by the general chemical formula ABX_3 (A = Cs, CH_3NH_3, or $CH_2NH{=}CH$; B = Pb or Sn; X = I, Br or Cl), where the A cations are located in the cubic network of corner-sharing [BX_6] octahedra. However, these compounds and their devices suffer from the long-term instability in an ambient atmosphere, and the water-soluble toxic lead components are potential risk for the environment issue. Therefore, Sn derivatives of perovskite compounds, $ASnX_3$, have been examined [7–9]. However, these $ASnX_3$ perovskites are very sensitive to the ambient atmosphere (oxygen, moisture, etc.) [7–11]. The instability of $ASnX_3$ is suggested to be related to unintentional oxidation of Sn^{2+} to Sn^{4+}, which might lead to a structural transformation and then degrade the photovoltaic performance [8,9]. Therefore, one may expect that the Sn-based perovskite compounds would be stabilized if the Sn^{4+} is employed. With this line, a class of perovskite variants A_2SnX_6 would be attractive candidates [12], because Sn in A_2SnX_6 is expected to be the 4+ oxidation state upon assumption of the A^+ and X^- oxidation states. Cs_2SnI_6, as a typical example, has been reported to be air-stable and Cs_2SnI_6 based solar cells have exhibited promising PCEs up to 7.8% due to its intrinsic

stability and beneficial optoelectronic properties [13]. On the other hand, determination of oxidation states is not simple and easy in particular for metal cations that take multiple stable oxidation states; e.g., there have been reports on unusual oxidation states in some complex compounds such as $CaCu_3Fe_4O_{12}$ [14]. Similarly, it is not clear whether such a simple ionic $Cs^{+}_2Sn^{4+}I^{-}_6$ model is applicable for such a complex molecular iodosalt compound in which strong covalent bonds may exist.

Based on the simple ionic model, the electronic structure of Sn^{2+}-based $Cs^{+}Sn^{2+}I^{-}_3$ and Sn^{4+}-based $Cs^{+}_2Sn^{4+}I^{-}_6$ can be illustrated schematically by Figs. 6.1a and 6.1b, respectively. While the Sn 5*s* orbitals of $Cs^{+}Sn^{2+}I^{-}_3$ are fully-occupied [10], those of the expected $Cs^{+}_2Sn^{4+}I^{-}_6$ model are unoccupied and contribute to the conduction band minimum (CBM), similar to SnO_2 [15]. The band gaps of both $Cs^{+}Sn^{2+}I^{-}_3$ and $Cs^{+}_2Sn^{4+}I^{-}_6$ are of a charge-transfer type where the valence band maximum (VBM) and CBM are formed mainly by anions and cations, respectively.

In this chapter, the electronic structure and oxidation states of Cs_2SnI_6 were investigated by density theory functional (DFT) calculations. It is found that the VBM consists of I 5*p*–I 5*p* antibonding states, while the CBM, unexpectedly, consists of I 5*p*–Sn 5*s* antibonding states as illustrated in Fig. 6.1c. The Sn 5*s* orbitals indeed form electronic states ~7 eV deeper than the VBM and are fully occupied, indicating that Sn in Cs_2SnI_6 should be in the +2 oxidation state, similar to $CsSnI_3$. The calculated oxidation state of I is a bit smaller than –1 and to be –2/3, because the $[I_6]$ ligand cluster is regarded to have two ligand holes and its oxidation state is $[I_6]^{4-}$ due to the I 5*p*–Cs 6*s* antibonding CBM state. The +2 oxidation state of Sn and the band gap are originated from the intracluster hybridization and stabilized by the strong covalency of the Sn–I bonds.

6.2 Computational Details

DFT calculations were performed using the projector-augmented plane wave (PAW) method implemented in the VASP code [16]. Cs (5*s*)(5*p*)(6*s*), Sn (5*s*)(5*p*), and I (5*s*)(5*p*) are treated as valence states in the PAW potentials. The plane wave cutoff energy was set to 275.4 eV. For the exchange-correlation functional, the local density approximation (LDA) and the Perdew−Burke−Ernzerhof (PBE96) [17] generalized gradient approximation (GGA) functionals underestimated the band gap for Cs_2SnI_6 (0.41 and 0.25 eV, respectively. The experimental value is 1.26 eV [13]). On the other hand, the Heyd–Scuseria–Ernzerhot (HSE06) hybrid functional [18] with the standard mixing parameter of 25% for the exact-exchange term, provided a better band gap value of 0.93 eV. In order to discuss the chemical bonding nature and the origin of the band gap more realistically, the α was adjusted to be 34 % so as to reproduce the reported band gap value, and the HSE06 with this α value will be used for the following discussion. A primitive cell containing one formula unit (f.u.) of Cs_2SnI_6 and a Γ-centered 4×4×4 *k*-mesh were employed for the periodic calculations. Prior to the electronic structure calculations, variable-cell structure relaxations were performed. To reveal the origin of the band gap in Cs_2SnI_6, calculations for hypothetic structures including $[I_6]^0$ cluster, $[SnI_6]^{2-}$ cluster, and $[SnI_6]^{2-}$ sublattice models were also performed. Additionally, chemical bonding analysis was carried out for Cs_2SnI_6 based on the crystal orbital Hamiltonian population (COHP) [19] calculated by a tight binding−linear muffin tin orbitals−atomic sphere approximation (TB-LMTO-ASA) program [20], where positive –COHP values indicate bonding states and vice versa. Integration of the –COHP spectra up to the Fermi level (E_F) yielded –ICOHP values as measure of total overlap populations (i.e., the bond order). The Bader charge analysis was carried out by the Bader program [21] with the charge density obtained by VASP.

6.3 Results and Discussion

6.3.1 Crystal and Electronic Structures of Cs_2SnI_6

Cs_2SnI_6 crystalizes into the face-centered-cubic (fcc) $K_2[PtCl_6]$-type with the space group *Fm*–3*m* (the anti-fluorite structure) and the lattice parameter *a* of 11.65 Å [22]. As shown in Fig. 6.2a, the unit cell is composed of four $[SnI_6]^{2-}$ octahedra at the corners and the face centers and eight Cs^{2+} cations at the tetragonal interstitials. Alternatively, Cs_2SnI_6 can be regarded as a defective variant of the perovskite $CsSnI_3$, in which the $[SnI_6]$ octahedra connect to each other by sharing their corners. The Cs_2SnI_6 structure is obtained by removing a half of the Sn atoms in the $CsSnI_3$ structure at intervals (i.e. the edge centers and the body center in Fig. 6.2a), and thus the corner-shared $[SnI_6]^{2-}$ octahedra become isolated in Cs_2SnI_6. After the half of the Sn atoms are removed, the $[SnI_6]^{2-}$ octahedra shrink slightly, leading to the smaller Sn−I bond length (2.85 Å [22]) in Cs_2SnI_6 than that in $CsSnI_3$ (3.11 Å [10]) as well as the smaller intraoctahedral I−I bond length (4.04 Å) than that of interoctahedral I−I' bond lengths (4.20 Å) (Fig. 6.2b). Table 6.1 summarizes the literature and calculated lattice parameters, bonding lengths, and band gaps. Compared with the LDA and PBE96, the HSE06 gave better results. In particular, when α = 34%, the HSE06 provided the lattice parameters and bonding lengths within 1.5% errors from the room-temperature experimental values and reproduced the experiment band gap value.

Figures 6.3a and 6.3b show the calculated band structure and the total and projected densities of states (DOSs) for Cs_2SnI_6 with the HSE06, respectively. The band structure of Cs_2SnI_6 exhibits a direct band gap of 1.26 eV at the Γ point. The valence band (VB) consists of I 5*p* orbitals, and its band width is small (only 2.38 eV in the total width). Below the VB, there is another I 5*p* band localized between –2.90 and –3.62 eV, which is slightly hybridized with Sn 5*p* orbitals. The Sn 5*s* orbital forms a very deep band between

–7.18 and –6.84 eV, and has little contribution to the VB. On the other hand, the conduction band (CB) extends from 1.26 to 2.56 eV and mainly consists of I 5*p* orbitals hybridized with Sn 5*s* orbitals. This breaks the above expectation in Fig. 6.1b that the CBM would consist of Sn 5*s* orbitals based on the simple ionic model of $Cs^{+}{}_2Sn^{4+}I^{-}{}_6$. Upper CB bands starts from 4.86 eV and separate from the CB with a forbidden gap of 2.30 eV, which consist of Sn 5*p*, Cs 6*s*, 5*d* and I 6*s*, 5*d* orbitals. It can also be seen that the Cs ion has little contribution to the VB and the CB.

6.3.2 Oxidation State of Sn in Cs_2SnI_6

The calculated electronic structure of Cs_2SnI_6 is represented schematically by Fig. 6.1c. Similar to the case of $CsSnI_3$ (Fig. 6.1a), the Sn 5*s* orbitals in $CsSnI_6$ are occupied, which indicates that the real oxidation state of Sn in Cs_2SnI_6 is +2, similar to that in $CsSnI_3$ and not the expected oxidation state of +4. Based on the Sn^{2+} and the Cs^{+} ions in Cs_2SnI_6, the overall charge of the $[I_6]$ cluster must be −4 and then each I atom equivalently has an apparent fractional oxidation state of −2/3 (i.e. the $5p^{5⅔}$ configuration), smaller than the conventional oxidation state of −1 (i.e. the fully occupied $5p^6$ configuration); this is consistent with the above electronic structure that 1/18 of $[I_6]$ 5*p* orbitals (i.e. the single conduction band) are unoccupied. In other words, this electronic structure is understood that the $[I_6]$ ligand cluster has 2 ligand holes $\underline{L}^{+}$ and is represented as $[I^{-}{}_6\underline{L}^{+}{}_2]^{4-}$. This leads to converting the expected formal oxidation state of Sn^{4+} to Sn^{2+} via $Sn^{4+} \rightarrow Sn^{2+}\underline{L}^{+}{}_2$, being consistent with the calculation result.

To further support the +2 oxidation state of Sn, Bader charge analysis was performed for Cs_2SnI_6 as well as other related compounds for comparison. Figure 6.4 shows the Bader oxidation states (*Z*) of Sn calculated from the Bader charges (*N*). It should be noted that although all the *Z* values of the Sn (+1.25 and +1.56, respectively, in typical Sn^{2+}-based

compounds SnO and SnF_2; +2.40 and +2.71, respectively, in typical Sn^{4+}-based compounds SnO_2 and SnF_4) are underestimated, the similar values are obtained if the oxidation states are the same. The Sn in Cs_2SnI_6 has the Z = +1.24, close to those in SnO (+1.25), SnF_2 (+1.56), $CsSnI_3$ (+0.89), binary SnI_2 (+0.98), and SnI_4 (+1.16), while much smaller than those in SnO_2 (+2.40) and SnF_4 (+2.71). This result indicates that the Sn in these compounds have similar oxidation states. The similarity in the Z values between Cs_2SnI_6 and $CsSnI_3$ would be reasonable because the coordination structures around an Sn ion consist of [SnI_6] octahedra and are similar to each other. Interestingly, the SnI_4 has the similar Z value to that in SnI_2 and other Sn^{2+}-based compounds. It implies that, unlike F, anionic I is much larger than F and other halide ions, forms more covalent bonds, and consequently its oxidation ability is not strong enough to oxidize Sn to the +4 oxidation state; SnI_4 is indeed known to be a covalent molecular compound with more covalent I−I bonds [23].

6.3.3 Bonding Nature and Origin of Band Gap in Cs_2SnI_6

The character and strength of chemical bonds were analysized by COHP as shown in Fig. 6.3a along with the total DOS. It can be seen that the Sn–I bonds are all bonding states below E_F while antibonding ones above E_F. It should be noted that there are strong bonding states at ~ –7.4 and –3.2 eV, which originate from the strong covalent interaction between Sn 5*s*/5*p* and I 5*p* states. The strong covalent interaction also leads to the largest –ICOHP (2.41 eV/bond) for the Sn–I bond and would be the origin of the chemical stability of Cs_2SnI_6. In contrast, the small –ICOHP value (0.10 eV/bond) for the Cs–I bond reflects the weak covalent interaction between Cs and I. On the other hand, the –COHP spectra of I–I and I–I' bonds show similar patterns between –2.2 and 0 eV, where the DOS is contributed dominantly by the I 5*p* state. This pattern recalls the familiar molecular orbital (MO)

diagrams of homonuclear molecular dimers and clusters. The large antibonding states at E_F and the negative small –ICOHP values (−0.24 and −0.064 eV/bond for the I−I and I−I' bonds, respectively) imply that the MOs of I 5*p* are almost filled up and no effective bond strength remains between the I ions. The bonding natures are confirmed also by the valence electron density maps on the (200) and (400) planes, as shown in Figs. 6.3b and 6.3c, respectively. It can be seen that the significant electron distribution in the Sn–I bonds clearly indicate the formation of Sn–I covalent bond. In contrast, there is little electrons between Cs–I, meaning that little covalent bond exist in the Cs−I bonds.

To understand the chemical bonding nature and the origin of the band gap in Cs_2SnI_6, DFT calculations for some hypothetic structures were performed. First, the electronic structure for an isolated $[I_6]$ octahedron (i.e., $[I_6]^0$ cluster) was examined, as shown in Fig. 6.6a. According to the energy eigenvalues at the Γ point and the group theory, the 18 I 5*p* orbitals of the $[I_6]$ octahedra are split to 7 groups [24]. The 6 radial I 5*p* orbitals split to 3 groups of a_{1g} (I−I bonding) and e_g & t_{1u} (I−I antibonding). The 12 tangential I 5*p* orbitals form 4 triply degenerated groups of $1t_{1u}$ & t_{2g} (I−I bonding) and t_{2u} & t_{1g} (I−I antibonding). These groups are qualitatively arranged on the energy scale in Fig. 6.6d.

By adding an Sn atom and 2 electrons (transferred from the two Cs atoms, which is ionized to Cs^+ in Cs_2SnI_6) into the $[I_6]$ octahedron, the electronic structure of a $[SnI_6]^{2-}$ octahedron cluster was calculated. The resulted DOSs are shown in Fig. 6.6b and the derived energy levels are qualitatively illustrated in Fig. 6.6d. The shallow Sn 5*p* orbitals slightly hybridize with the $[I_6]$ t_{1u} orbitals, leading to Sn 5*p*–$[I_6]$ t_{1u} bonding states at −2.77 eV and Sn 5p–$[I_6]$ t_{1u} antibonding states at 5.45 eV. The deep Sn 5s orbitals strongly hybridize with the $[I_6]$ a_{1g} orbitals (see the inset to Fig. 6.6d), resulting in the Sn 5*s*–$[I_6]$ a_{1g} bonding states at −6.65 eV and the Sn 5*s*–$[I_6]$ a_{1g} antibonding states at 2.36 eV. These

results are consistent with the –COHP analysis of Sn−I (the second panel of Fig. 6.5a). The Sn 5*s* and 5*p* orbitals have little hybridization with the other 5 groups of I 5*p* orbitals (i.e. t_{2g}, t_{2u}, e_g, t_{1g} and $2t_{1u}$). Note that the $2t_{1u}$ orbitals are fully occupied while the Sn 5*s*–[I_6] a_{1g} antibonding orbital is unoccupied in the $[SnI_6]^{2-}$ cluster, and the $[SnI_6]^{2-}$ cluster forms a semiconductor-type electronic structure with the band gap of 2.36 eV.

Finally, a $[SnI_6]^{2-}$ sublattice model in which $[SnI_6]^{2-}$ are located at the corner and the face-center sites in the unit cell of Cs_2SnI_6 (i.e., the Cs^+ ions are removed from Cs_2SnI_6) was examined. The resulted DOSs (Fig. 6.6c) are very similar to that of Cs_2SnI_6 (Fig. 6.3b), indicating that Cs^+ cations have limited contribution to the electronic structure of Cs_2SnI_6 except for slightly pushing up the bands above E_F. The localized orbitals in the $[SnI_6]^{2-}$ cluster model expand into dispersed bands made of the $[SnI_6]^{2-}$ sublattice. The unoccupied Sn 5*s*–[I_6] a_{1g} antibonding orbitals forms the CBM, and the occupied [I_6] 5*p* (t_{2g}, t_{2u}, e_g, t_{1g}, and $2t_{1u}$) orbitals, which are antibonding between two I ions while non-bonding states to Sn, form the VBM.

6.4 Conclusions

In conclusion, the real oxidation state of Sn in Cs_2SnI_6 is +2, which is the same as that in $CsSnI_3$ but different from the previously-expected value +4. DFT calculations clarified that the +2 oxidation state and the band gap are formed due to the intracluster hybridization in in the [SnI_6] clusters and stabilized by the strong covalent nature of the Sn–I bonds. The Sn^{2+} state and the apparently $I^{-2/3}$ state form the shortened and strengthened Sn–I chemical bonds, making the isolated $[SnI_6]^{2-}$ similar to stable functional groups like $[SO_4]^{2-}$. The present result also shows the conventional ionic model is invalid for *p*-block metal-iodide

based perovskites in which ionic bonds and covalent bonds coexist and compete, and provides a guiding principle to design new perovskite-based photovoltaic materials.

References

[1] Best Research-Cell Efficiencies, National Renewable Energy Laboratory, http://www.nrel.gov/ncpv/, November 2014.

[2] A. Kojima, K. Teshima, Y. Shirai, and T. Miyasaka, J. Am. Chem. Soc. **131**, 6050 (2009).

[3] H. Zhou, Q. Chen, G. Li, S. Luo, T. Song, H.-S. Duan, Z. Hong, J. You, Y. Liu, and Y. Yang, Science **345**, 542 (2014).

[4] N. J. Jeon, J. H. Hoh, Y. C. Kim, K. S. Yang, S. Ryu, and S. I. Seok, Nat. Mater. **13**, 897 (2014).

[5] J.-H. Im, I.-H. Jang, N. Pellet, M. Grätzel, and N.-G. Park, Nat. Nanotech. **9**, 927 (2014).

[6] Y. Kutes, L. Ye, Y. Zhou, S. Pang, B. D. Huey, and N. P. Padture, J. Phys. Chem. Lett. **5**, 3335 (2014).

[7] F. Hao, C. C. Stoumpos, D. H. Cao, R. P. H. Chang, and M. G. Kanatzidis, Nat. Photon. **8**, 489 (2014).

[8] N. K. Noel, S. D. Stranks, A. Abate, C. Wehrenfennig, S. Guarnera, A.-A. Haghighirad, A. Sadhanala, G. E. Eperon, S. K. Pathak, M. B. Johnson, A. Petrozza, L. M. Herz, and H. J. Snaith, Energy Environ. Sci. **7**, 3061 (2014).

[9] I. Chung, B. Lee, J. He, R. P. H. Chang, and M. G. Kanatzidis, Nature **485**, 486 (2012).

[10] I. Chung, J.-H. Song, J. Im, J. Androulakis, C. D. Malliakas, H. Li, A. J. Freeman, J. T.

Kenney, and M. G. Kanatzidis, J. Am. Chem. Soc. **34**, 8579 (2012).

[11] Y. Zhou, H. F. Garces, B. S. Senturk, A. L. Ortiz, and N. P. Padture, Mater. Lett. **110**, 127 (2013).

[12] M. G. Brik and I. V. Kityk, J. Phys. Chem. Solids **72**, 1256 (2011).

[13] B. Lee, C. C. Stoumpos, N. Zhou, F. Hao, C. Malliakas, C.-Y. Yeh, T. J. Marks, M. G. Kanatzidis, and R. P. H. Chang, J. Am. Chem. Soc. **136**, 15379 (2014).

[14] W.-T. Chen, T. Soito, N. Hayashi, M. Takano, and Y. Shimakawa, Sci. Rep. **2**, 449 (2012).

[15] J. Robertson, J. Phys. C Solid State Phys. **12**, 4767 (1979).

[16] G. Kresse and J. Furthmüller, Phys. Rev. B **54**, 11169 (1996).

[17] J. P. Perdew, K. Burke, and M. Ernzerhof, Phys. Rev. Lett. **77**, 3865 (1996).

[18] J. Heyd, G. E. Scuseria, and M. Ernzerhof, J. Chem. Phys. **124**, 219906 (2006).

[19] R. Dronskowski and P. E. Blöchl, J. Phys. Chem. **97**, 8617 (1993).

[20] O. Jepsen, A. Burkhardt, and O. K. Andersen, The program TB-LMTO-ASA, Ver.4.7; Max-Planck-Institut für Festkörperforschung, Stuttgart, Germany, 1999.

[21] W. Tang, E. Sanville, and G. Henkelman, Phys.: Condens. Matter. **21**, 084204 (2009).

[22] W. Werker, Recl. Trav. Chim. Pays-Bas Belg. **58**, 257 (1939).

[23] M. Cordey-Hayes, J. Inorg. Nucl. Chem. **26**, 915 (1964).

[24] G. V. Vajenine and R. Hoffmann, J. Am. Chem. Soc. **120**, 4200 (1998).

Table 6.1. Literature and calculated lattice parameters, bonding lengths and band gaps of Cs_2SnI_6.

	Exp.	LDA	PBE96	HSE06 (α=25%)	HSE06 (α=34%)
a (Å)	11.65 [22]	11.26	12.03	11.86	11.82
Cs–I (Å)	4.12 [22]	3.98	4.25	4.19	4.18
Sn–I (Å)	2.85 [22]	2.83	2.91	2.89	2.88
I–I (Å)	4.04 [22]	4.00	4.11	4.09	4.07
I–I' (Å)	4.20 [22]	3.96	4.39	4.30	4.29
E_g (eV)	1.26 [13]	0.13	0.25	0.93	1.26

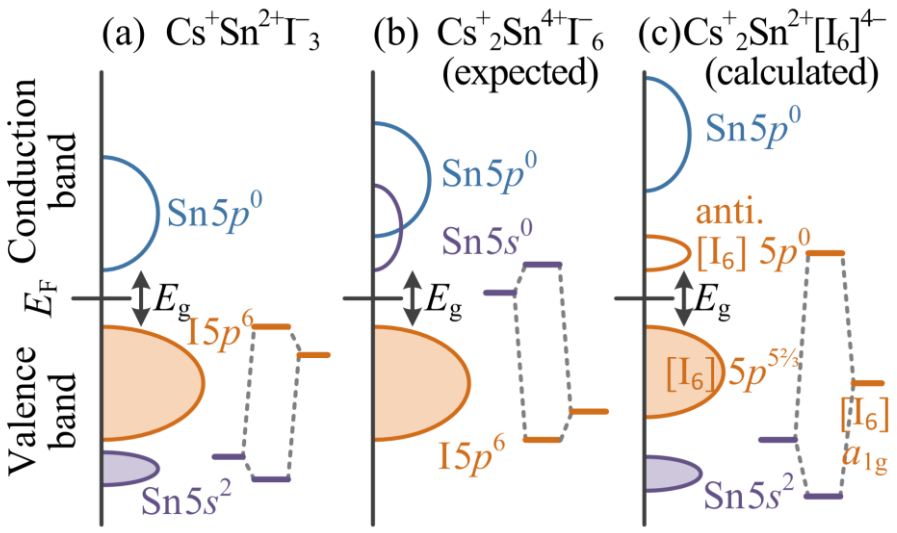

Figure. 6.1. Schematic electronic structure for (a) $Cs^+Sn^{2+}I^-_3$ (b) previously-expected $Cs^+_2Sn^{4+}I^-_6$, and (c) calculated $Cs^+_2Sn^{2+}[I_6]^{4-}$. The molecular orbital energy diagrams for Sn 5*s*–I 5*p* bonds are also shown schematically on bottom-left in each figure.

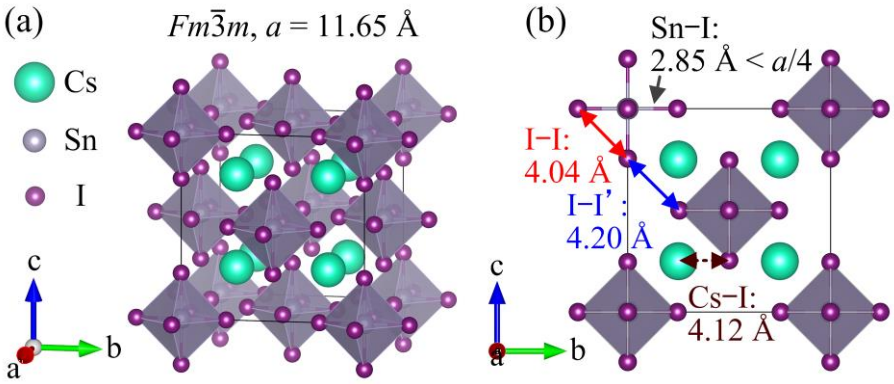

Figure. 6.2. (a) Crystal structure of Cs_2SnI_6 and (b) top view of (a). The bonding lengths from Ref. 22 are shown in (b).

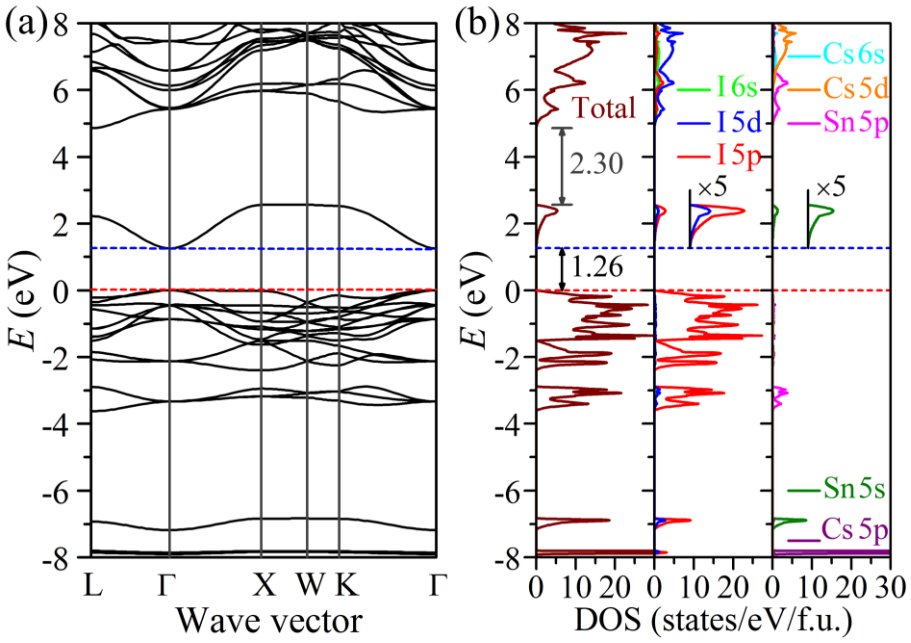

Figure. 6.3. (a) Band structure and (b) total and projected DOSs of Cs_2SnI_6 calculated with HSE06. The red and blue dashed lines mark the VBM and the CBM, respectively.

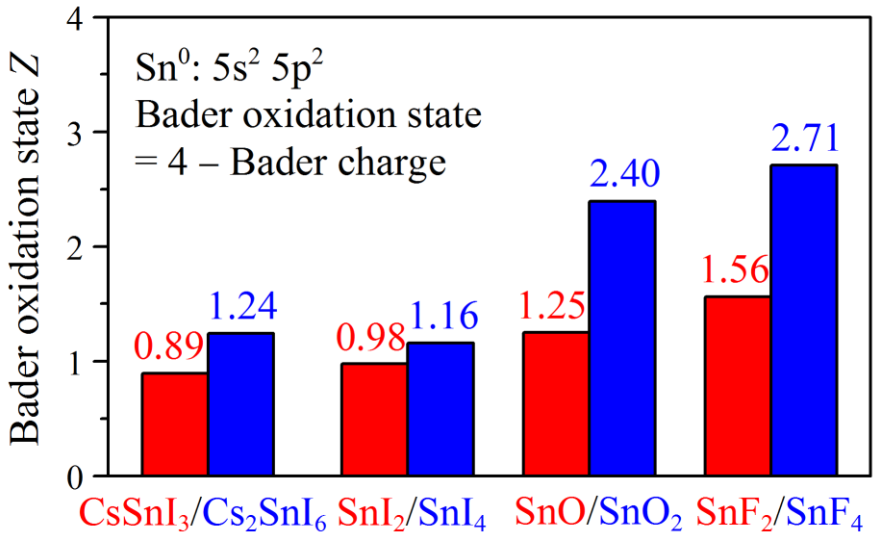

Figure. 6.4. Bader oxidation states Z of Sn in Sn-based compounds.

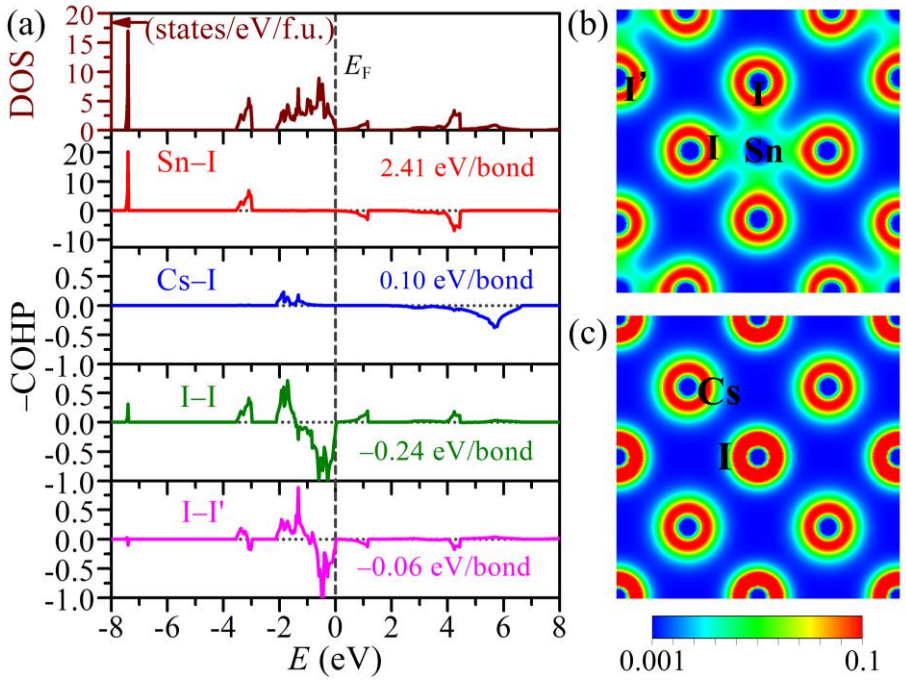

Figure. 6.5. (a) Calculated –COHPs for Sn−I, Cs−I, I−I, and I−I' bonds. The total DOS is shown in the top panel for comparison. The –ICOHP values for Sn−I, Cs−I, I−I, and I−I' are also shown in respective panels. (b and c) Valence electron density maps on the (b) (200) and (c) (400) planes.

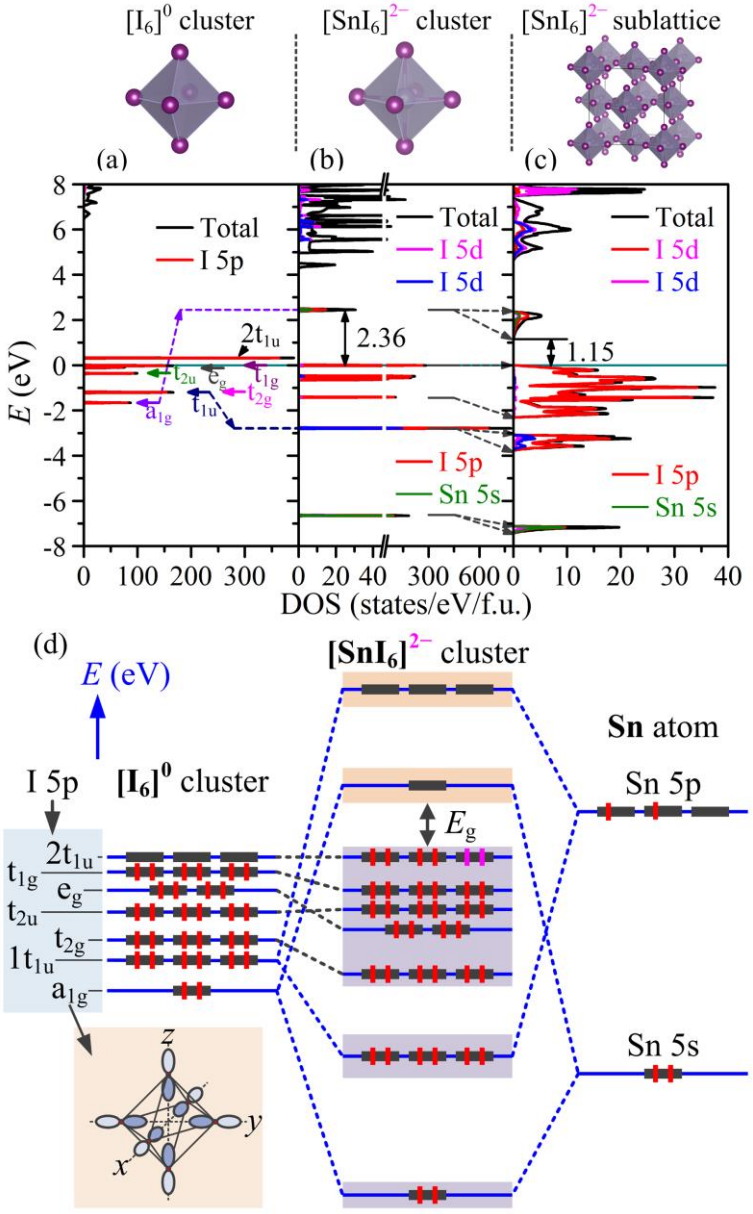

Figure 6.6. Total and projected DOSs of (a) $[I_6]^0$ cluster, (b) $[SnI_6]^{2-}$ cluster, and (c) $[SnI_6]^{2-}$ sublattice models. The structures of the $[I_6]$ cluster, the $[SnI_6]$ cluster and the $[SnI_6]$ sublattice models are shown on top. (d) Qualitative interaction diagram for the $[I_6]^0$ cluster, the $[SnI_6]$ cluster, and the $[SnI_6]$ sublattice models. The orbitals are qualitatively arranged on the energy scale. Inset of (d) shows a schematic illustration of $[I_6]$ a_{1u} orbital.

Chapter 7

Intrinsic Defects in a Perovskite Variant Cs_2SnI_6

7.1 Introduction

In Chapter 6 the density functional theory (DFT) calculations indicate that the real oxidation state of Sn in Cs_2SnI_6 is closer to +2, similar to $CsSnI_3$, which originates from the nominal formula $Cs^{+}{}_2Sn^{2+}[I_6]^{4-}$. It is known well that the typical Sn^{2+}-based compounds, including SnO [1], SnS [2], and $CsSnI_3$ [3], in general, intrinsically exhibit good *p*-type conductivity because V_{Sn} in these compounds are easily formed and act as shallow acceptors to produce mobile holes. On the other hand, Cs_2SnI_6 have not shown *p*-type conductivity unlike the other Sn^{2+}-based compounds and have shown *n*-type conduction or insulating behavior depending on the synthetic routes. Lee *et al.* [4] reported the native *n*-type conduction with electron density (*n*) of ~1×10^{14} cm^{-3} in polycrystalline Cs_2SnI_6 pellets annealed at 200 °C, while Zhang *et al.* [5] observed very high resistivity in room temperature-processed Cs_2SnI_6. Therefore, in order to clarify the intrinsic nature of Cs_2SnI_6 and its origin, a systematic theoretical study on the intrinsic defects is important, which will provide a guiding principle for tuning its properties for photovoltaic and other semiconductor applications.

In this chapter, the formation enthalpy (ΔH) of intrinsic defects in Cs_2SnI_6 was studied by DFT calculations. It is clarified that I vacancy (V_I) and Sn interstitial (Sn_i) are mainly responsible for the intrinsic *n*-type conductivity in Cs_2SnI_6. V_{Sn}, which is usually a

dominant *p*-type defect in Sn^{2+}-based compounds, is hardly formed in Cs_2SnI_6 because of its high ΔH resulted from the low chemical potential of Sn. It is also clarified that intrinsic *p*-type conductivity is hardly be attained in pure Cs_2SnI_6 due to the absence of an effective acceptor with sufficiently low ΔH and a shallow transition level. The origin of deep transition levels of the dominant defects in Cs_2SnI_6 is also discussed.

7.2 Computational Details

Defect calculations were performed in the framework of DFT using the projector-augmented wave (PAW) method as implemented in the VASP code [6]. Cs (5s)(5p)(6s), Sn (5s)(5p), and I (5s)(5p) orbitals are treated as valence states in the PAW potentials. The cutoff energy for the basis set was set to 275.4 eV. A 72-atoms supercell (2×2×2 primitive cells) was used to model the intrinsic defects. Atomic positions were relaxed until all the forces on the atoms were less than 0.05 eV/Å, employing a Γ-centered 3×3×3 *k*-mesh and the Perdew−Burke−Ernzerhof (PBE96) [7] generalized gradient approximation (GGA) functionals. The total energies were calculated by Γ point-only calculation using the Heyd−Scuseria−Ernzerhof (HSE06) [8] hybrid functional with 34% of exact nonlocal exact exchange, which was adjusted to reproduce the experimental band gap of 1.26 eV [4].

ΔH of a defect (D) in a charge state q was calculated through the equation [9]

$$\Delta H_{D,q}(E_F,\mu) = E_{D,q} - E_H - \Sigma n_\alpha \mu_\alpha + q(E_F+E_V+\Delta V), \quad (7.1)$$

where $E_{D,q}$ is the total energies of the supercell with the defect D in the charge state q, and E_H that of the perfect host supercell. n_α indicates the number of α atoms added ($n_\alpha > 0$) or removed ($n_\alpha < 0$), and μ_α is the chemical potential of an α atom with respect to that of an elemental phase (μ_α^{el}) by $\mu_\alpha = \mu_\alpha^{el} + \Delta\mu_\alpha$. The chemical potentials of elemental phases μ_{Cs}^{el},

μ_{Sn}^{el}, and μ_I^{el} are taken from elemental Cs (the cubic phase, space group *Fm*–3*m*) [10], β-Sn (tetragonal, space group $I4_1/amd$) [11], and I_2 (orthorhombic, space group *Cmca*) [12], respectively. E_F is the Fermi level relative to the valence band maximum (VBM, E_V), which was corrected by ΔV through electrostatic potential alignment [13]. For charged defects, the image charge correction was also applied to eliminate the supercell finite-size effects [13].

μ_α varies depending on the experimental condition during growth or annealing. First, to stabilize the Cs_2SnI_6 phase, the following thermodynamic equation must be satisfied

$$2\Delta\mu_{Cs} + \Delta\mu_{Sn} + 6\Delta\mu_I = \Delta H(Cs_2SnI_6) = -10.49 \text{ eV}, \quad (7.2)$$

where $\Delta H(Cs_2SnI_6)$ is ΔH of Cs_2SnI_6 referred to the elemental Cs, β-Sn, and I_2. To avoid the coexistence of the Cs, the Sn, and the I_2 elemental phases, the additional conditions, $\Delta\mu_{Cs} < 0$, $\Delta\mu_{Sn} < 0$, and $\Delta\mu_I < 0$, are required. To exclude the secondary phases CsI (cubic, space group *Pm*−3*m*) [14], SnI_2 (monoclinic, space group *C*2/*m*) [15], SnI_4 (cubic, space group *Pa*−3) [16], and $CsSnI_3$ (cubic, space group *Pm*−3*m*) [17], the following constraints must be satisfied as well.

$$\Delta\mu_{Cs} + \Delta\mu_I < \Delta H(CsI) = -3.80 \text{ eV}, \quad (7.3)$$

$$\Delta\mu_{Sn} + 2\Delta\mu_I < \Delta H(SnI_2) = -1.69 \text{ eV}, \quad (7.4)$$

$$\Delta\mu_{Sn} + 4\Delta\mu_I < \Delta H(SnI_4) = -2.40 \text{ eV}, \quad (7.5)$$

$$\Delta\mu_{Cs} + \Delta\mu_{Sn} + 3\Delta\mu_I < \Delta H(CsSnI_3) = -5.77 \text{ eV}. \quad (7.6)$$

With all these equations satisfied, $\Delta\mu_{Sn}$ and $\Delta\mu_I$ (and, thus, $\Delta\mu_{Cs}$ determined from Eq 7.2) are limited to a narrow region (the yellow region in Fig. 7.1). The narrow shape indicates that the growth or annealing conditions should be carefully controlled to produce the single-phase Cs_2SnI_6, similar to the cases of $CsSnI_3$ [3] and $MAPbI_3$ [18].

7.3 Results and Discussion

7.3.1 Properties of Intrinsic Defects in Cs_2SnI_6

I have considered intrinsic point defects in Cs_2SnI_6 including three vacancies (V_{Cs}, V_{Sn}, V_I), three interstitials (Cs_i, Sn_i, I_i), two cation substitutions (Cs_{Sn}, Sn_{Cs}), and four antisites (Cs_I, Sn_I, I_{Cs}, I_{Sn}). Two representative chemical potential conditions in Fig. 7.1 are chosen for the following discussion; ($\Delta\mu_{Sn}$, $\Delta\mu_I$) at A (I-rich condition) and D (I-poor) points. The calculated $\Delta H_{D,q}$ under the I-rich and I poor conditions are plotted as a function of E_F in Figs. 7.2a and 7.2b, respectively. The calculated transition levels $\varepsilon(q/q')$ are plotted relative to the conduction band minimum (CBM) and valence band maximum (VBM) in Fig. 7.3. Out of the twelve intrinsic defects, four (V_I, Sn_i, Cs_I and V_{Cs}) have a sufficiently small ΔH (e.g., < 1.0 eV) to influence the electrical properties. Among them, V_I has the lowest ΔH ($\leq$0.74 eV and $\leq$0.28 eV under I-rich and I-poor conditions, respectively) and acts as a deep donor with $\varepsilon(0/+1)$ = 0.74 eV above VBM (i.e., 0.52 eV below the conduction band edge, CBM), which is mainly responsible for the *n*-type condition of Cs_2SnI_6. Under the I-poor condition, Sn_i has a small ΔH ($\leq$1.18 eV) and a shallower transition $\varepsilon(0/+1)$ at 0.11 eV below the CBM. Therefore, Sn_i as well as V_I are also dominant donors for *n*-type conduction. Cs_I is of a low ΔH but stabilized in the neutral charge state at high E_F (i.e. *n*-type conditions); therefore, it does not contribute to the *n*-type conduction. Only Sn_I is a shallow donor in Cs_2SnI_6 with the $\varepsilon(0/+2)$ above the CBM, as seen in Figs. 7.2b and 7.3. However, because of its relatively high ΔH, Sn_I has limited contribution to the *n*-type conductivity even under the I-poor condition. On the other hand, under the I-rich condition, V_{Cs} has a low ΔH ($\leq$1.37 eV) and can act as a deep acceptor, but at E_F only above 0.51 eV from the VBM and the hole density produced is too low to compensate the electrons released by V_I.

The other intrinsic defects with prohibitively high ΔH are displayed by gray dashed lines in Fig. 7.2. It should be noted that V_{Sn} in Cs_2SnI_6 has high ΔH values under all the chemical potentials and is as large as 3.63 eV even under the Sn-poor condition (A point), as seen in Table 7.1. This is strikingly different from the cases of the typical Sn^{2+}-based semiconductors such as SnO, SnS, and $CsSnI_3$, in which the ΔH values of V_{Sn} (at the VBM) are usually very small under the Sn-poor condition (i.e., 1.3 eV at E_V for SnO [1], 0.8 eV for SnS [2], and 0.3 eV for $CsSnI_3$ [3]). The unusually high ΔH of V_{Sn} in Cs_2SnI_6 should originate from the extremely low $\Delta\mu_{Sn}$ values in Cs_2SnI_6 (see Fig. 7.1) in comparision with $CsSnI_3$. For the same reason, the substitutions of Sn by Cs and I (i.e., Cs_{Sn} and I_{Sn}) also have similarly high ΔH values.

Since it is found any intrinsic defect does not work as an effective *p*-type source from the I-rich to I-poor conditions, as shown above, it would be difficult to achieve intrinsic *p*-type conduction in pure Cs_2SnI_6. Instead, Cs_2SnI_6 intrinsically exhibits *n*-type conduction due to the easy formation of V_I and Sn_i donors. For quantitative analysis, the equilibrium E_F ($E_{F,e}$) at room temperature were calculated by solving semiconductor statistic equations. Under the I-rich limit at the A point, $E_{F,e}$ is 0.96 eV above the VBM (see the vertical dotted line in Fig. 7.2a) and the corresponding electron density (n) is ~10^{12} cm^{-3}, which is not easily determined by a Hall effect measurement. Under the I-poor condition at the D point, $E_{F,e}$ is 1.14 eV above the VBM (see the vertical dotted line in Fig. 7.2b) and n is ~10^{16} cm^{-3}. These theoretical results seem to explain the experimental results reported to date; i.e., the electrical properties of Cs_2SnI_6 ranging from insulating [5] to low-density *n*-type conduction (n ~1×10^{14} cm^{-3}) [4].

7.3.2 Origins of Deep Defect Levels in Cs_2SnI_6

The $\varepsilon(q/q')$ of the dominant defects are important in particular for solar cells because

$\varepsilon(q/q')$ in the band gap indicates that they work as an electron trap, hole trap, and/or a recombination center, which deteriorate the device performances. The dominant defects V_{Pb} in $MAPbI_3$ [17] and V_{Sn} in $CsSnI_3$ [3] have transition levels deeper than their VBMs and are inert. Also in $CuInSe_2$, the dominant defect V_{Cu} has an $\varepsilon(-1/0)$ at only 0.03 eV above the VBM [19]. The very shallow V_{Cu} results in good *p*-type good conduction but does not deteriorate the photovoltaic performance. In contrast, in Cs_2SnI_6, all the dominant defects (Cs_i, Sn_i, V_I, V_{Cs} as shown by the solid lines in Fig. 7.2) have $\varepsilon(q/q')$ in the band gap, as seen in Fig. 7.3, which would more or less hinder photovoltaic performances through short diffusion/drift length and fast recombination of photo-generated carriers, in particular when processed under the I-poor condition. These deep defects can, however, be significantly avoided by using I-rich conditions, which is located at the phase boundary between Cs_2SnI_6 and elemental I (e.g. the B point as shown in Fig. 7.2a), because their ΔH are considerably increased as seen in Table 7.1.

The defect properties as well as electronic structure of a material can qualitatively understood well based on the molecular orbital theory [17,20,21]. Here I provide a simplified interpretation for the origin of the deep nature of the intrinsic defects in Cs_2SnI_6 in comparison with representative Sn^{2+}-based compounds such as SnO and $CsSnI_3$, by focusing on cation and anion vacancies, which generally have low ΔH and play important role on electrical properties of these compounds. Fig. 7.4a shows the calculated densities of states (DOSs) and projected DOSs (PDOSs) for SnO, $CsSnI_3$ and Cs_2SnI_6, where the energy is aligned by Sn 4*d* and Cs 5*s* so as to compare the energy levels. Figs. 7.4b–7.4d show the schematic energy diagrams that are derived From Fig. 7.4a. As depicted in Fig. 7.4b, the VBM of SnO consists of the antibonding states of Sn 5*s* and O 2*p* orbitals (region I in the top panel of Fig. 7.4a). For a cation vacancy V_M, it is known that the V_M transition

energy in a simple oxide is ~1 eV above VBM e.g. in ZnO [22]. Also for the SnO case, the V_{Sn} level is above the O 2*p* band (region II of the top panel of Fig. 7.4a) similar to the V_M in the simple oxides. As the VBM made by Sn 5s level is similarly high, and consequently the V_{Sn} level in SnO forms the shallow acceptor level. On the other hand, the CBM consists of antibonding Sn 5*p*–O 2*p* states and is close to the Sn 5*p* level due to the ionic character of SnO. For an oxygen vacancy V_O, the defect state is composed of the Sn non-bonding state, which drops slightly from the CBM [21], resulting in the shallow nature of V_O. Fig. 7.4c schematically illustrates the formation of the CBM, VBM, V_{Sn}, and V_I in $CsSnI_3$. Since the Cs cation does not contribute to the electronic structure around the band gap, the electronic structure of $CsSnI_3$ is similar to that of SnO if O is replaced with I. As a result, V_{Sn} and V_I in $CsSnI_3$ form a shallow acceptor and a shallow donor, respectively, [3] similar to those in SnO.

In contrast, Cs_2SnI_6 has a strikingly different electronic structure (see the bottom panel of Fig. 7.4a), which is schematically illustrated in Fig. 7.4d. Because the removal of the half of Sn atoms and the subsequent isolation of the $[SnI_6]^{4-}$ octahedra, the energy splitting between the bonding and the antibonding states of Sn 5*s*–I 5*p* (see regions IV and I, respectively, in the bottom panel of Fig. 7.4a) become very large, and the Sn 5*s*–I 5*p* bonding energies are deepened; on the other hand, the Sn 5*s*–I 5*p* antibonding energies are pushed up and become unoccupied states, forming the CBM of Cs_2SnI_6. The VBM of Cs_2SnI_6 is composed of the I 5*p*–I 5*p* antibonding states (region II in the bottom panel of Fig. 7.4a) and is much deeper than that of $CsSnI_3$. This seems to explain the reported experimental observation that Cs_2SnI_6 has a deeper VBM than $CsSnI_3$ (–5.94 eV and –5.74 eV), respectively [5]. It should be noted that the Sn 5*s* level in Cs_2SnI_6 is deep similar to SnO and $CsSnI_3$ and almost fully occupied, indicating the +2 oxidation state of Sn. It is

seen that the V_{Sn} level in Cs_2SnI_6 is similar to those in SnO and $CsSnI_3$, while the VBM level in Cs_2SnI_6 is far below that in $CsSnI_3$; consequently, the V_{Sn} in Cs_2SnI_6 is a deep acceptor even close to the CBM, which explains why Cs_2SnI_6 is not an intrinsic *p*-type semiconductor unlike $CsSnI_3$.

7.4 Conclusions

In conclusion, the formation energies of intrinsic defects in the Cs_2SnI_6 perovskite variant were inverstigated using DFT calculations. The dominant defects are donor V_I and Sn_i, giving the calculated electron densities of 10^{12}–10^{16} cm^{-3}. Unlike other Sn^{2+}-based *p*-type semiconductor such as SnO, SnS and $CsSnI_3$, the V_{Sn} in Cs_2SnI_6 has a very high $\Delta H > 3.6$ eV and are hardly formed due to the extremely low chemical potential of Sn in Cs_2SnI_6. The energy levels of the dominant defects are deep in the band gap and would work as recombination centers in photovoltaic applications. On the other hand, their formations would be practically suppressed by employing an I-rich synthesis condition where their densities are negligibly small due to the high ΔH. These results explain the reported experimental results and provide a clue to better understanding the unusual defect physics in *p*-block metal-based compounds.

References

[1] A. Togo, F. Oba, I. Tanaka, and K. Tatsumi, Phys. Rev. B **74**, 195128 (2006).

[2] Z. Xiao, F.-Y. Ran, H. Hosono, and T. Kamiya, Appl. Phys. Lett. **106**, 152103 (2015).

[3] P. Xu, S. Chen, H.-J. Xiang, X.-G. Gong, and S.-H. Wei, Chem. Mater. **26**, 6068 (2014).

[4] B. Lee, C. C. Stoumpos, N. Zhou, F. Hao, C. Malliakas, C.-Y. Yeh, T. J. Marks, M. G.

Kanatzidis, and R. P. H. Chang, J. Am. Chem. Soc. **136**, 15379 (2014).

[5] J. Zhang, C. Yu, L. Wang, Y. Li, Y. Ren, and K. Shum, Sci. Rep. **4**, 6954 (2014).

[6] G. Kresse and J. Furthmüller, Phys. Rev. B **54**, 11169 (1996).

[7] J. P. Perdew, K. Burke, and M. Ernzerhof, Phys. Rev. Lett. **77**, 3865 (1996).

[8] J. Heyd, G. E. Scuseria, and M. Ernzerhof, J. Chem. Phys. **118**, 8207 (2003).

[9] C. G. Van de Walle and J. Neugebauer, J. Appl. Phys. **95**, 3851 (2004).

[10] C. E. Weir, G. J. Piermarini and S. Block, J. Chem. Phys. **54**, 2768 (1971).

[11] E. R. Jette and E. B. Gebert, J. Chem. Phys. **1**, 753 (1933).

[12] R. M. Ibberson, O. Moze and C. Petrillo, Mol. Phys. **76**, 395 (1992).

[13] S. Lany and A. Zunger, Phys. Rev. B **78**, 235104 (2008).

[14] A. Smakula and J. Kalnajs, Phys. Rev. **99**, 1737 (1955).

[15] R. A. Howie, W. Moser, and I. C. Trevena, Acta Crystallogr. **B28**, 2965 (1972).

[16] R. G. Dickinson, J. Am. Chem. Soc. **45**, 958 (1923).

[17] I. Chung, J. H. Song, J. Im, J. Androulakis, C. D. Malliakas, H. Li, A. J. Freeman, J. T. Kenney, and M. G. Kanatzidis, J. Am. Chem. Soc. **134**, 8579 (2012).

[18] W.-J. Yin, T. Shi, and Y. Yan, Appl. Phys. Lett. **104**, 063903 (2014).

[19] S. B. Zhang, S.-H. Wei, A. Zunger, and H. Katayama-Yoshida, Phys. Rev. B **57**, 9642 (1998).

[20] W.-J. Yin, S.-H. Wei, M. M. Al-Jassim, and Y. Yan, Appl. Phys. Lett. **99**, (2011).

[21] W.-J. Yin, T. Shi, and Y. Yan, J. Phys. Chem. C **119**, 5253 (2015).

[22] S. J. Clark, J. Robertson, S. Lany and A. Zunger, Phys. Rev. B **81**, 115311 (2010).

Table 7.1. Formation enthalpies (in eV) of twelve neutral intrinsic defects in Cs_2SnI_6 at the chemical potential points A, B, C, and D shown in Fig. 7.1.

	V_{Cs}	V_{Sn}	V_I	Cs_i	Sn_i	I_i	Cs_{Sn}	Sn_{Cs}	Cs_I	Sn_I	I_{Cs}	I_{Sn}
A	1.61	3.63	0.74	2.86	2.77	2.54	3.74	3.50	1.57	5.47	2.62	1.74
B	1.37	4.11	0.74	3.10	2.28	2.54	4.46	2.78	1.81	4.98	2.38	2.23
C	1.71	5.47	0.40	2.76	0.93	2.88	5.48	1.76	1.14	3.29	3.06	3.92
D	2.07	5.47	0.28	2.40	0.93	3.00	5.12	2.12	0.65	3.17	3.54	4.04

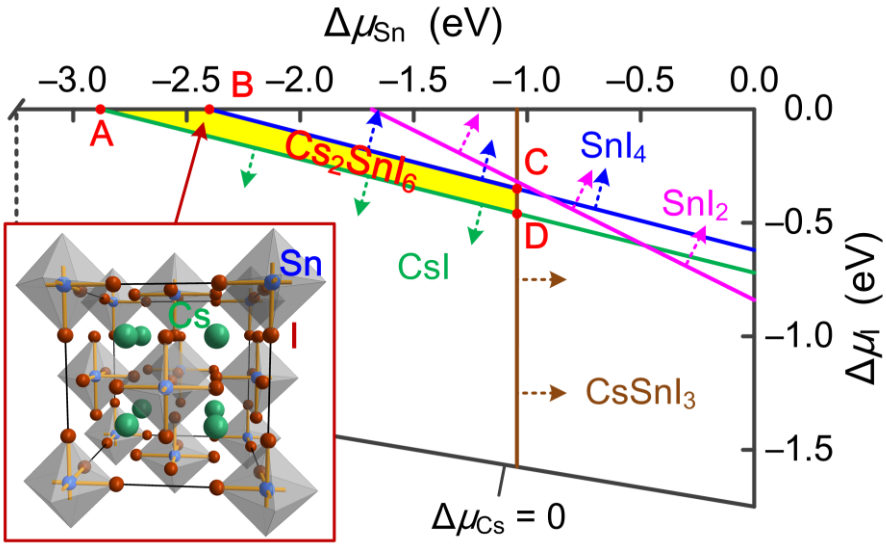

Figure 7.1. Chemical potential ($\Delta\mu_{Sn}$, $\Delta\mu_I$) – phase map. The yellow region A–B–C–D shows the region where Cs_2SnI_6 is stabilized against possible competitive phases including Cs, β-Sn, I_2, CsI, SnI_2, SnI_4, and $CsSnI_3$. The inset on left shows the crystal structure of Cs_2SnI_6.

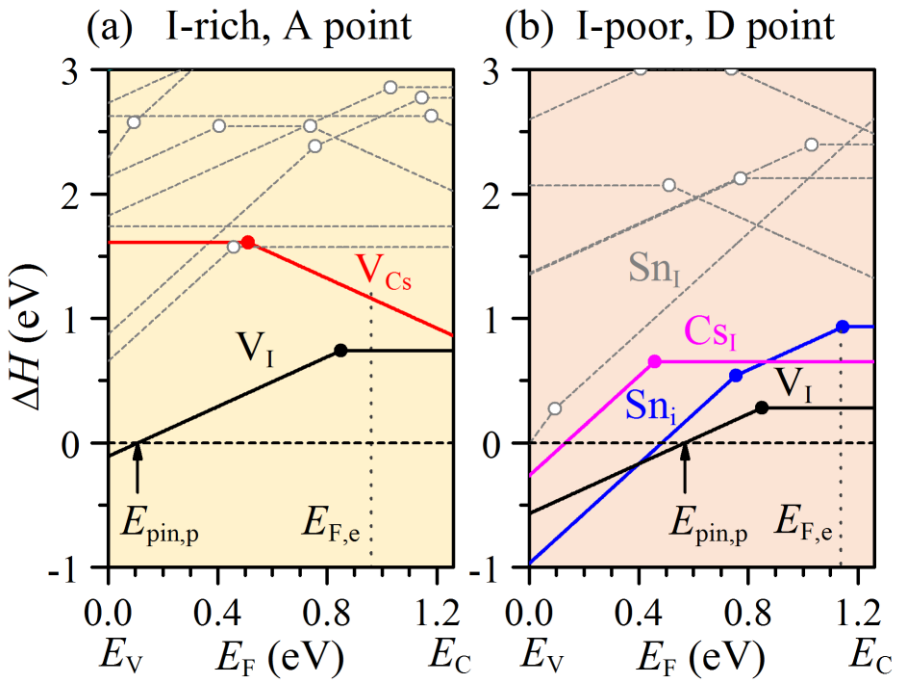

Figure 7.2. Calculated ΔH of intrinsic defects in Cs_2SnI_6 as a function of E_F at the chemical potential points in Figure 7.1, (a) A (I-rich) and (b) D (I-poor). Defects with much high ΔH values are shown by dashed lines.

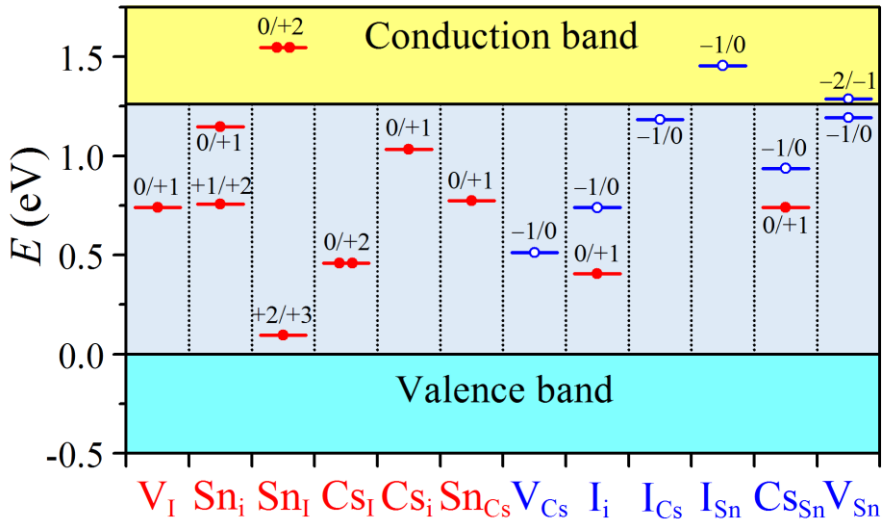

Figure 7.3. Calculated transition energy levels $\varepsilon(q/q')$ for intrinsic defects in Cs_2SnI_6. Donor and acceptor defect levels are denoted by red and blue bars, respectively. The solid and open circles at the transition levels show the number of electrons and holes that can be released during the transition of the defect charge state.

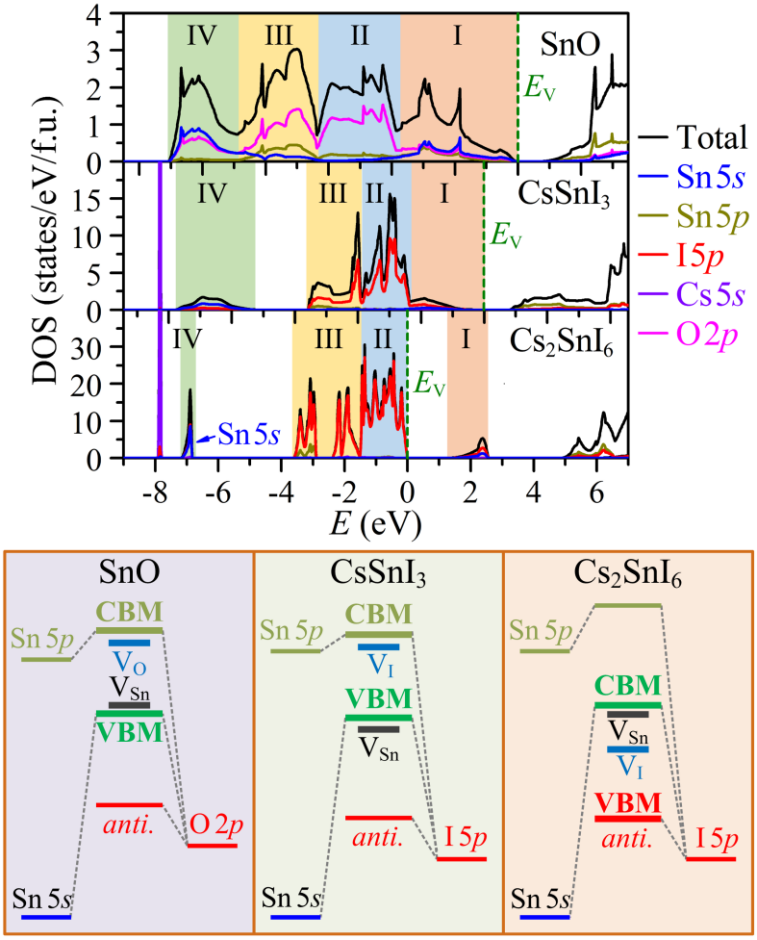

Figure 7.4. (a) Total and projected densities of states (DOSs/PDOSs) of $Sn^{2+}O^{2-}$ (top panel), $Cs^{+}Sn^{2+}I^{-}_{3}$ (middle panel), and $Cs^{+}_{2}Sn^{2+}[I_6]^{4-}$ (bottom panel). The energy is aligned by Sn 4*d* and Cs 5*s*. (b–d) Simplified energy diagrams depicting the formation of VBM, CBM, and donor-/acceptor-like defects in (b) $Sn^{2+}O^{2-}$, (c) $Cs^{+}Sn^{2+}I^{-}_{3}$, and (d) $Cs^{+}_{2}Sn^{2+}[I_6]^{4-}$.

Chapter 8

General Conclusions

8.1 General Conclusions

This study was performed to develop new inorganic semiconductors with an aid of first-principles H/DFT calculations. Particulary, the following two objectives are designated; one is to design *p*-type amorphous semiconductor, and the other is to clarify the origins of doping asymmetry issues in SnS and Cs_2SnI_6 and to explore new doping routes.

In Chapter 2, $BaZn_2As_2$ was investigated for a high-mobility *p*-type semiconductor. High hole mobilities aroud 10 $cm^2\ V^{-1}\ s^{-1}$ were attained in amorphous $BaZn_2As_2$ thin films fabricated by plused lase deposition. The high mobilities should be attributed mainly to two reasons. One is the large dispersion of As 4*p* orbitals, which leads to small effective hole masses. The other is the ionic nature of As anions, which is considered to maintain the hole transport path in the amorphous structure. These results indicate that high hole mobilities would be attained even in amorphous semiconductors if heavy anions such as arsenic are employed.

In Chapter 4, the origins of doping asymmetry were investigated by DFT calculations. It was revealed that the easiness of *p*-type doping and the difficulity in *n*-type doping were caused by the shallow VBM (i.e. small ionization potential) and the shallow CBM (i.e. small electron affinity), respectively. Further, it was found that the shallow VBM and CBM

are caused by the strong *s*–*p* and *p*–*p* couplings between Sn^{2+} cation and S^{2-} anion.

In Chapter 5, *n*-type conduction was realized in isovalently Pb-substituted SnS films, which are explained by two reasons. The Pb substitution deepened the VBM and CBM, and thus reduced the severity of the doping asymmetry. More importantly, the Pb substitution invoked a geometrical size effect that enlarges the interlayer distance and subquently induces the formation of Sn and Pb cation interstials, which result in the electron doping.

In Chapters 6 and 7, the electronic structure and the doping mechanism were studied for Cs_2SnI_6 by DFT calculations. It was found that the covalent $Cs^{+}{}_2Sn^{2+}[I_6]^{4-}$ model explains the electronic structure better than the expected ionic $Cs^{+}{}_2Sn^{2+}I^{-}{}_6$ model. It was clarified that iodine vacancy and tin interstitial are the dominant defects that are responsible for the intrinsic *n*-type conduction in Cs_2SnI_6. Further, it was clarified that the doping asymmetry in Cs_2SnI_6, i.e., the easiness of *n*-type doping and the difficulty in *p*-type doping, results from the deep CBM (i.e. large electron affinity) and the deep VBM (i.e. large ionization potential), which are formed by the unoccupied Sn 5*s*–I 5*p* antibonding states in Cs_2SnI_6.

8.2 Future Perspective

In Chapter 2, high-mobility *p*-type conduction was attained by employing arsenic anions. It is expected that other heavy anions including phosphorus, antimony, tellurium and iodine would also appropriate for designing *p*-type morphous semiconductors. On the other hand, the choice of cations would also be important to control the electrical properties. In particular, it is desirable to find a new and improved semiconductors without using toxic or rare elements. Much efforts are needed to develop more *p*-type amorphous semiconductors,

and apply them for practical electronic devices.

In Chapters 5, the geometrical doping route was proposed as a novel idea for carrier doping. This achievement proves that even keeping the same crystal structure and the ion charges, easiness of impurity doping can be altered by modifying the geometrical lattice parameters, which makes the geometrical doping route more flexibile and applicable to materials in which aliovalent ion doping is not effective. On the other hand, applicability of the geometrical effect would be limited e.g. by the constituent elements and the crystal structure of a host material; therefore, it is still an important issue to find new doping routes to develop new semiconudctors; e.g., it may be achived by convering existing insulating materials into semiconductors and by solving doping asymmetry in unipolar dopable semiconductors.

Acknowledgements

The present study was carried out under the supervision of Professor Toshio Kamiya, Professor Hideo Hosono, Associate Professor Hidenori Hiramatsu, and Associate Professor Tomofumi Tada at Tokyo Institute of Technology (Tokyo Tech) from October 2012 to September 2015.

First of all, I would like to express my deepest gratitude to Professor Toshio Kamiya for all he has done for me. Prior to my doctoral course, he accepted me as an exchange student to study in his laboratory via the YSEP program from September 2011 to July 2012. Over the years, he has given me a lot of scientific suggestions and patiently guided me to first-principles calculations. Besides, he has offered me many chances to communicate with academic colleges in group meetings and academic conferences. He has also helped me a lot to get financial supports and to find a postdoctoral position. I have really enjoined my doctoral course and learned a lot with his guidance.

I would like to express my earnest gratitude to Professor Hideo Hosono for his kind guidance and insight. He has given me many valuable comments and suggestions to improve the journal papers and this thesis. I would like also to express my gratitude to Associate Professor Hidenori Hiramatsu for his experimental help and to Associate Professor Tomofumi Tada for his valuable discussion on first-principle calculations.

I would like to express my grateful thanks to Professor Masaki Azuma, Professor Fumiyasu Oba, and Associate Professor Takao Sasagawa at Tokyo Institute of Technology for their critical referring of this thesis and valuable comments.

I would like to thank Mr. Kataya Miyase (my tutor during the YSEP program), Associate Professor Satoru Matsuishi, Dr. Yoshitake Toda, Associate Professor Hiroshi

Mizoguchi, Mr. Keisuke Ide, Dr. Kay Domen, Dr. Katsumi Abe, Mr. Hikaru Satoru, Mr. Joonho Bang, Mr. Junghwan Kim, and other laboratory members for their kindly help with experimental characterizations and measurements. I would like also to thank the project managers Professor Satoru Fujitsu and Professor Hideya Kumomi, and the laboratory secretaries Ms. Kanako Ochiai, Ms. Mayumi Nakano, and Ms. Hanae Murayama for their administrative supports.

I would like to express my deep gratitude to my cooperators and good friends Dr. Fan-Yong Ran, Dr. Hechang Lei (currently at Renmin University of China), Dr. Yanpeng Qi (currently at Max Planck Institute for Chemical Physics of Solids), Dr. Jiangang Guo (currently at Rice University), Dr. Xiao Zhang, Dr. Min Liao, Dr. Yaoqing Zhang and Mr. Yuanyuan Zhou (a PhD candidate at Brown University) not only for their active experimental corporation and valuable scientific discussion, but also for their kindly help in daily life.

Last but not least, I owe a great deal of gratitude to all my family members. My wife Yan Zeng has been my soul mate since high school. She has helped me to make many important choices and been always encouraging and urging me to do better. She has done much to take care of our family and to look after our lovely one-year-old daughter Huizhen Xiao, whose birth has inspired me so much. My parents and parents-in-law have always been understanding and supporting mine and my wife's choices. All these have made me concentrate much more on my doctoral course.

Publication List

Papers Included in the Thesis

1. "Narrow bandgap in β-$BaZn_2As_2$ and its chemical origins"
   Zewen Xiao, Hidenori Hiramatsu, Shigenori Ueda, Yoshitake Toda, Fan-Yong Ran, Jiangang Guo, Hechang Lei, Satoru Matsuishi, Hideo Hosono, and Toshio Kamiya
   Jounal of American Chemical Society **136**, 14959–14965 (2014).

2. "Intrinsic defects in photovoltaic perovskite variant Cs_2SnI_6"
   Zewen Xiao, Yuanyuan Zhou, Hideo Hosono, and Toshio Kamiya
   Physical Chemistry Chemical Physics, **17**, 18900–18903 (2015).

3. "Route to n-type doping in SnS"
   Zewen Xiao, Fan-Yong Ran, Hideo Hosono, and Toshio Kamiya
   Applied Physics Letters **106**, 152103 (2015).

4. "Ligand-hole in SnI_6 unit and origin of band gap in photovoltaic perovskite variant Cs_2SnI_6"
   Zewen Xiao, Hechang Lei, Xiao Zhang, Yuanyuan Zhou, Hideo Hosono, and Toshio Kamiya
   Bulletin of the Chemical Society of Japan doi:10.1246/bcsj.20150110 (2015).

5. "Epitaxial growth and electronic structure of a layered zinc pnictide semiconductor, β-$BaZn_2As_2$"
   Zewen Xiao, Fan-Yong Ran, Hidenori Hiramatsu, Satoru Matsuishi, Hideo Hosono, and Toshio Kamiya
   Thin Solid Films **559**, 100–104 (2014).

6. "*n*-type conversion of SnS by isovalent ion substitution: Geometrical doping as a new doping route"
   Fan-Yong Ran, **Zewen Xiao**, Yoshitake Toda, Hidenori Hiramatsu, Hideo Hosono, and Toshio Kamiya
   Scientific Reports **5**, 10428 (2015).

7. "High-mobility *p*-type amorphous semiconductor $BaZn_2As_2$" (in preparation)
   Zewen Xiao, Fan-Yong Ran, Min Liao, Shigenori Ueda, Hidenori Hiramatsu, Hosono Hideo, and Tosho Kamiya

Other Papers

1. "Two-dimensional transition metal electride Y_2C"
   Xiao Zhang,[*] **Zewen Xiao**,[*] Hechang Lei, Yoshitake Toda, Satoru Matsuishi, Toshio Kamiya, and Hideo Hosono
   Chemistry of Materials **26**, 6638–6643 (2014). ([*]shared first authors)

2. "Apparent high mobility ~30 cm^2/Vs of amorphous In–Ga–Zn–O thin-film transistor and its origin"
   Zewen Xiao, Kay Domen, Toshio Kamiya, and Hideo Hosono
   Journal of the Ceramic Society of Japan **121**, 295–198 (2013).

3. "Growth of high-quality SnS epitaxial films by H_2S flow pulsed laser deposition"
   Fan-Yong Ran, **Zewen Xiao**, Hidenori Hiramatsu, Hideo Hosono, and Toshio Kamiya
   Applied Physics Letters **104**, 072106 (2014).

4. "Superconductivity in noncentrosymmetric ternary equiatomic pnictides La*MP* (*M* = Ir and Rh; *P* = P and As)"
   Yanpeng Qi, Jiangang Guo, Hechang Lei, **Zewen Xiao**, Toshio Kamiya. Hideo Hosono
   Physical Review B **89**, 204517 (2014).

5. "Effects of Pb doping on hole transport properties and thin-film transistor characteristics of SnO thin films"
   Min Liao, **Zewen Xiao**, Fan-Yong Ran, Hideya Kumomi, Toshio Kamiya, and Hideo Hosono
   ECS Journal of Solid State Science and Technology **4**, Q26–Q30 (2015).

6. "Difficulty of carrier generation in PbO in comparison with SnO"
   Min Liao, Seiji Takemoto, **Zewen Xiao**, Yoshitake Toda, Tomofumi Tada, Toshio Kamiya, and Hideo Hosono
   to be sumitted.

7. "Electron confinement in channel spaces for one-dimensional electride"
   Yaoqing Zhang,[*] **Zewen Xiao**,[*] Toshio Kamiya, and Hideo Hosono
   to be submitted. ([*]shared first authors)

Presentation List

International Oral Presentations

1. "Unexpected electronic structure of air-stable lead-free perovskite variant Cs2SnI6 for photovoltaic application"
   Zewen Xiao, Hechang Lei, Hidenori Hiramatsu, Hideo Hosono, and Toshio Kamiya
   The 2015 MRS Spring Meeting & Exhibit, San Francisco, April 6–10, 2015.

International Poster Presentations

1. "Carrier transport and origins of narrow bandgap for *p*-type layered semiconductor, β-$BaZn_2As_2$"
   Zewen Xiao, Fan-Yong Ran, Hidenori Hiramatsu, Hideo Hosono, and Toshio Kamiya
   The 2014 E-MRS Spring Meeting and Exhibit, Lille, May 26–30, 2014.

2. "*n*-type conduction in SnS-based thin films"
   Fan-Yong Ran, **Zewen Xiao**, Hidenori Hiramatsu, Hideo Hosono, and Toshio Kamiya
   The 2014 E-MRS Spring Meeting and Exhibit, Lille, May 26–30, 2014.

3. "Electronic structures of Zn–Pn (*Pn* = P, As, Sb)-based layered crystals"
   Zewen Xiao, Toshio Kamiya, Hiramatsu, and Hideo Hosono
   The 12th Asia Pacific Physics Conference, Chiba, July 14–19, 2013.

4. "Synthesis and epitaxial growth of novel layered zinc pnictide semiconductor, β-$BaZn_2As_2$."
   Zewen Xiao, Hidenori Hiramatsu, Hideo Hosono, and Toshio Kamiya
   The 8th International Symposium on Transparent Oxide and Related Materials for Electronics and Optics, Tokyo, May 13–15, 2013.

5. "Apparent high mobility ~30 cm^2/Vs of amorphous In–Ga–Zn–O thin-film transistor and its origin"
   Zewen Xiao, Kenji Nomura, Toshio Kamiya, and Hideo Hosono
   The 6th International Conference on the Science and Technology for Advanced Ceramics, Yokohama, June 26–28, 2012.

Demotic Poster Presentations

1. "*n*-type doping in SnS: Origin of difficulty and the success by isovalent Pb-doping"
   Zewen Xiao, Fan-Yong Ran, Hidenori Hiramatsu, Hideo Hosono, and Toshio Kamiya
   The 11th Thin Film Materials & Devices Meeting, Kyoto, Oct 31–Nov 1, 2014.

2. "Carrier transport and origins of narrow bandgap for *p*-type layered semiconductor, β-$BaZn_2As_2$"
   Zewen Xiao, Hidenori Hiramatsu, Hideo Hosono, Toshio Kamiya, Shigenori Ueda, and Naoki Ohashi
   The 61st JSPS Spring Meeting, Sagamihara, Mar 17–20, 2014.

3. "Carrier transport of layered *p*-type semiconductor, β-$BaZn_2As_2$, and origins of its narrow bandgap"
   Zewen Xiao, Fan-Yong Ran, Haochun Tang, Hidenori Hiramatsu, Hideo Hosono, and Toshio Kamiya
   The 10th Thin Film Materials & Devices Meeting, Kyoto, Dec 31–Nov 2, 2014.

4. "Apparent high Mobility ~30 cm^2/Vs of amorphous In–Ga–Zn–O thin-film transistors and its origin"
   Zewen Xiao, Junghwan Kim, Toshio Kamiya and Hideo Hosono
   The 9th Thin Film Materials & Devices Meeting, Nara, Nov 2–3, 2014.